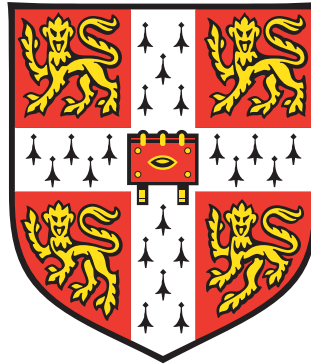


UNIVERSITY OF CAMBRIDGE
CAVENDISH LABORATORY

High magnetic field quantum
oscillation study of Fermi surfaces in
bulk unconventional insulators



Hsu Liu

HOMERTON COLLEGE

SUBMITTED MAY 2021

This dissertation is submitted for the degree of Doctor of Philosophy

Declaration

This dissertation is the result of my own work and includes nothing which is the outcome of work done in collaboration except as declared in the Preface and specified in the text. It is not substantially the same as any that I have submitted, or, is being concurrently submitted for a degree or diploma or other qualification at the University of Cambridge or any other University or similar institution except as declared in the Preface and specified in the text. I further state that no substantial part of my dissertation has already been submitted, or, is being concurrently submitted for any such degree, diploma or other qualification at the University of Cambridge or any other University or similar institution except as declared in the Preface and specified in the text. This dissertation does not exceed the word limit of 60,000 prescribed by the Degree Committee for the Faculty of Physics and Chemistry.

The research projects described in this thesis were performed under the supervision of Dr. Suchitra E. Sebastian. Polycrystalline YbB_{12} was prepared by Dr. Natalya Shitsevalova's group at the National Academy of Sciences of Ukraine, and single crystal YbB_{12} samples were grown by Prof. Geetha Balakrishnan's group at the University of Warwick. Single crystal FeSb_2 samples were prepared by Prof. Zhi-Xun Shen's group at Stanford University. Basic elemental characterization of the samples including powder x-ray diffraction, scanning electron microscopy, and energy-dispersive x-ray spectroscopy were performed by the crystal growers.

Sample preparation work including sample sectioning, electropolishing, mounting onto sample holders, and wiring were performed by myself. Low magnetic field sample characterization work, including the measurement of Laue backscattering diffraction, electrical

resistivity, magnetic susceptibility, specific heat capacity, and preliminary measurements of quantum oscillations were mainly performed by myself. Measurements performed by external companies, collaborators, and colleagues that differed from routine characterization, such as mass spectroscopy and high precision specific heat capacity measurements on FeSb₂, are acknowledged in the text. The intermediate-field magnetic susceptibility data on FeSb₂ shown in Chapter 5 is part of an ongoing study of the magnetic anisotropy of the material performed by colleagues within the group; this is also acknowledged in the text.

High magnetic field measurements were performed as a team with other members of the group and assistance from local support staff. Sample preparation and mounting at high field facilities were performed by myself. Measurements were led by myself and performed as a group. Torque magnetization quantum oscillation data on YbB₁₂ were analyzed in collaboration with colleague Máté Hartstein, where each of us analyzed one of two samples measured simultaneously during a magnet run. Electrical resistivity and proximity diode oscillator quantum oscillation data on YbB₁₂ were analyzed by myself. Torque magnetization quantum oscillation data on FeSb₂ were analyzed in collaboration with colleague Alexander G. Eaton in the same manner as the YbB₁₂ torque magnetization analysis. Advice on background subtraction parameters and additional checks were performed by colleague Alexander J. Hickey. Any additional help on data analysis from colleagues are acknowledged in the text.

The study of YbB₁₂ presented in Chapter 4 has been published in the Journal of Physics: Condensed Matter **30** 16LT01 and arXiv:2102.09545. The arXiv preprint has been submitted to npj Quantum Materials for publication and is undergoing peer review. The study of FeSb₂ presented in Chapter 5 has been submitted to Science for publication and is also undergoing peer review.

A number of figures presented in this thesis have been made with input from colleagues Máté Hartstein (Figs. 4.4, 4.5, 4.6, 4.13, 4.15, 5.4, 4.16, 4.17, A.1), Alexander J. Hickey (Figs. 5.5, 5.9, C.1), and Alexander G. Eaton (Figs. 5.6, 5.7, 5.9, 5.10, 5.11).

Hsu Liu

May 2021

High magnetic field quantum oscillation study of Fermi surfaces in bulk unconventional insulators

Hsu Liu

As a field of study that investigates how microscopic interactions affect macroscopic material properties, condensed matter physics takes great interest in understanding how charge carriers respond to external stimuli. A fundamental distinction has therefore existed between conductors and insulators, where charge carriers' ability to move freely separates the two phases of matter. However, even this seemingly immutable distinction has recently begun to blur. The recent discovery of a bulk Fermi surface in the Kondo insulator SmB_6 has raised serious questions about how a fundamentally metallic property could be intrinsically realized in a robust insulator. This thesis describes my work to further our understanding of this surprising behavior by searching for other examples of unconventional quantum oscillatory insulators.

Following SmB_6 , two additional strongly correlated insulators have been found to display insulating quantum oscillations: YbB_{12} and FeSb_2 . YbB_{12} is an f -electron Kondo insulator, much like SmB_6 , and exhibits similar electrical and thermal properties to SmB_6 . FeSb_2 , on the other hand, is a d -electron insulator that had previously attracted attention for its unusual thermal properties. While united in exhibiting intrinsic insulating phase quantum oscillations that originate from the sample bulk, the two materials separately illuminate important insights into insulating phase quantum oscillations.

Despite its similar physical properties to SmB_6 , YbB_{12} was found to exhibit slow and heavy quantum oscillations, in stark contrast to the fast and light quantum oscillations

in SmB_6 . YbB_{12} has also been found to display sizable quantum oscillations in electrical resistivity, a feature which has not yet been observed in SmB_6 and remains the topic of much theoretical debate. Furthermore, an investigation of quantum oscillations in the field-induced metallic phase of YbB_{12} has revealed more of the same Fermi surface observed in the insulating phase. Taken together, the discoveries in YbB_{12} suggest a rich variety of insulating phase Fermi surfaces which are shaped by material bandstructure, much like metallic phase Fermi surfaces.

While discoveries in YbB_{12} hint at the breadth of insulating Fermi surfaces, the investigation of FeSb_2 takes us one step closer to pinpointing the mechanism that underlies insulating phase quantum oscillations. Quantum oscillations in FeSb_2 have shown a strong coupling to a metamagnetic-like transition in the magnetic torque, which reflects anisotropic magnetization. The transition correlates the onset of a novel high field phase with enhanced quantum oscillation amplitude and frequency spectrum. Moreover, the temperature dependence of this onset has shown a tentative link to a dramatic increase in quantum oscillation amplitudes at low temperatures beyond the description of the Lifshitz-Kosevich formalism, a behavior also seen in SmB_6 . The discoveries in FeSb_2 therefore strengthens the proposition of Fermi surfaces arising from novel quasiparticles that do not participate in longitudinal charge transport.

The discovery of insulating phase quantum oscillations in the correlated insulators YbB_{12} and FeSb_2 has helped accelerate a rapidly growing field of study around the unexpected finding of unconventional quantum oscillatory insulators. The new discoveries show a rich variety of insulating Fermi surfaces, and provide suggestions towards the origin of this surprising phenomenon. These studies further motivate efforts to uncover additional unconventional quantum oscillatory insulators and devise a theoretical description to capture the rich variety of unconventional insulating Fermi surfaces.

Acknowledgements

I am grateful for all the help and encouragements I have received on this journey. I would like to thank my supervisor Suchitra Sebastian for offering me the opportunity to do a PhD in Cambridge and to participate in the countless magnet times that made this thesis possible. I would also like to thank everyone in the group, past and present, for the camaraderie and companionship: Yu-Te Hsu for imparting me your immense technical expertise; Máté Hartstein for being the unwavering voice of reason and curiosity; Sofia Taylor for love and care at magnet times, APS, and in Cambridge; Alex Davies for the helping hand when I needed it most during magnet times; Alex Hickey for unfailingly logical criticisms and for keeping me sane in Dresden; Alex Eaton for the reliable stream of witty input, pleasant entertainment, and resourcefulness.

Special thanks to Cheng, Patricia, Jiasheng, Michael, Matt, Gilles, Nick, and all our summer students for helping me along this journey. Thanks also to Geetha and Monica in Warwick, Alix and Bryan in Nijmegen, Tobias in Dresden, and Kohama-san, Miyake-san, Nomura-san, and Zhuo in ISSP for your warm hospitality. I am also indebted to the generous financial support of The Taiwanese Ministry of Education, Homerton College, the Institute for Complex Adaptive Matter, and the Cambridge Philosophical Society.

Lastly, this thesis would not be complete without acknowledging my parents. Thank you for setting me onto this path and for always standing by me. I would not have made it this far without you.

Contents

1	Introduction	1
2	Relevant Theoretical Concepts	7
2.1	Correlated electron systems	8
2.2	The Kondo system	10
2.3	Quantization of quasiparticle energy in a magnetic field	14
2.4	Quantum oscillatory behavior in a magnetic field	22
3	Experimental Methods	29
3.1	Sample Preparation	29
3.2	High Magnetic Field Measurements	37
3.3	Quantum oscillation background subtraction	62
3.4	Numerical simulations of quantum oscillations	67
4	Unconventional insulating quantum oscillations in YbB₁₂	73
4.1	Introduction	73
4.2	Sample characterization	77

4.3	Quantum oscillations in the unconventional insulating phase of YbB ₁₂	79
4.4	Quantum oscillations in the field-induced metallic phase of YbB ₁₂	87
4.5	Bulk origin of quantum oscillations in the unconventional insulating phase	92
4.6	Gapless origin of quantum oscillations in the unconventional insulating phase	95
4.7	Insulating Fermi surface mirroring a heavy fermion semimetal	98
4.8	Comparison with quantum oscillations observed by independent research group	103
5	Unconventional insulating quantum oscillations in FeSb₂	107
5.1	Introduction	107
5.2	Sample characterization	113
5.3	Magnetic torque quantum oscillations in FeSb ₂	117
5.4	Novel metamagnetic transition accompanied by enhanced quantum oscillations	121
5.5	Non-Lifshitz-Kosevich quantum oscillation amplitude growth at low temperatures	125
6	Towards the origin of insulating quantum oscillations	129
6.1	Proposed models of insulating quantum oscillations	129
6.2	Metamagnetism and insulating quantum oscillations	132
6.3	Band hybridization and quantum oscillations	135
7	Conclusions	139
	Appendix A Absolute amplitude of magnetic torque quantum oscillations	143
A.1	YbB ₁₂	145

A.2 FeSb ₂	146
Appendix B Non-LK quantum oscillation amplitude temperature-dependence for gapped models compared with LK temperature-dependence for gapless models	147
B.1 Model simulations	147
B.2 Low temperature model expansion	150
Appendix C Sample magnetic impurity content from Langevin fit	153
References	155

Chapter 1

Introduction

“Alone we can do so little, together we can do so much”

– Helen Keller

The year was 1961, and the field of condensed matter physics was struggling with mid-life crisis. As Cambridge’s own Brian Pippard declared, “the disappearance of liquid helium, superconductivity, and magneto-resistance from the list of major unsolved problems has left this branch of research looking pretty sick from the point of view of any young innocent who thinks he’s going to break new ground” [1].

Fortunately, condensed matter physics had many more new grounds to be broken. Taking an example relevant to this thesis, merely three years after Pippard’s utterances, Jun Kondo proposed a theoretical framework to describe a class of insulators that would later take his name. Kondo insulators, the first known example of which is SmB_6 [2], have the unusual property of being conductors at room temperature but transitioning to insulators when cooled to cryogenic temperatures [3]. While it was believed that strong interaction between localized spins and conduction electrons was responsible for the resistivity divergence, Kondo’s solution using exchange interactions led to unphysical singularities. The resolution of this problem required the development and adoption of a new statistical method, the renormalization group, hinting at the sheer complexity of condensed matter behavior [4].

A few other unusual condensed matter systems with relevance for this thesis include heavy fermion materials where electrons behave as though they are under the weight of many times their rest mass [5], spin liquids in one-dimensional metals where spin and charge are able to move separately [6], and, most recently, topological phases of material [7].

Much of the beguiling yet fascinating behavior observed in condensed matter physics result from emergence, the idea that collectives behave in ways that are much different than what would be exhibited by the constituents. Materials in which the interaction between charge carriers can no longer be neglected are collectively referred to as strongly correlated systems. The Kondo insulator is one such example, as pure conductors and insulators would see their resistivity decrease or increase monotonically in temperature, rather than transition from one to the other [8].

Despite the myriad of unusual behavior exhibited by strongly correlated materials, one seemingly immutable concept is the distinction between conductors and insulators. Qualitatively, the difference between a conductor and an insulator can be thought of as whether electrons can move freely in a material. Formally, the Fermi liquid theory treats the distinction through the concept of low energy excitations [9]. For particles that obey Fermi-Dirac statistics, available momentum states are filled up to some material-specific chemical potential at zero temperature. If the chemical potential falls within a partially-filled band, minimal energy is required to excite a particle into the next higher energy state. In this case, a well-defined boundary separates filled momentum states from unfilled ones at zero temperature – this is the Fermi surface. At finite temperatures, only a minimal amount of energy is required to excite a particle across the Fermi surface, and states near the Fermi surface are said to host low energy excitations. On the other hand, if the chemical potential falls within a band gap, some nontrivial amount of energy is required to excite a particle to the next higher energy state, and the Fermi surface is no longer well defined. Fig. 1.1 provides a graphical illustration of this distinction.

True to the trailblazing history of condensed matter physics, even this seemingly fundamental distinction between conductors and insulators has recently begun to blur. While probing the Kondo insulator SmB_6 [2], our group found high frequency, large amplitude

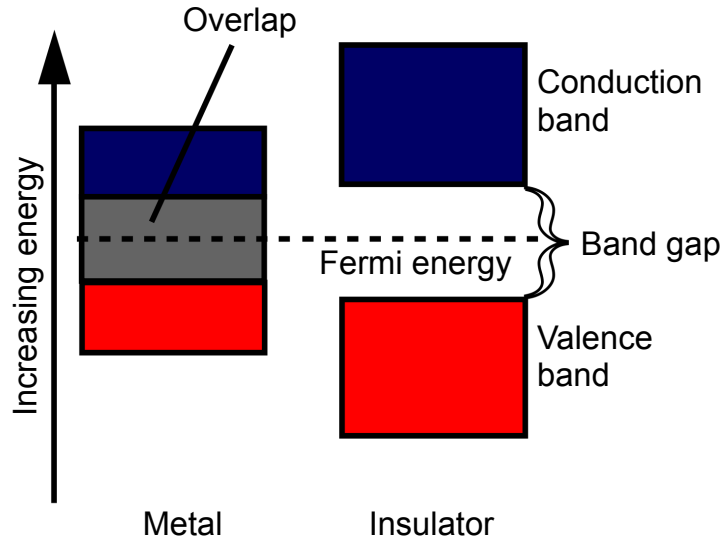


Fig. 1.1. Schematic of band gap for a metal compared to an insulator. Illustration showing finite density of states at the Fermi energy for metals, compared to a gap of forbidden energy states in an insulator. As the Fermi surface is the set of states that can host low energy excitations, the concept is well defined in a metal but not in an insulator. Image courtesy of Wikimedia commons [10].

quantum oscillations in the material’s torque magnetization [11, 12]. Under conventional Lifshitz-Kosevich (LK) theory, quantum oscillations result from a quantization of energy levels as electrons are driven into circular orbit under the influence of an applied magnetic field. The established theoretical paradigm would suggest that high frequency quantum oscillations observed in SmB_6 correspond to electron mean free paths on the order of a few micrometers [13]. Such high electron mobility is in tension with the electrical resistivity of SmB_6 , which indicate that electrons can travel no further than a picometer, and presents a dramatic departure from established theory (Fig. 1.2).

In addition to quantum oscillations, a wealth of anomalies have been observed in SmB_6 . Indeed, a finite residual linear coefficient γ of specific heat capacity at low temperatures, typically reflecting low energy electronic excitations, has long been an unsolved mystery in the material [14]. More recently, our group reported a steep, inexplicable increase in γ at

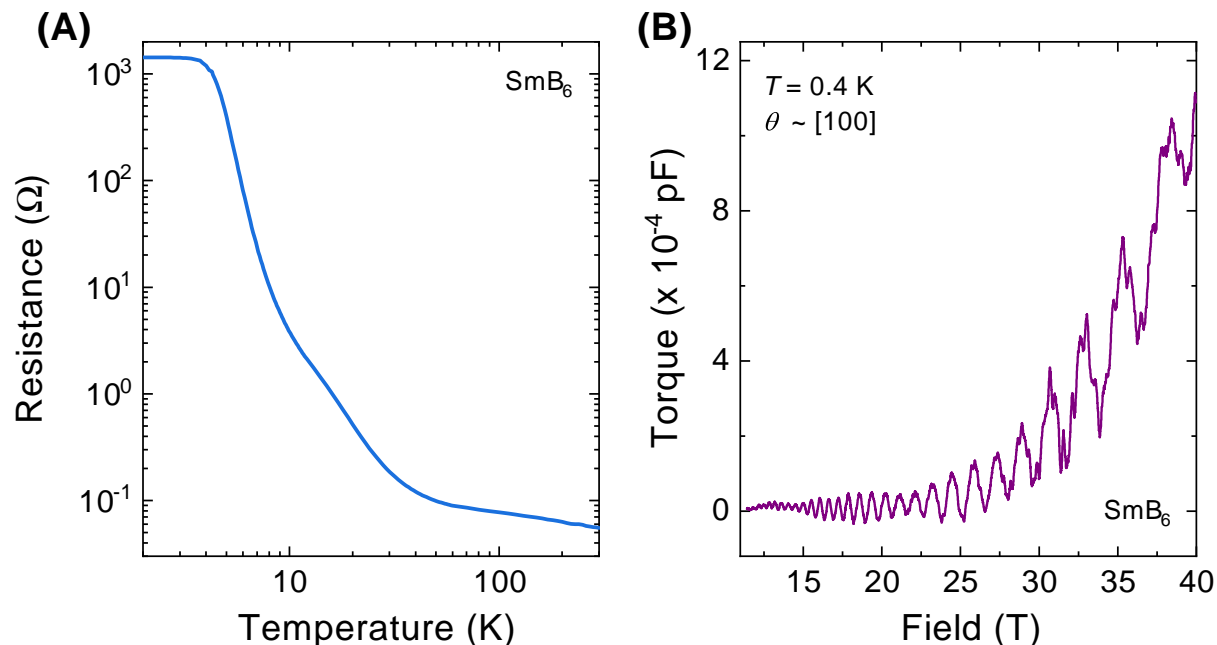


Fig. 1.2. Insulator-metal dichotomy in the unconventional insulator SmB₆. (A) Measured electrical resistance as a function of temperature for SmB₆. While the material is a conductor at room temperature, interactions between mobile electrons and localized spins lead to the formation of a robustly insulating state below temperatures of approximately 50 K [14]. (B) Large amplitude, high frequency quantum oscillations observed in SmB₆. Conventional Lifshitz-Kosevich theory would indicate that these oscillations result from the quantization of highly mobile electrons with mean free paths on the order of a few micrometers, in sharp tension with the highly insulating behavior shown in (A) [11, 12].

very low temperatures below 0.1 K, which appears to correspond to an equally surprising divergence in the quantum oscillation amplitude beyond the predictions of conventional theory [11, 12]. A finite linear coefficient of thermal conductivity that appears with and is enhanced by applied magnetic fields has also been observed, indicative of heat-carrying magnetic quasiparticles in spite of a nonmagnetic insulating ground state [12]. An additional puzzle in SmB₆ is its lack of quantum oscillations in electrical resistivity, despite efforts by multiple research groups to measure them. The selective response to magnetic fields is

puzzling, as the Lorentz force law would predict a simultaneous coupling to both magnetic and electric fields through the vector potential. The insulator-metal dichotomy, viewed in light of even more exotic behavior such as low temperature amplitude divergences and the absence of resistivity quantum oscillations, suggest brand new physics waiting to be explained.

Since the distinction between conductors and insulators has been regarded as a fundamental concept, the idea of looking for quantum oscillations in insulators would have crossed few people's minds. The discoveries in SmB_6 therefore raised the possibility that unconventional Fermi surfaces exist in other insulators. As such, my thesis is concerned with establishing unconventional Fermi surfaces as a widespread phenomenon with a diverse variety of behavior. This research broadens the field of study to encompass additional quantum oscillatory insulators: the Kondo insulator YbB_{12} , which is often mentioned in the same breath with SmB_6 for their similar physical properties, and the d -electron correlated insulator FeSb_2 , the first insulator without f -electrons to exhibit quantum oscillations. My research has unearthed clues to the physical mechanism that underlies insulating quantum oscillations, by asserting the gapless origin of the quantum oscillations, suggesting a relationship between material band structure and insulating quantum oscillations, and uncovering a novel insulating metamagnetism to which the quantum oscillations couple. Together, these discoveries take us many steps forward in understanding the true scope of insulating Fermi surfaces and extricating the physical origin behind this wonderful phenomenon.

This thesis is structured as follows. In Chapter 2, I will present a theoretical overview of correlated insulators and the conventional description of quantum oscillation. In Chapter 3, I will detail the experimental methods used, including sample preparation, characterization, high magnetic field measurement techniques, as well as numerical methods. Chapters 4 and 5 delve into quantum oscillation measurements on YbB_{12} and FeSb_2 , respectively. Chapter 6 presents a discussion of currently proposed theoretical explanations of insulating quantum oscillations, as well as new lessons learned from our study of YbB_{12} and FeSb_2 . Finally, Chapter 7 concludes the thesis with a summary of the main findings and a brief description of the future outlook.

1. Introduction

Chapter 2

Relevant Theoretical Concepts

The two materials that are the focus of my PhD, YbB_{12} and FeSb_2 , are known as correlated insulators. The “correlated” designation indicates that electron interaction is intimately responsible for the physical properties of these materials. Specifically, YbB_{12} is a Kondo insulator [15], a class of materials with a rich history of theoretical developments where an energy gap is formed as a result of hybridization between the conduction and localized bands. FeSb_2 has also been considered a Kondo insulator, however whether the Kondo effect plays a leading role in the gap formation in FeSb_2 remains a subject of active debate [16, 17]. More recently, YbB_{12} has been proposed as a topological Kondo insulator, which is thought to host topologically protected surface conduction states juxtaposed with an insulating bulk [18]. Tentative evidence have also been found for the existence of topological surface conduction states in FeSb_2 [19].

While it is unclear how established theoretical paradigms relate to insulating quantum oscillations in YbB_{12} and FeSb_2 , an understanding of existing theories helps us place the new discoveries in context. This chapter covers relevant theoretical concepts spanning electron correlation, band hybridization, the Kondo system, and quantum oscillations of physical properties using established theories. An overview of theories that have been proposed to explain insulating phase quantum oscillations thus far will be given in Chapter 6.

2.1 Correlated electron systems

Correlated systems is an overarching term that refers to any system where many-body interactions affect macroscopic properties. Much of the exotic physics discovered in the past few decades result from strong correlation. For instance, in cuprate superconductors, electronic interactions give rise to an antiferromagnetic Mott insulator ground state, which becomes host to high temperature superconductivity when doped [20]. In heavy-fermion compounds, interaction between localized magnetic moments and electrons in a dispersive conduction sea give rise to quasiparticles effective masses that are orders of magnitude heavier than the electron rest mass [21]. In fractional quantum Hall systems, electronic interactions in a two-dimensional system give rise to exotic quasiparticles with fractional charge [22]. To gain an intuitive understanding of how correlated systems differ from weakly-interacting systems, it is informative to look at the simplest such example – the Mott insulator.

A traditional band insulator arises when the chemical potential of a non-interacting system falls within a band gap. In a free electron gas that is not under the influence of external potentials, electrons are able to occupy any state among a continuous spectrum of momentum states. When such an electron gas is placed under the influence of a periodic potential from, for instance, a crystal lattice, gaps of forbidden energy states appear [23]. If a material's chemical potential falls within one such energy gap, energy states below the gap will be filled at zero temperature. As the momenta of all electrons average to zero in this case, such a system would not respond to weak electric fields. A non-trivial amount of energy is therefore required to excite an electron into the next available energy state and drive an electrical current.

In a Mott insulator, the above band theory in the absence of electron interactions would predict a metallic ground state. This can be intuitively pictured by considering a toy lattice of half-filled atoms. Assuming that the Pauli exclusion principle does not forbid electron hopping, one would expect the electrons on the toy lattice to respond to applied electric fields and roam freely. However, if the Coulomb repulsion between two electrons on a single atomic site is sufficiently strong, the system settles into a ground state with a single electron

on each atomic site. An energy gap is therefore opened by electron interaction, and a large electric field is required to overcome Coulomb repulsion and drive an electrical current.

When we consider that macroscopic materials contain a few Avogadro number's worth of electrons, it is remarkable that non-interacting theories can capture the physics of condensed matter systems at all. The success of the non-interacting picture can be explained by the Landau Fermi liquid theory, which models fermionic interactions as a perturbation that is adiabatically turned on from a system of a non-interacting fermions [9].

The critical piece of insight from Landau is that Pauli exclusion severely restricts the number of states below the Fermi level an excited electron can scatter into. The closer an excited electron is to the Fermi surface, the fewer available states it has access to. As a result, the inelastic scattering rate of a system of interacting fermions grows quadratically with both temperature and excitation energy. Such a scaling implies that excitations at the Fermi energy develop a long lifetime – these long lasting excitations are referred to as quasiparticles. Since quasiparticle lifetimes are usually orders of magnitude higher than the typical relaxation time of a metal at room temperature, the effect of electron-electron interaction only become significant at sufficiently low temperatures.

One consequential claim of the Fermi liquid theory is that adiabaticity leads to a one-to-one correspondence between an excited state in a non-interacting system to one in an interacting system [8]. As a result of this correspondence, the conserved quantum numbers of an excited particle, such as its spin and charge, are unchanged. Therefore, the dominant effect of interaction is to renormalize the dynamic properties of the particle, or the quasiparticle effective mass and magnetic moment (the g -factor). As long as they remain near the Fermi surface, quasiparticles can be treated in the same way as normal particles, only with different masses and magnetic moments.

2.2 The Kondo system

Before introducing the Kondo system, we first examine the Anderson model, which describes the interaction between localized spins with the surrounding conduction sea [24, 25]. Both theories came about from the study of pure metals with dilute magnetic impurities. While elemental metals exhibit a monotonic decrease in electrical resistivity with decreasing temperature, the presence of magnetic impurities sometimes leads to a resistivity minimum at a finite temperature. The Anderson model was proposed to explain such resistivity minima by taking into account localizing Coulomb interactions and tunneling between localized orbitals and the conduction sea:

$$H_{\text{Anderson}} = \sum_{\mathbf{k}, \sigma} \epsilon_{\mathbf{k}} n_{\mathbf{k}\sigma} + \sum_{\mathbf{k}, \sigma} \left[V(\mathbf{k}) c_{\mathbf{k}\sigma}^{\dagger} f_{\sigma} + V^{*}(\mathbf{k}) f_{\sigma}^{\dagger} c_{\mathbf{k}\sigma} \right] + E_f n_f + U n_{f\uparrow} n_{f\downarrow}. \quad (2.1)$$

In second quantized notation, $c_{\mathbf{k}\sigma}^{\dagger}$ is the creation operator for a conduction electron with momentum \mathbf{k} and spin σ , f_{σ}^{\dagger} is the creation operator for an electron on the impurity orbital with spin σ , and $n_{\mathbf{k}\sigma} = c_{\mathbf{k}\sigma}^{\dagger} c_{\mathbf{k}\sigma}$ is the number operator.

Hybridization between the conduction electron sea and the impurity state is introduced through the second summation term in Equation 2.1. The $c_{\mathbf{k}\sigma}^{\dagger} f_{\sigma} + \text{H.c.}$ term allows electrons to tunnel between the impurity state and the degenerate conduction sea. The amplitude associated with this tunneling is given by first-order perturbation theory: $V(\mathbf{k}) = \langle \mathbf{k} | V_{\text{ion}} | f \rangle$, which depends on the overlap between the conduction and impurity orbitals.

The physics of the Anderson model can be understood by looking at two limits: the atomic limit, where hybridization is turned off, and the non-interacting limit, where the on-site Coulomb U term is turned off. Let us first examine the atomic limit, which models local moment formation on the impurity state. In this case, the relevant Hamiltonian is:

$$H = E_f n_f + U n_{f\uparrow} n_{f\downarrow}, \quad (2.2)$$

where E_f is the energy associated with singly occupying the impurity state and U is the Coulomb repulsion energy. The $\epsilon_{\mathbf{k}}$ term describing the conduction sea in Equation 2.1 has

been dropped since it simply shifts the zero in energy. When the impurity level is below the Fermi energy, E_f is negative, and the $E_f n_f$ term favors double occupation of the localized state. This competes with the Coulomb repulsion term U , which favors single occupancy. As long as Coulomb repulsion is larger than the energy associated with singly occupying the localized state, that is, when $2E_f + U$ is sufficiently larger than the Fermi energy, the impurity state will behave as a local magnetic moment. Later, we will see that the interaction between this local moment and the conduction sea gives rise to the Kondo effect.

We now turn to the non-interacting limit, where the effect of hybridization between the conduction sea and the impurity state becomes apparent. In this limit, the relevant Hamiltonian is:

$$H = \sum_{\mathbf{k},\sigma} \epsilon_{\mathbf{k}} n_{\mathbf{k}\sigma} + \sum_{\mathbf{k},\sigma} \left[V(\mathbf{k}) c_{\mathbf{k}\sigma}^\dagger f_\sigma + V^*(\mathbf{k}) f_\sigma^\dagger c_{\mathbf{k}\sigma} \right] + E_f n_f. \quad (2.3)$$

When this Hamiltonian is solved, hybridization between the conduction sea and the impurity level leads to a resonance of width Δ in the density of states given by Fermi's golden rule:

$$\Delta = \pi \sum_{\mathbf{k}} |V(\mathbf{k})|^2 \delta(\epsilon_{\mathbf{k}} - E_f). \quad (2.4)$$

This Friedel-Anderson resonance broadens the impurity density of states around E_f , and is the source of heavy fermion physics in the Anderson model.

To study the Kondo effect, which has an energy scale roughly a thousand times smaller than Coulomb interaction, we need to make use of the renormalization concept [4]. Renormalization is the idea that the low energy physics of a system only depends on certain features of the high energy physics, so the high energy physics can be folded into a small set of parameters that control the low energy physics [21]. When the high energy physics in the Anderson model are folded using renormalization, we are presented with a Hilbert space where the impurity states are singly occupied. Tunneling between the impurity state and the conduction sea can still occur via a virtual process that is second order in perturbation theory. The two-step virtual charge fluctuation processes will lower the energy of the singlet

2. Relevant Theoretical Concepts

configuration by an amount of the order $\Delta E = -J$, where:

$$J \sim V^2 \left[\frac{1}{-E_f} + \frac{1}{E_f + U} \right], \quad (2.5)$$

and V is the hybridization strength near the Fermi surface. Importantly, since E_f is below the Fermi energy, $J < 0$. Such an interaction forms an antiferromagnetic coupling between the localized moment and the conduction electrons. The resultant low energy Hamiltonian for this system gives us the Kondo model:

$$H_{\text{Kondo}} = \sum_{k\sigma} \epsilon_k c_{k\sigma}^\dagger c_{k\sigma} + J \mathbf{S}_c \cdot \mathbf{S}_f, \quad (2.6)$$

where \mathbf{S}_f is the spin of the localized impurity and \mathbf{S}_c is the spin density of the conduction electron sea. The scattering rate caused by this antiferromagnetic interaction has a logarithmic temperature dependence at third order. When the magnetic scattering exceeds that of phonon scattering at low temperatures, the material resistivity develops a minimum.

Another important result from the renormalization concept is an energy scale associated with the Kondo effect. Although the impurity moment is free at high energies, below some characteristic Kondo temperature defined by the conduction sea density of states ρ and the half-width of the electron band D ,

$$T_{\text{Kondo}} \sim D e^{-\frac{1}{2J\rho}}, \quad (2.7)$$

the interaction between the impurity moment and the conduction electron sea grows to a point where the impurity moment is screened into a singlet state. An adiabatically renormalized analogue to the Friedel-Anderson resonance introduced for the non-interacting Anderson model appears below the Kondo temperature, called the Abrikosov-Suhl or Kondo resonance [26, 27]. As the resonance produces a peak in the density of states at the Fermi energy, the Kondo system gains heavy fermion characteristics at low temperatures.

The treatment thus far only considers a single impurity state in the conduction sea. When

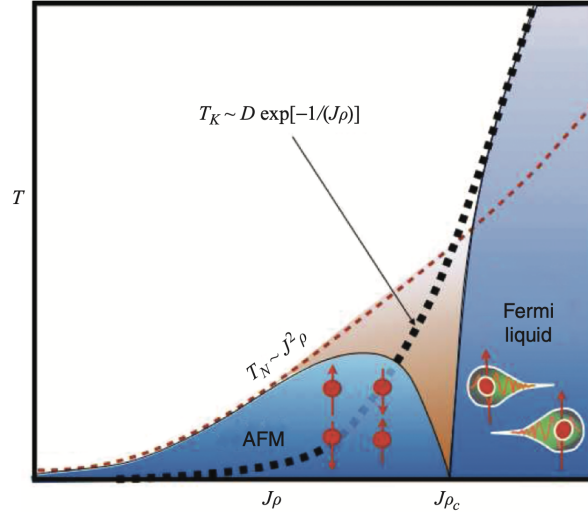


Fig. 2.1. The Doniach phase diagram for the Kondo lattice. Competition between the Kondo and RKKY interactions as a function of the hybridization strength J . For small interaction, the RKKY interaction is dominant, and the Kondo lattice forms and antiferromagnetic phase. As J increases, magnetic order is suppressed, and the system transitions to a heavy fermion phase. Figure adopted from [21].

a second impurity is introduced to the system, a long-range magnetic interaction arises:

$$H_{\text{RKKY}} = \frac{1}{2} \sum_{\mathbf{x}, \mathbf{x}'} -J^2 \chi(\mathbf{x} - \mathbf{x}') \mathbf{S}(\mathbf{x}) \cdot \mathbf{S}(\mathbf{x}'), \quad (2.8)$$

where \mathbf{x} and \mathbf{x}' are locations of the impurity atoms and $\chi(\mathbf{x})$ is the non-local susceptibility of the metal [28]. This long range interaction gives rise to a spin glass state for dilute concentration of magnetic impurities, while in dense systems the interaction typically gives rise to an ordered antiferromagnet with a Néel temperature of:

$$T_{\text{RKKY}} \sim J^2 \rho. \quad (2.9)$$

An extreme case of adding magnetic impurities to the conduction sea is to adopt the same treatment on an entire lattice of localized magnetic states. This idea was first proposed to

explain the strange lack of magnetic ordering in some heavy fermion compounds, despite experimental evidence of unpaired spinful f -electrons [29, 30]. In a Kondo lattice, a dense array of local moments interact with the conduction sea via the antiferromagnetic interaction J . Since both the Kondo and the RKKY effects depend on J , the two effects compete in such a system. For small interaction J , the RKKY interaction dominates, driving the system into an antiferromagnetic ground state. As J increases, the Kondo effect begins to dominate and drive the system into a heavy fermion regime. The competition between the RKKY and Kondo effects in a Kondo lattice system is depicted in the Doniach phase diagram, as shown in Fig. 2.1.

2.3 Quantization of quasiparticle energy in a magnetic field

The main discovery presented in this thesis is the existence of bulk quantum oscillations in the insulating phase of the correlated insulators YbB_{12} and FeSb_2 . As briefly described in Chapter 1, it is surprising to find quantum oscillations in insulators since our current understanding of the phenomenon is predicated on mobile electrons responding to an applied magnetic field.

The following section presents a semiclassical derivation of the Lifshitz-Kosevich (LK) formula based on the seminal work in Ref. [13], which describes quantum oscillations of the thermodynamic potential and density of states. We will derive the relationship between quantum oscillation frequency and the extremal Fermi surface cross-sectional area and the quantum oscillation damping factors due to finite temperature and impurity scattering, which will be applied to the quantum oscillations observed in YbB_{12} and FeSb_2 .

While this derivation of the LK formula is inherently non-interacting, the resultant formula has been successfully applied to a wide range of materials ranging from simple metals like bismuth [31] to strong-correlated systems such as heavy fermion materials [32] and superconductors [33]. Despite its success in capturing the behavior of metals, the application

of the LK formula to insulators would seem tenuous. Some new theoretical prescription is almost certainly required to model the physical origin of bulk quantum oscillations in unconventional insulators. Before such a new theoretical paradigm is constructed, it is informative to apply the existing LK formulation of quantum oscillations and examine how the physics of insulating phase quantum oscillations agree or deviate from our existing machinery.

2.3.1 Cyclotron motion

Let us first use the semiclassical approximation to introduce the concepts of cyclotron frequency and quasiparticle effective mass. The motion of a particle with charge q in a magnetic field \mathbf{B} is governed by the Lorentz force law:

$$\mathbf{F} = \hbar \dot{\mathbf{k}} = -q\mathbf{v} \times \mathbf{B}, \quad (2.10)$$

where \mathbf{k} is the wavevector and \mathbf{v} is the particle velocity [34]. The particle velocity is related to its energy ϵ by [13]:

$$\mathbf{v} = \frac{1}{\hbar} \nabla_{\mathbf{k}} \epsilon. \quad (2.11)$$

Since Eq. 2.10 implies that the force applied by a magnetic field is normal to the direction of particle motion, the Lorentz force does no work on the charged particle. The particle velocity is therefore normal to some constant energy surface. Similarly, $\dot{\mathbf{k}} = d\mathbf{k}/dt$, which is perpendicular to \mathbf{v} , is tangential to the constant energy surface (Fig. 2.2).

Consider the component of \mathbf{k} perpendicular to the direction of the field, k_{\perp} . From Eq. 2.10, the time dt it takes for the particle to traverse an infinitesimal element dk_{\perp} of the orbit is:

$$dt = dk_{\perp} \frac{\hbar^2}{qB \frac{\partial \epsilon}{\partial k_{\perp}}} = dk_{\perp} \frac{\hbar^2}{qB} \frac{\Delta k_{\perp}}{\Delta \epsilon}. \quad (2.12)$$

Let the area element da be the area between the two k_{\perp} orbits corresponding to energies ϵ

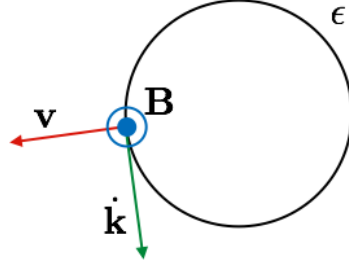


Fig. 2.2. Motion of charged particle in magnetic field. Relative directions of the applied magnetic field \mathbf{B} , the particle velocity \mathbf{v} , and the change in momentum $\dot{\mathbf{k}}$. The motion of the particle in the direction of the applied magnetic field is unaffected by the magnetic field.

and $\epsilon + \Delta\epsilon$. The incremental change of this area is given by $\Delta(da) = dk_{\perp}\Delta k_{\perp}$, meaning:

$$dt = \frac{\hbar^2}{qB} \frac{\Delta(da)}{\Delta\epsilon}. \quad (2.13)$$

Integrating this over a full period $2\pi/\omega_c$, we find:

$$\frac{1}{\omega_c} = \frac{\hbar^2}{2\pi qB} \left(\frac{\partial a}{\partial \epsilon} \right)_{k_{\parallel}}, \quad (2.14)$$

where ω_c is the cyclotron frequency and k_{\parallel} , the component of \mathbf{k} parallel to the magnetic field, is held constant. Drawing an analogy to the classic circular orbit frequency $\omega = eB/m_e$, we can define the quasiparticle effective mass as [13]:

$$m^* = \frac{\hbar^2}{2\pi} \left(\frac{\partial a}{\partial \epsilon} \right)_{k_{\parallel}}, \quad (2.15)$$

such that the semiclassical cyclotron frequency becomes:

$$\omega_c = \frac{qB}{m^*}. \quad (2.16)$$

2.3.2 The Onsager relation

Another important relationship that can be derived using the semiclassical approach is the Onsager relation, which relates the size of charged particle orbits in real space to that in k -space [35]. Following Onsager's original derivation, consider the Bohr-Sommerfeld quantization rule:

$$\oint \mathbf{p} \cdot d\mathbf{x} = (n + \gamma) 2\pi\hbar, \quad (2.17)$$

where \mathbf{p} and \mathbf{x} are the canonical momentum and position operators, respectively, n is an integer, and γ is the phase factor. For a charged particle under the influence of a magnetic field, the canonical position and momentum operators are [13]:

$$\mathbf{p} = \hbar\mathbf{k} - q\mathbf{A} \quad (2.18)$$

$$\mathbf{x} = \mathbf{R}_\perp, \quad (2.19)$$

where \mathbf{R}_\perp is the component of the real space position vector \mathbf{R} perpendicular to the magnetic field \mathbf{B} and q is the charge on the particle. In order to relate \mathbf{k} to a real space variable, integrate the Lorentz force law in Eq. 2.10 to find:

$$\hbar(\mathbf{k} - \mathbf{k}_0) = -q(\mathbf{R} - \mathbf{R}_0) \times \mathbf{B}. \quad (2.20)$$

Since the particle motion parallel to the magnetic field is unaffected by the field itself (which therefore implies the particle motion is generally helical), the component relevant for cyclotron motion is perpendicular to the field:

$$|\mathbf{R}_\perp - \mathbf{R}_{\perp 0}| = \frac{\hbar}{qB} |\mathbf{k} - \mathbf{k}_0|. \quad (2.21)$$

We therefore see that the \mathbf{R}_\perp orbit is a scaled version of the \mathbf{k} orbit.

Substituting the canonical momentum and position operators \mathbf{p} and \mathbf{x} into Eq. 2.17 and using Stoke's theorem [34] to rewrite the vector potential \mathbf{A} in terms of magnetic field \mathbf{B} ,

we find:

$$\mathbf{B} \cdot \oint (\mathbf{R} \times d\mathbf{R}_\perp) - \int_{\mathcal{S}} \mathbf{B} \cdot d\mathbf{S} = (n + \gamma) \frac{2\pi\hbar}{q}, \quad (2.22)$$

where \mathcal{S} denotes integration over the area of the orbit in real space. We can write \mathbf{R} as a sum of components parallel and perpendicular to the magnetic field, $\mathbf{R} = \mathbf{R}_\perp + \mathbf{R}_\parallel$. The parallel component \mathbf{R}_\parallel does not contribute to the integration since its cross product with \mathbf{R}_\perp is perpendicular to \mathbf{B} . As a result,

$$\mathbf{B} \cdot \oint (\mathbf{R} \times d\mathbf{R}_\perp) = B \left| \oint (\mathbf{R}_\perp \times d\mathbf{R}_\perp) \right| = 2B\alpha, \quad (2.23)$$

where α is the area of the \mathbf{R}_\perp orbit in real space. The second term on the left-hand side of Eq. 2.22 is the magnetic flux through the are of the \mathbf{R}_\perp orbit:

$$\int_{\mathcal{S}} \mathbf{B} \cdot d\mathbf{S} = \Phi_{\mathbf{B}} \equiv B\alpha. \quad (2.24)$$

From Eq. 2.21, we know that the k -space orbit area a is related to the real space orbit area α by $\alpha = (\hbar/eB)^2 a$. Therefore, the area of the orbit in k -space is given by:

$$a(\epsilon, k_\parallel) = (n + \gamma) \frac{2\pi q B}{\hbar}. \quad (2.25)$$

2.3.3 Landau levels

We can now treat the cyclotron problem quantum mechanically to see how a magnetic field quantizes electron energy states. This is essentially a quantum harmonic oscillator problem in two dimensions combined with a free-electron problem along the \hat{z} direction [8]. Imagine a magnetic field aligned along the \hat{z} -axis with the following vector potential:

$$\mathbf{A} = (0, Bx, 0), \quad (2.26)$$

which has some arbitrary field strength B . The magnetic field for this vector potential is given by $\mathbf{B} = \nabla \times \mathbf{A} = B\hat{z}$.

The Hamiltonian for a charged particle in a vector potential is given by:

$$\mathbf{H} = \frac{1}{2m} (\mathbf{p} - q\mathbf{A}) \cdot (\mathbf{p} - q\mathbf{A}) + V(\mathbf{r}, t), \quad (2.27)$$

where q is the charge of the particle. For simplicity, we assume there is no scalar potential, so $V(\mathbf{r}, t) = 0$. Substituting the vector potential and the momentum operator $\mathbf{p} = -i\hbar\nabla$ into the Hamiltonian, we find:

$$H = -\frac{\hbar^2}{2m} \left[\frac{\partial^2}{\partial x^2} + \left(\frac{\partial}{\partial y} - \frac{iqBx}{\hbar} \right)^2 + \frac{\partial^2}{\partial z^2} \right]. \quad (2.28)$$

Since the magnetic field exerts no force in the \hat{z} -direction, we can disregard the \hat{z} -term and add a quadratic dispersion term in the \hat{z} -direction to the final expression.

From translational invariance in the \hat{y} -direction (the Hamiltonian does not depend on the position in y), the solution to Schrödinger's equation is a free particle in y . Using an ansatz of the form $\psi_{n,k}(x, y) = e^{iky} f_n(x)$, we have:

$$\begin{aligned} H\psi_{n,k}(x, y) &= -\frac{\hbar^2}{2m} \left[e^{iky} f_n''(x) - k^2 e^{iky} f_n(x) + \frac{2kqBx}{\hbar} e^{iky} f_n(x) - \left(\frac{qBx}{\hbar} \right)^2 e^{iky} f_n(x) \right] \\ &= E e^{iky} f_n(x), \end{aligned} \quad (2.29)$$

where the second equality is from the time independent Schrödinger's equation. Cancelling out e^{iky} from both sides and defining a length scale $l = \sqrt{\hbar/qB}$, we find:

$$-\frac{\hbar^2}{2ml^2} \left[l^2 f_n''(x) - \left(\frac{x}{l} - kl \right)^2 f_n(x) \right] = E f_n(x). \quad (2.30)$$

Now substitute in the cyclotron frequency, $\omega_c = qB/m$, and transform variables $x \rightarrow \bar{x} = (x/l - kl)$,

$$-\frac{\hbar\omega_c}{2} [l^2 f_n''(\bar{x}) - \bar{x}^2 f_n(\bar{x})] = E f_n(\bar{x}). \quad (2.31)$$

The solution to this quantum harmonic oscillator problem is a series of Hermite polyno-

2. Relevant Theoretical Concepts

mials $H_n(x)$ [36] centered at $x_k = -l^2k$. In other words, the wavefunctions that solve the Hamiltonian given in Eq. 2.28 are:

$$\psi_{n,k}(x, y) = e^{iky} H_n \left(\frac{x}{l} - kl \right) e^{-(x-x_k)^2/2l^2}. \quad (2.32)$$

The eigenvalues of this family of wavefunctions are known as Landau levels, which have quantized energy with index n :

$$\epsilon_n = \hbar\omega_c \left(n + \frac{1}{2} \right). \quad (2.33)$$

Since the Landau levels are independent of k , the degeneracy of each Landau level is determined by the distinct number of k values that generate a state within that Landau level [37]. The wavevector k can take on a range of values consistent with the confinement of the system in the y -direction. Let L_x and L_y be the spatial extent of the sample in the x - and y -directions, respectively. The wavevector $k = 2\pi/\lambda$, where λ is the wavelength, can be written as:

$$k_m = \frac{2\pi m}{L_y}, \quad (2.34)$$

for some integer m . Since each Landau level is centered at $x_k = l^2k$, the maximum number of states in each Landau level is given by $L = l^2k_{N_{\max}}$. In other words, the degeneracy of each Landau level in the xy -plane is given by:

$$N_{\max} = \frac{L_x L_y}{2\pi l^2} = \frac{qBL_x L_y}{2\pi\hbar}. \quad (2.35)$$

There is a physical interpretation for this degeneracy. The total magnetic flux in each Landau level is the product of the magnetic field and the area of the sample, $BL_x L_y$. This quantity must be equal to the number of electrons in each level times the flux quantum, h/e .

When the \hat{z} -direction is taken into account, the total degeneracy of a Landau level is:

$$D = \frac{qBV}{2\pi^2\hbar}, \quad (2.36)$$

where V is the real space volume of the sample, and a factor of 2 is included for spin degeneracy [13].

From Eq. 2.33, we can get an intuitive understanding of the quantum oscillation frequency [38]. Quantum oscillations are caused by peaks in the thermodynamic potential when successive Landau levels pass through the Fermi level E_F . We can first rewrite the energy levels in terms of the cyclotron effective mass m^* :

$$\epsilon_n = \hbar\omega_c \left(n + \frac{1}{2} \right) = \frac{q\hbar B}{m^*} \left(n + \frac{1}{2} \right). \quad (2.37)$$

Let B_n denote the field strength at which the n^{th} Landau level passes through the Fermi level. The frequency F of quantum oscillations can be written as:

$$\frac{1}{F} = \frac{1}{B_n} - \frac{1}{B_{n-1}} = \frac{q\hbar}{m^* E_F}. \quad (2.38)$$

Consider the simple case of the Fermi surface having a circular cross section, $\mathcal{A} = \pi k_F^2$. Since the Fermi wavevector k_F is related to the Fermi energy by $E_F = \hbar^2 k_F^2 / 2m^*$, the period of oscillation can then be rewritten as:

$$\frac{1}{F} = \frac{2\pi q}{\hbar \mathcal{A}}. \quad (2.39)$$

Therefore, the quantum oscillation frequency is proportional to the cross-sectional area of the Fermi surface perpendicular to the magnetic field. This same treatment can be performed using Eq. 2.25 by setting the area of orbit in k -space equal to the Fermi surface cross-sectional area $a = \mathcal{A}$, yielding the same result. More specifically, since the thermodynamic potential undergoes a sharp change when a Landau level enters or exits an arbitrarily shaped Fermi surface, the oscillation frequency is proportional to the extremal cross-sectional area of the Fermi surface [13].

2.4 Quantum oscillatory behavior in a magnetic field

In the previous section, we have seen how a magnetic field induces the thermodynamic potential to undulate with a frequency proportional to the extremal Fermi surface cross-sectional area. In this section, we will derive an expression for sample magnetization as a function of magnetic field, which is relevant for magnetic torque quantum oscillations. We will further explore the difficulty of analytically describing quantum oscillations in electrical resistivity, and discuss an approximate description of the behavior using density of states at the Fermi energy.

2.4.1 The thermodynamic potential

The magnetization \mathbf{M} of a collection of charged particles is given by:

$$\mathbf{M} = -(\nabla_{\mathbf{B}}\Omega)_{\mu}, \quad (2.40)$$

where Ω is the thermodynamic potential and μ is the chemical potential. The thermodynamic potential of a collection of particles is defined as:

$$\Omega = -k_{\text{B}}T \ln(\mathcal{Z}), \quad (2.41)$$

where k_{B} is Boltzmann's constant and T is temperature [39]. The grand partition function \mathcal{Z} is defined as:

$$\mathcal{Z} = \sum_i e^{(\mu N_i - E_i)/k_{\text{B}}T}, \quad (2.42)$$

where N_i is the number of particles with energy E_i . For non-interacting fermions that obey the Pauli exclusion principle, the grand potential is:

$$\Omega = -k_{\text{B}}T \ln \left(1 + e^{(\mu - \epsilon_i)/k_{\text{B}}T} \right). \quad (2.43)$$

Using the degeneracy from Eq. 2.36, the thermodynamic potential for a system of charged particles in a magnetic field can be written as:

$$\Omega = -k_{\text{B}}T \int_{-\infty}^{\infty} dk_{\parallel} \frac{qBV}{2\pi^2\hbar} \sum_n \ln \left(1 + e^{(\mu - \epsilon_n)/k_{\text{B}}T} \right), \quad (2.44)$$

where n refers to solutions to the Onsager relation in Eq. 2.25. Technically, at this point it only remains to differentiate Ω with respect to the magnetic field \mathbf{B} to obtain an equation for de Haas-van Alphen oscillations in magnetization [40]. To see the physics at work, we go about this process by first examining the $T \rightarrow 0$ limit, before considering temperature as a phase smearing effect [13].

2.4.2 Magnetization as $T \rightarrow 0$

In the $T \rightarrow 0$ limit, the thermodynamic potential simplifies to:

$$\delta\Omega = D \sum_n (\epsilon_n - \mu), \quad (2.45)$$

where D is the degeneracy in Eq. 2.36. This sum can be approximated as an integral using the Euler-Maclaurin formula; up to second order, the formula is given by:

$$\sum_0^N f(n) = \int_0^N f(n)dn + \frac{1}{2} [f(N) + f(0)] + \frac{1}{12} [f'(N) - f'(0)]. \quad (2.46)$$

Applying this to Eq. 2.45, we have:

$$\frac{\delta\Omega}{D} = \int_0^N (\epsilon_n - \mu)dn + \frac{1}{2}(\epsilon_N + \epsilon_0) + \frac{1}{12} \left[\left(\frac{\partial\epsilon}{\partial n} \right)_{n=N} - \left(\frac{\partial\epsilon}{\partial n} \right)_{n=0} \right], \quad (2.47)$$

2. Relevant Theoretical Concepts

where N is the highest occupied state at $T = 0$ (in other words, where $\epsilon_N = \mu$). We now define a continuous variable $x = n + 1/2$ for the Onsager relation in Eq. 2.25:

$$a(\epsilon, k_{\parallel}) = x \left(\frac{2\pi q B}{\hbar} \right), \quad (2.48)$$

and also a variable X that corresponds to the extremal Fermi surface area perpendicular to the magnetic field:

$$\mathcal{A}(\mu, k_{\parallel}) = X \left(\frac{2\pi q B}{\hbar} \right). \quad (2.49)$$

By changing variables in Eq. 2.47 from $n \rightarrow x$, we find that the oscillatory term of the thermodynamic potential is given by:

$$\delta\tilde{\Omega} = \delta k_{\parallel} \frac{q\beta V B^2}{4\pi^2 \hbar} \left\{ \left[X - \left(N + \frac{1}{2} \right) \right]^2 - \left[X - \left(N + \frac{1}{2} \right) \right] + \frac{1}{6} \right\}, \quad (2.50)$$

where $\beta = q\hbar/m^*$. By definition, the area of the Fermi surface \mathcal{A} encloses the largest occupied Landau tube. Since successive Landau tubes have a separation of $N = 1$, X is only defined for $N + 1/2 \leq X \leq N + 3/2$. Whenever X goes beyond this range, the value of N has to be increased or decreased by one, thereby making $\delta\tilde{\Omega}$ periodic in X with a period of 1. In other words, $\delta\tilde{\Omega}$ is periodic in $1/B$ with a period of $2\pi q/\hbar\mathcal{A}$. Eq. 2.50 can be transformed into a harmonic series through Fourier analysis:

$$\delta\tilde{\Omega} = \delta k_{\parallel} \frac{q\beta V B^2}{4\pi^2 \hbar} \sum_{p=1}^{\infty} \frac{1}{\pi^2 p^2} \cos \left[2\pi p \left(X - \frac{1}{2} \right) \right]. \quad (2.51)$$

The oscillatory component of the magnetic moment parallel to the magnetic field is given by:

$$\delta\tilde{M} = - \left(\frac{\partial (\delta\tilde{\Omega})}{\partial B} \right)_{\mu}. \quad (2.52)$$

This term can be calculated by either differentiating Eq. 2.50 and taking its Fourier analysis, or differentiating Eq. 2.51 directly:

$$\delta\widetilde{M} = -\beta\delta N_0 \sum_{p=1}^{\infty} \frac{\sin\left[2\pi p\left(X - \frac{1}{2}\right)\right]}{\pi p}. \quad (2.53)$$

The full magnetization, after integrating $\delta\widetilde{\Omega}$ over k_{\parallel} and differentiating, becomes:

$$\widetilde{M}_{\parallel} = -\beta F V \sqrt{\frac{q^3 B}{2\hbar^3 \pi^5 \left(\frac{\partial^2 \mathcal{A}}{\partial k_{\parallel}^2}\right)}} \sum_{p=1}^{\infty} \frac{1}{p^{3/2}} \sin\left[2\pi p\left(\frac{F}{B} - \frac{1}{2}\right) \pm \frac{\pi}{4}\right] \quad (2.54)$$

$$\widetilde{M}_{\perp} = -\frac{1}{F} \frac{\partial F}{\partial \theta} \widetilde{M}_{\parallel}. \quad (2.55)$$

where F is the de Haas-van Alphen oscillation frequency defined using the extremal cross-sectional area of the Fermi surface,

$$F = A \left(\frac{\hbar}{2\pi q} \right). \quad (2.56)$$

2.4.3 Oscillations in density of states

Quantum oscillations in electrical resistivity, known as the Shubnikov-de Haas oscillations [41], is more complicated compared to quantities that can be directly derived from the thermodynamic potential, since resistivity depends on details of electron scattering in a magnetic field. Pippard has put forward a qualitative argument that resistivity oscillations can be approximated using the fact that the probability of scattering is proportional to the number of states the electrons can be scattered into [42]. This probability, which determines the electronic relaxation time τ and resistivity, oscillates along with the density of states at the Fermi energy $\mathcal{D}(\mu)$. The density of states from a two-dimensional slice of k -space of thickness

dk_{\parallel} is given by [13]:

$$\delta\mathcal{D}(\epsilon) = dk_{\parallel} \left(\frac{qBV}{2\pi^2\hbar} \right) \sum_{r=0}^{\infty} \left(\frac{da}{d\epsilon} \right)_{k_{\parallel}} \delta \left[a(\epsilon, k_{\parallel}) - \left(r + \frac{1}{2} \right) \frac{2\pi qB}{\hbar} \right]. \quad (2.57)$$

The delta function is included since permitted states only come into consideration when a Landau tube crosses the Fermi surface. Expressing $(da/d\epsilon)_{k_{\parallel}}$ in terms of the quasiparticle effective mass m^* and changing variables to x again:

$$\delta\mathcal{D}(\epsilon) = dk_{\parallel} \frac{m^*V}{2\pi^2\hbar^2} \sum_{r=0}^{\infty} \delta \left[x - \left(r + \frac{1}{2} \right) \right]. \quad (2.58)$$

This can be transformed through Fourier analysis into a sinusoidal function:

$$\delta\mathcal{D}(\epsilon) = dk_{\parallel} \frac{m^*V}{2\pi^2\hbar^2} \left\{ 1 + 2 \sum_{p=1}^{\infty} \cos \left[2\pi p \left(\frac{F}{B} - \frac{1}{2} \right) \right] \right\}, \quad (2.59)$$

for the specific case of $\epsilon = \mu$. The oscillatory component of the full density of states after integrating over k_{\parallel} is given by:

$$\tilde{\mathcal{D}}(\epsilon) = m^*V \sqrt{\frac{2qB}{\pi^3\hbar^5 \left(\frac{\partial^2 \mathcal{A}}{\partial k_{\parallel}^2} \right)}} \sum_{p=1}^{\infty} \frac{1}{p^{1/2}} \cos \left[2\pi p \left(\frac{F}{B} - \frac{1}{2} \right) \pm \frac{\pi}{4} \right]. \quad (2.60)$$

We therefore see that the density of states at the Fermi level, and by an approximate extension the electrical resistivity, oscillates periodically in inverse magnetic field similar to the thermodynamic potential.

2.4.4 Damping factors

In real-world experiments, the quantum oscillation amplitude will deviate from the idealized results calculated in the $T \rightarrow 0$ limit. Effects such as finite temperature, impurity scattering,

sample inhomogeneity, and electron spin cause phase smearing, which reduce the oscillation amplitude from the $T \rightarrow 0$ limit. For instance, in pure metals, sample homogeneity causes the magnetization oscillation phase to vary throughout the sample. Even if the sample is locally perfect, different regions within the sample can have appreciably different phases due to variations in strain and crystal orientation. This causes the average amplitude of the magnetization oscillation to be less than the “perfect” value within each local region [13].

The result of this phase smearing is captured by the Lifshitz-Kosevich formula [43], which expresses the quantum oscillation amplitude as the $T \rightarrow 0$ case multiplied by a series of damping factors:

$$\widetilde{M} = M_0 R_T R_D \sin\left(\frac{2\pi F}{B} + \phi\right). \quad (2.61)$$

R_T and R_D are the most commonly relevant damping factors, attributed to finite temperature and impurity scattering and sample inhomogeneity, respectively [44]. ϕ is the phase factor related to the berry phase ϕ_B by $\phi = \phi_B + \delta - \pi$, where $\delta = 0$ and $\pm\pi/4$ for two-dimensional and three-dimensional Fermi surfaces, respectively. M_0 is the infinite field, zero spin-splitting amplitude given by [12]:

$$M_0 = -\frac{\mu_B m_e}{2\pi^4 m^*} \sqrt{\frac{A^3 B}{F \left| \frac{\partial^2 A}{\partial k_{\parallel}^2} \right|}}. \quad (2.62)$$

The temperature damping factor is given by:

$$R_T = \frac{X}{\sinh(X)}, \quad (2.63)$$

where,

$$X = \frac{2\pi^2 k_B T m^*}{e\hbar B}. \quad (2.64)$$

The temperature damping factor is useful since the only parameter that is not experimentally controlled is m^* , the quasiparticle effective mass. By recording the quantum oscillation amplitude at various temperatures and fitting to R_T , we can extract the quasiparticle effective mass m^* for the sample material.

2. Relevant Theoretical Concepts

Another relevant damping factor is the Dingle damping factor, which accounts for the attenuation of oscillation amplitude due to impurity scattering:

$$R_D = \exp\left(-\frac{\pi m_b}{eB\tau}\right) \equiv \exp\left(-\frac{B_D}{B}\right), \quad (2.65)$$

where m_b is the band mass calculated from mean-field density functional theory band structure, and τ is the scattering time. The Dingle damping term can be used to extract the scattering time constant τ and to compare the purity of different samples by fitting an envelope to the growth of quantum oscillation amplitude against the magnetic field to extract B_D . Finding the scattering time from R_D is not always feasible, however, since the band mass m_b is not necessarily straightforward to calculate.

Chapter 3

Experimental Methods

The data presented in this thesis were collected on two strongly correlated insulators, YbB_{12} and FeSb_2 . Both materials were grown by our group's collaborators, prepared and characterized in Cambridge, then measured up to high magnetic fields at various national laboratories in Florida, Germany, the Netherlands, and Japan. This chapter provides an overview of the growth methods and elemental characterization results from our collaborators, the procedure for preparing samples in Cambridge, the high field measurement techniques, as well as numerical methods used to analyze the measured quantum oscillations.

3.1 Sample Preparation

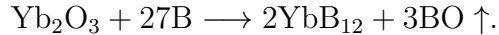
3.1.1 Sample Growth

YbB_{12} growth

YbB_{12} forms a face-centered cubic lattice with a NaCl-like structure, where Yb atoms and B_{12} octahedra respectively take the place of Na and Cl [45], as shown in Fig. 3.1A. For our samples, polycrystalline YbB_{12} was synthesized by our collaborator Natalya Shitsevalova's

3. Experimental Methods

group at The National Academy of Sciences of Ukraine in Kiev using borothermal reduction. 99.998%wt purity Yb_2O_3 powder was reacted with 99.9%wt purity amorphous B at 1700°C under vacuum [46], following the below reaction:



The polycrystalline YbB_{12} powder was isostatically pressed into a cylindrical rod and sintered at 1600°C in Ar gas flow for several hours to produce the starting material for single crystal growth using an image furnace.

Single crystals of YbB_{12} were grown from sintered polycrystalline rods using the traveling solvent floating zone technique with a 3 kW four-mirror xenon arc lamp optical image furnace by our collaborator Monica Ciomaga Hatnean in Prof. Geetha Balakrishnan's group at Warwick University [47–49]. The growths were performed in a Ar + 3% H_2 reducing atmosphere at a growth rate of 18 mm/hr with the feed and seed rods counter-rotating at 20-30 rpm.

Elemental composition analysis, performed on the grown single crystals using a FEI Philips XL30 sFEG scanning electron microscope at Warwick University, found an atomic ratio between Yb and B comparable to the stoichiometric ratio of 1 : 12 and distinct from the ratios for the neighboring phases YbB_6 and YbB_{66} [48].

The phase of the grown crystal was confirmed using powder X-ray diffraction at Warwick University. Rietveld refinement using the Bruker TOPAS software showed a dominant YbB_{12} phase and a lattice constant of $7.4686(1) \text{ \AA}$, agreeing well with published results [46]. A representative powder X-ray diffraction spectrum with labels for calculated YbB_{12} peaks is shown in Fig. 3.1C.

Single crystallinity is confirmed using Laue X-ray imaging with a Multiwire Laue back-scattering camera in the Cavendish Laboratory. A Laue spectrum taken along the [001] crystallographic direction on one of the samples used in high field measurements is shown in Fig. 3.1B.

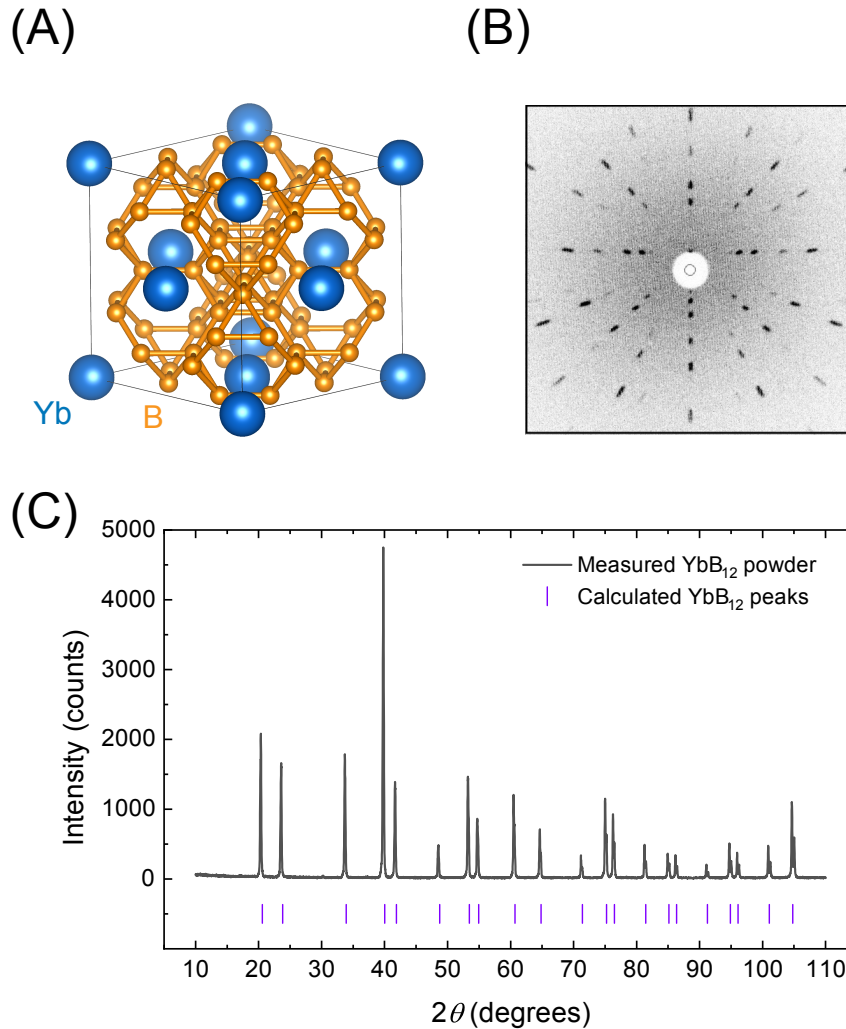


Fig. 3.1. Crystal structure of YbB₁₂. (A) A schematic crystal structure of YbB₁₂. The Yb atoms, shown in blue, form a FCC cage interspersed with octahedra formed of 12 B atoms, shown in orange. (B) A Laue back scattering image of a single crystal YbB₁₂ sample that was grown by our collaborator in Warwick University, taken along the [001] crystallographic direction. High single crystallinity is evident, with no signs of co-growth. (C) Powder X-ray diffraction data taken on samples from the batch that was used in high field measurements, with tick labels indicating the location of calculated peaks for YbB₁₂ [45].

FeSb₂ growth

FeSb₂ forms an orthorhombic lattice with a marcasite crystal structure, as shown in Fig. 3.2A. Single crystals of FeSb₂ were grown using the chemical vapour transport (CVT) technique by our collaborator Ke-Jun Xu in Prof. Zhi-Xun Shen’s group at Stanford University. To perform CVT growth, stoichiometric ratio amounts of 99.995%wt Fe and 99.999%wt Sb were placed at one end of a quartz tube along with ~ 1 mg/cm³ of elemental iodine I₂ as the transport agent, and sealed under vacuum. Growth was conducted with a 750°C – 650°C temperature gradient and maintained for one week. After the growth, the charge end was quenched to condense any remaining vapour in order to preserve pristine surfaces on the FeSb₂ crystals [50].

Elemental composition analysis was performed on FeSb₂ by powder X-ray diffraction using the Malvern Panalytical X’pert and Empyrean diffractometers in Stanford University. All observed peaks correspond to known crystallographic phases of FeSb₂. Rietveld refinement showed a marcasitic crystal structure with lattice constants of $a = 5.833$ Å, $b = 6.538$ Å, and $c = 3.197$ Å. A representative spectrum with labels for calculated FeSb₂ peaks is shown in Fig. 3.2C.

The as-grown FeSb₂ crystals were also aligned using the Multiwire Laue camera system in the Cavendish Laboratory. Since FeSb₂ forms an orthorhombic crystal structure, many more distinct rotation planes can be chosen when aligning these samples than when aligning YbB₁₂. A representative Laue image evidencing high crystallinity is shown in Fig. 3.2B. Details on sample alignment and rotation will be discussed in Section 3.2.2.

3.1.2 Sample sectioning

As-grown boules of single crystal YbB₁₂ were cut using the K. D. Unipress WS-22 high precision wire saw to sizes appropriate for high field measurements. Samples for capacitive torque magnetometry are typically $\approx 1 \times 1 \times 0.4$ mm³ in size, while samples for electrical transport measurements typically have surface areas of $\approx 0.5 \times 0.5$ mm² and are made as

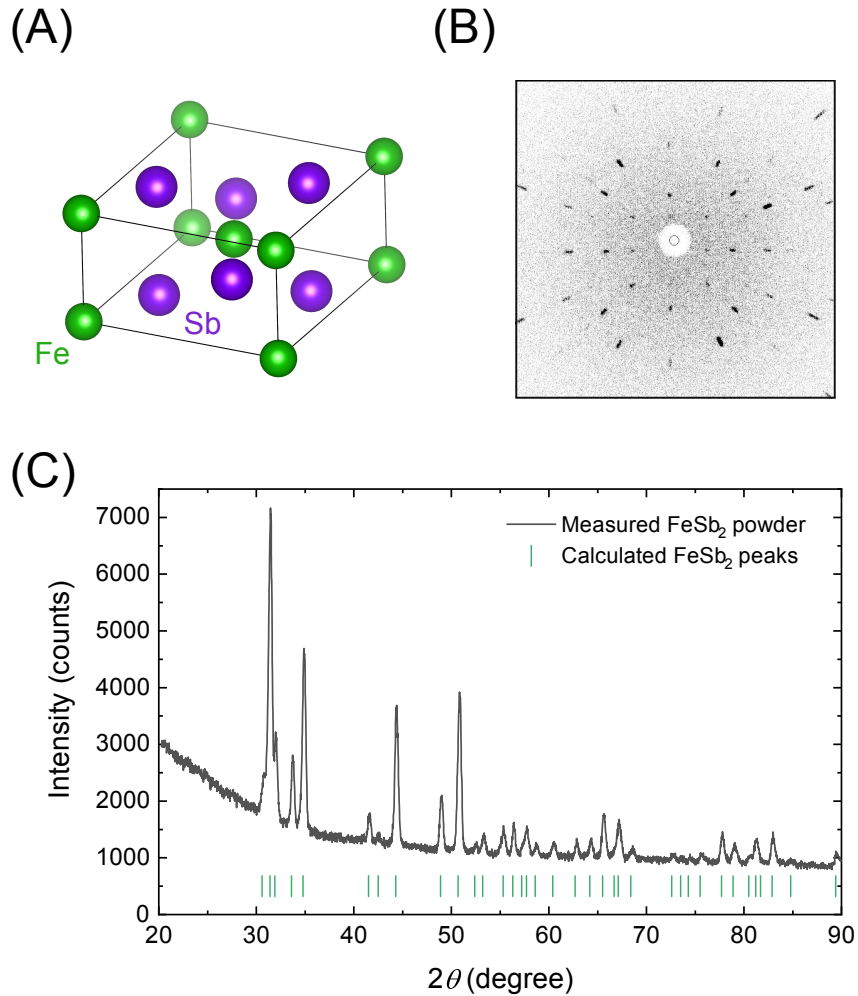


Fig. 3.2. FeSb₂ crystal structure. (A) A schematic crystal structure of FeSb₂. Fe atoms are shown in green, while Sb atoms are shown in purple. (B) A Laue back scattering image of a single crystal FeSb₂ sample grown by our collaborators in Stanford University, taken along the [001] crystallographic direction. High single crystallinity is evident, with no signs of co-growth. (C) Powder X-ray diffraction data taken using samples from one of the growth batches that was used in high field measurements. Tick labels indicate the location of calculated peaks for FeSb₂ [51].



Fig. 3.3. Wire saw used for sample sectioning. A picture of the K. D. Unipress WS-22 wire saw used to cut samples taken from the company website.

thin as can practically be cut and manipulated, typically less than 0.1 mm.

Fig. 3.3 shows a photograph of the WS-22 wire saw from the K. D. Unipress website. The arms of the wire saw, holding a taut tungsten wire, are driven back and forth by a motor to grind a particulate slurry and cut the object of interest. Tungsten wires 50 μm and 25 μm in diameter are used. The particulate slurry is made from suspending either 600 grit silicon carbide powder or 10 μm diameter diamond powder in a glycerol solvent. The fine tungsten wire and powders were chosen to minimize damage to the cut sample surfaces.

FeSb_2 single crystals grown via the CVT technique are multifaceted and typically have a maximum volume of $\approx 1 \times 1 \times 1 \text{ mm}^3$. These are typically not sectioned further to avoid straining the samples, except when a precise alignment is required for applying current in electrical transport measurements. In these cases, a single cut was made perpendicular to the tip of an as-grown crystal to produce a pyramid-shaped sample. One such sample was used in pulsed magnetic field measurements to determine the dependence of the gap size in applied fields, which will be described in Chapter 5.

3.1.3 Electropolishing

Despite efforts to minimize damage caused by the cutting process, surfaces on cut samples of YbB_{12} often show visible signs of mechanical scratches and burn marks. To avoid such extraneous damages and strain from affecting measurement results, an electrolytic polisher is used to chemically remove damaged surface layers on cut samples.

Fig. 3.4 shows the South Bay Technologies, Inc. Model 451 electrolytic crystal polisher that was used to electropolish samples. A chemical reagent is kept cool in the tub with liquid nitrogen and soaked up by the teflon cloth covering the rotating polisher wheel. The sample, functioning as the anode, is brought into contact with the wheel, which functions as the cathode. An electric current is passed through the sample to drive the chemical reaction to remove sample material.

The optimal parameters for the applied current, temperature, reagent choice, and reagent concentration for a particular material is often found through trial-and-error [52]. In the case of YbB_{12} , good results were produced with electrical currents of 10–20 mA at temperatures of 8–12°C using 1% perchloric acid by volume in methanol. YbB_{12} samples typically need to be polished for ~ 10 mins to achieve a smooth, mirror-like surface finish without visible damage.

More recently, a new method of applying current to the sample was adopted with the aim of thinning YbB_{12} samples to less than 100 μm in thickness in a controlled manner. Instead of the polishing wheel, a mesh ladle made from platinum wires is used to immerse samples into the perchloric acid bath. The same current, temperature range, and acid concentration is used. This method has the advantage of polishing all sides of the crystal simultaneously, which avoids the risk of polishing the sample into a wedge shape if it is brought to the polishing wheel at an angle. The lack of moving parts also allows controlled polishing to thicknesses below 100 μm , where it becomes exceedingly difficult to manually maneuver the sample to the polishing wheel without hitting the sample against the wheel. Samples of less than 20 μm in thickness have been produced using the mesh ladle method.

3. Experimental Methods

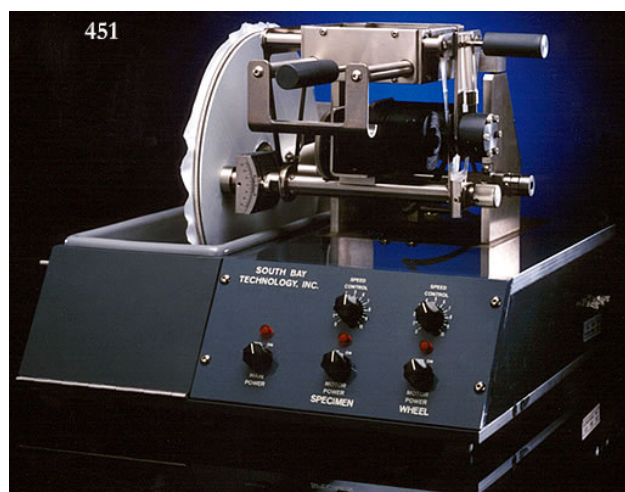


Fig. 3.4. Electropolisher used to remove surface damage and strain from cut samples. A picture of the South Bay Technologies Model 451 electropolisher taken from the company website.

3.2 High Magnetic Field Measurements

The main findings presented in this thesis were acquired through high magnetic field measurements performed at national laboratories around the world. In order to select the highest quality samples for high field measurements, the cut and electropolished samples are subject to a series of low field characterization measurements in Cambridge. Each sample is imaged using our X-ray Laue backscattering camera to confirm their single crystallinity and lack of co-growth or grain boundaries. Their resistivity as a function of temperature is measured at various applied magnetic fields using a Quantum Design Inc. Physical Property Measurement System (PPMS) in order to determine the gap size and inverse residual resistivity ratio (iRRR), the latter of which has been shown to reflect sample quality [53, 54]. The specific heat capacity as a function of temperature is measured on select samples to look for finite linear coefficients. Magnetization as a function of applied magnetic field is measured on select samples to determine the magnetic impurity content. The typical results of these low field characterization measurements will be detailed in Chapter. 4 and Chapter 5 for YbB_{12} and FeSb_2 , respectively.

In this section, I will describe the setup of the high field experiments that make up the bulk of this thesis. I will begin with a brief overview of the electromagnets used, followed by descriptions for the three primary measurement techniques – capacitive torque magnetometry, four-point electrical transport, and proximity detector oscillator.

3.2.1 High Magnetic Fields

High magnetic field data presented in this thesis were collected across four international high magnetic field laboratories: National High Magnetic Field Laboratory (NHMFL) in Tallahassee, Florida, High Field Magnet Laboratory (HFML) in Nijmegen, the Netherlands, Hochfeld-Magnetlabor Dresden (HLD) in Dresden, Germany, and the International Mega-Gauss Science Laboratory in the Institute for Solid State Physics (ISSP) of the University of Tokyo in Chiba, Japan. The electromagnets in these laboratories share the same broad characteristics, and can be grouped into two categories: direct current (DC) magnets and

pulsed magnets.

Direct current magnets

In a DC magnet, a large electric current on the order of 10 kA is passed continuously through a conducting solenoid, thereby generating a steady, homogeneous magnetic field within the solenoid. DC field data presented in this thesis were collected in the NHMFL in Tallahassee and the HFML in Nijmegen.

The conducting solenoids that make up a DC magnet are made of either superconductors, normal conductors, or a combination thereof. As they are able to transport electric currents without dissipation, superconductors are ideal for use in DC magnets [55]. For instance, the Quantum Design Inc. PPMS and MPMS that are used extensively for low field characterization measurements consist of superconducting coils capable of generating magnetic fields of 7 T, 9 T, or 14 T, depending on the model. There are, however, a number of limitations on the strength of magnetic fields that can be practically generated using superconductors. The three main limitations are: the superconducting critical temperature T_c , the critical current density j_c , and the upper critical field H_{c2} of the superconductor used.

The superconducting transition temperature T_c presents an engineering challenge, where complex cryogenic cooling systems are required to keep the coils safely below their T_c . Sometimes the cooling systems can fail, causing a section of the coil to warm past its T_c and lose superconductivity. The sudden appearance of nonzero electrical resistance quickly generates large amounts of thermal energy, thereby causing a chain event that rapidly warms the entire coil above its T_c . These runaway events are known as “quenches”, which can sometimes lead to catastrophic failures of the coil. Despite the negative connotation of quenches, newly built superconducting magnets are often put through a series of controlled quenches to train the coils. Such exercises allow the magnets to run reliably at their highest rated current, thereby reducing the risk of unexpected quenches when they are deployed for use.

The critical current j_c of a superconductor presents an additional engineering challenge. Unlike T_c , which is an intrinsic property that varies between materials, j_c can often be

improved through metallurgical treatments. For instance, crystallographic defects can be intentionally introduced in type-II superconductors to act as pinning centers for flux vortices. Such treatments can often improve the critical current by a few orders of magnitude within the same material [56].

The upper critical field, on the other hand, has been the main factor limiting the strength of magnetic fields that can be generated by superconducting magnets. Presently, NbTi is the most commonly used compound for superconducting magnets with maximum fields below 9 T. Although NbTi by no means has the highest upper critical field among the available superconducting materials, it is relatively straightforward and cost-effective to manufacture due to its ductility. For fields of up to 22 T, the compound Nb₃Sn is often employed. Since Nb₃Sn is brittle and therefore expensive to manufacture, it is often used in conjunction with NbTi to reduce cost. More recently, the NHMFL in Tallahassee have successfully tested an all-superconducting magnet built in part with high- T_c cuprate superconductors. During its test run, the magnet reached a maximum field strength of 32 T, far exceeding the previous record of 23.5 T [57].

The second type of DC magnets are known as resistive magnets. As the name suggests, resistive magnets are fabricated from non-superconducting materials, typically copper or copper alloys. While resistive magnets are far less efficient than superconducting magnets to operate, they are used to generate much higher fields, the record of which is currently held by the NHMFL's new 41.4 T magnet. Although these magnets do not need cryogenic temperatures, they require a steady supply of cooling water – up to 15,000 litres per minute – to prevent heat generated by the large applied currents from damaging the coils. The need for a constant supply of ultra high current is also extremely energy intensive. The 41.4 T magnet in the NHMFL has a power consumption of 32 MW at maximum field, or roughly equivalent to the peak power output from the reactor in a typical nuclear-powered submarine [58].

A third type of DC magnets is known as hybrid magnets, which are made from a combination of superconducting and resistive coils. The most powerful DC magnet currently in use is the 45 T hybrid magnet in the NHMFL, which consists of a 33.5 T resistive insert

3. Experimental Methods

magnet and a 11.5 T superconducting outsert magnet. The resistive insert is water-cooled, while the NbTi and Nb₃Sn superconducting outsert is housed in a liquid helium cryostat pumped to 1.8 K. A cutaway drawing of the 45 T hybrid is shown in Fig. 3.5. In 2017, the NHMFL has broken their own world record of the strongest continuous magnetic field by reaching 45.5 T with a hybrid magnet made of a 31.1 T resistive outsert and a 14.4 T high- T_c cuprate superconducting insert [59]. While the magnet is still under development, the new record highlights the exciting possibility of using high temperature superconductors with high upper critical fields to generate DC fields above 45 T.

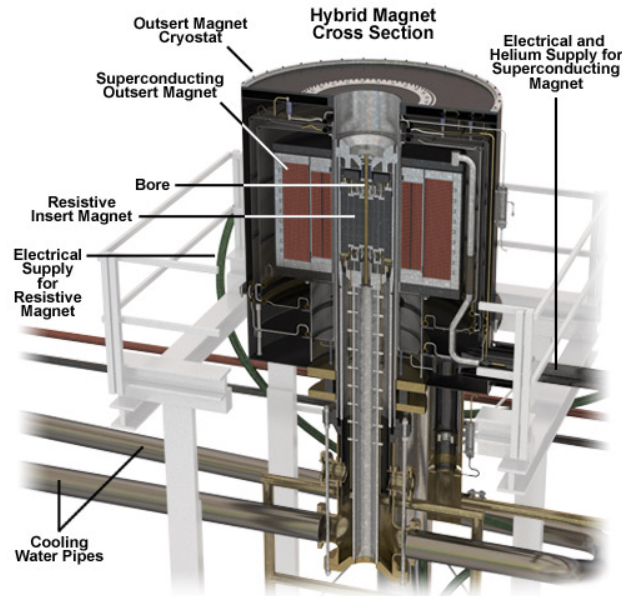


Fig. 3.5. The 45 T hybrid magnet. A cutaway drawing of the 45 T hybrid magnet in NHMFL in Tallahassee, Florida, courtesy of the laboratory’s website [60, 61].

Pulsed magnets

In order to produce even stronger magnetic fields, pulsed magnets sacrifice the persistent field offered by DC magnets for a short blast of very high fields. Pulsed field data presented in this thesis have been collected in HLD in Dresden and ISSP in Japan.

Similar to resistive DC magnets, pulsed magnets are made of copper or copper alloy solenoids. However, in contrast to the persistent current supplied to DC magnets, a short but intense pulse of current is discharged into these coils from capacitor banks, batteries, or motor generators. The magnets are immersed in liquid nitrogen baths to ensure that the coils are not melted by the immense heat generated during the discharge. The magnetic pulses have durations ranging from the order of ~ 10 ms to ~ 2 s, and the typical cooling time between successive pulses ranges from ~ 30 mins to ~ 4 hours. Fields of up to 60 T are routinely generated using magnets with a single coil, an example of which is shown in Fig. 3.6A. Single coil magnets that can reach up to 70 T are also available in several laboratories, including the 70 T magnet in HLD where data on the field-induced metallized phase of YbB_{12} presented in Chapter 4 of this thesis was collected. To reach even higher fields, double- and even triple-coil magnets have been developed. The most powerful non-destructive pulsed magnet in the world, operated by the NHMFL branch in Los Alamos, New Mexico, can generate a maximum field of 100 T [62].

In pulsed magnets, the main design limitation is the structural rigidity of the magnet during the pulse. The magnet experiences significant radial Lorentz forces during the current discharge as the rapid change in magnetic flux exerts an outward force on the coil, as well as shear and axial stresses on the structural reinforcement components [64]. Structural damages to either the coil or the reinforcement bracings can cause catastrophic failures of the magnet. While the NHMFL branch in Los Alamos has been generating fields of up to 100 T for user experiments since 2012, fields above 100 T can currently only be achieved through destructive means. For instance, single-turn coils, a one-turn winding of a thin copper plate, are regularly used to generate fields up to ≈ 300 T. Even higher magnetic fields up to thousands of T can be generated through the flux compression method. The method relies on compressing a metallic liner that has been subjected to some small seed magnetic field, where the rapidly shrinking liner with a fixed magnetic flux drives a brief but intense magnetic pulse [65]. Both the single turn coil and the flux compression methods produce pulse lengths on the order of a few μs , in which measurements can be made using optical techniques with fast enough response times.

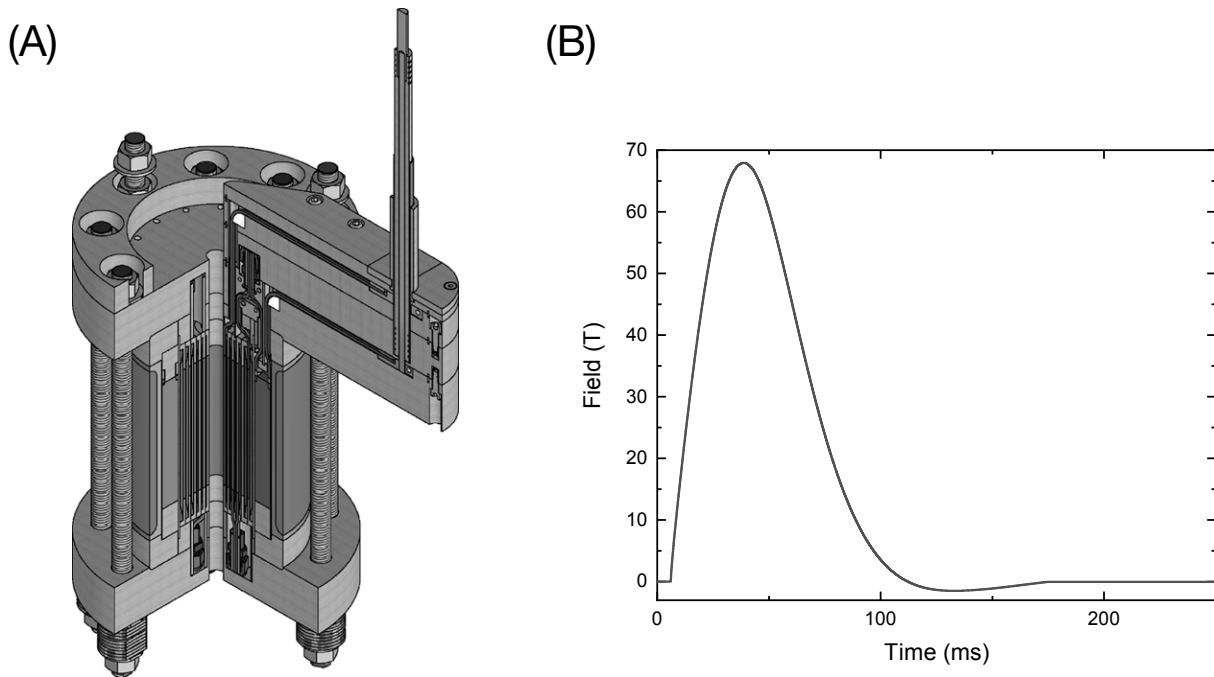


Fig. 3.6. Pulsed magnets. (A) A schematic drawing of the 65 T single coil pulsed magnet used in the Los Alamos National Laboratory [63], which has a similar design to the 70 T magnet in HLD. (B) The field profile of the 70 T magnet in HLD, where data on the field-induced metallized phase of YbB_{12} presented in Chapter 4 of this thesis was collected.

3.2.2 Torque Magnetometry

Cantilever torque magnetometry is a method of measuring changes in the anisotropic magnetization in a sample. For this technique, the sample of interest is placed at one end of a cantilever and subjected to an applied magnetic field. The deflection of the cantilever caused by the magnetic torque acting on the sample is measured using piezoelectric or capacitive means, which is used to infer the anisotropic magnetization of the sample [66–68]. Torque measurements presented in this thesis were performed using capacitive cantilevers, where the cantilever displacement is inferred by measuring the change in capacitance between the cantilever and a fixed Cu baseplate. A schematic drawing of the cantilever design is shown in Fig. 3.8A.

Physical background

The torque exerted by an applied magnetic field on a sample with magnetic moment \mathbf{m} is given by:

$$\begin{aligned}\boldsymbol{\tau} &= \mathbf{m} \times \mu_0 \mathbf{H} \\ &= \mu_0(m_b H_z - m_c H_y)\hat{x} + \mu_0(m_c H_x - m_a H_z)\hat{y} + \mu_0(m_a H_y - m_b H_x)\hat{z},\end{aligned}\quad (3.1)$$

where a , b , and c are the crystal principal axes and x , y , and z are the reference frame axes. We can define the reference frame axes to be the same as the crystal principal axes, as shown in Fig. 3.7.

The magnetic moment of a sample can be written as $\mathbf{m} = V\mathbf{M}$, where V is the sample volume and \mathbf{M} is the sample magnetization. Consider the case where the sample magnetization is linear in the applied field, $M_a = \chi_a H_a$, $M_b = \chi_b H_b$, and $M_c = \chi_c H_c$, which is applicable for magnetization quantum oscillations shown in this thesis. Substituting into Eq. 3.1, we find:

$$\boldsymbol{\tau} = \mu_0 V \left[H_b H_c (\chi_b - \chi_c) \hat{a} + H_a H_c (\chi_c - \chi_a) \hat{b} + H_a H_b (\chi_a - \chi_b) \hat{c} \right]. \quad (3.2)$$

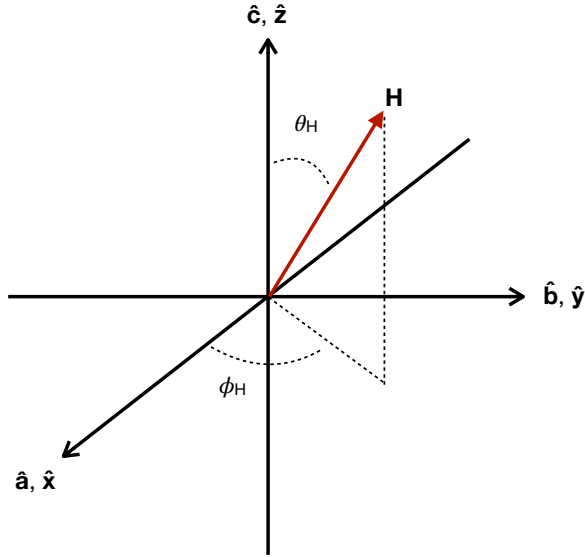


Fig. 3.7. Coordinate axes setup for torque magnetometry measurements. A schematic showing the axis orientations used in the magnetic torque derivation. The magnetic moment vector \mathbf{m} is omitted for clarity.

The torque experienced by a sample in an applied magnetic field is therefore a measure of the anisotropic magnetization of the sample. The amplitude of the magnetic torque on the sample can be written in terms of angles θ and ϕ as:

$$\tau = \mu_0 V H^2 \sin \theta \times \sqrt{\cos^2 \theta \sin^2 \phi (\chi_b - \chi_c)^2 + \cos^2 \theta \cos^2 \phi (\chi_c - \chi_a)^2 + \sin^2 \theta \sin^2 \phi \cos^2 \phi (\chi_a - \chi_b)^2}. \quad (3.3)$$

We therefore see that the magnetic torque background in the regime of linear sample magnetization scales quadratically with the applied magnetic field.

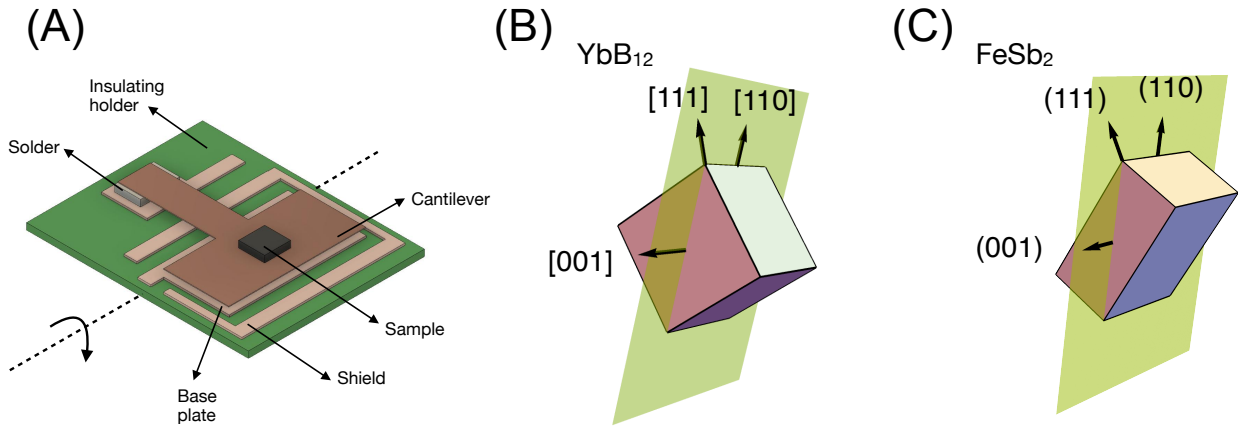


Fig. 3.8. Torque magnetometry rotation axis. (A) Schematic diagram of the cantilever setup. A sample is fixed on a BeCu cantilever, which is suspended over a Cu baseplate. A thin strip of grounded Cu shielding is placed around the cantilever baseplate to reduce noise. (B) Schematic diagram showing the measured rotation plane for YbB₁₂, where the sample is rotated through the [001]-[111]-[110] high symmetry directions. (C) Schematic diagram showing the measured rotation plane for FeSb₂, where the sample is rotated through the vectors normal to the (001), (111), and (110) planes [23].

Experimental setup

The experimental setup for capacitive torque magnetometry consists of a sample mounted on a thin sheet of nonmagnetic metal that hovers above a fixed nonmagnetic baseplate, thereby forming the two plates of a capacitor (Fig. 3.8A). In particular, our baseplates are made of Cu, and our cantilevers are laser cut from sheets of BeCu with thicknesses of either 20 μm or 50 μm . As thicker cantilevers have higher spring constants, we would ideally want to use thin cantilevers to maximize the sensitivity of our measurements. However, a thin cantilever could more easily be bent out of shape if the sample experiences a large magnetic torque. As the torque exerted on the sample is a function of sample volume, magnetization, and the size of quantum oscillations, there is often an element of trial and error for selecting the appropriate cantilever to balance between sensitivity and structural integrity.

To affix samples to the cantilevers, we use the EP30LTE-LO two-part epoxy from Master-

3. Experimental Methods

Bond. The epoxy was selected for its comparable thermal expansion coefficients to YbB_{12} [47] and FeSb_2 [16], which helps minimize strain induced by differential contraction upon cooling. To improve adhesion, the cantilevers are carefully roughened with coarse sand paper to increase contact area. Care must be taken during this process to avoid bending the cantilever, which can cause the cantilever to respond to applied torque in unexpected ways. Two small portions of epoxy are applied on two corners along the shortest side of a sample, which further minimizes strain induced by thermal contraction.

Since YbB_{12} samples are cut from floating zone boules with faces that are precisely aligned with crystallographic high symmetry directions, we simply need to make sure that the sample lies flat on the cantilever when mounted. The samples are typically cut with a surface aligned with the [001] high symmetry direction, and a perpendicular surface aligned with the [110] high symmetry direction. We therefore mount the sample with the [001] surface against the cantilever, and visually align the [110] surface against one of the sides of the cantilever. This allows us to access the [001]-[111]-[110] crystallographic plane during measurement using an in-situ rotation mechanism on the measurement probes. A schematic illustrating this rotation plane is shown in Fig. 3.8B.

The mounting process is more complicated for FeSb_2 , which has an orthorhombic unit cell and shows greater sensitivity to angles. As-grown FeSb_2 single crystals produced by the CVT method typically have a large flat surface that is aligned with the vector normal to (110) plane in k -space. This is orthogonal to the [001] axis, which is typically identified by a pyramid shape on grown samples. For ease of alignment, we initially chose to align samples in the rotation plane spanned by the above two directions – from the vector normal to (001), through the vector normal to (111), to the vector normal to (110). A schematic illustrating this rotation plane is shown in Fig. 3.8C.

To ensure precise alignment, FeSb_2 samples are mounted simultaneously as the two-part epoxy dries. The sample is first secured on the cantilever with a small amount of partially-dried epoxy, then visually aligned with the vector normal to (110). The sample is then placed in our X-ray Laue diffraction camera along with the cantilever, and checked for alignment with the [001] direction in the cantilever’s rotation plane. Fine adjustments are

then repeatedly made and checked with the Laue camera until a satisfactory alignment is achieved. After this, the epoxy is allowed to solidify, and the final alignment checked in case any movement occurred during the drying process.

To prevent samples from being lost in case the epoxy fails, two strips of thin teflon tape are placed on top of the secured sample in the shape of a cross. The teflon tape is secured onto the cantilever surface using the Loctite 4105 Instant Adhesive, and care is taken not to allow the adhesive to bind to the sample. Although the teflon tape precaution reduces the possibility of losing precious samples, the teflon and Loctite can sometimes bend the cantilever when the setup is cooled. Therefore, this step is sometimes omitted when the sample is large and the sample chamber is tightly enclosed.

Once the sample is mounted, the cantilever is soldered onto the magnetometer base with a 100 μm flat spacer, and the whole setup is secured onto the measurement probe. The cantilever, base plate, and grounded shield around the baseplate are connected to detection instruments using coaxial cables to shield external noise. The connected setup is first checked using an Andeen-Hagerling (AH) electronic capacitance bridge, which outputs a maximum of 15 V across the capacitance plates, and we typically choose a frequency of around 10 kHz. When the cantilever is mounted with a 100 μm spacer, the capacitance of the magnetometer should be 1.0 ± 0.1 pF. When the sample holder is rotated, the capacitance reading should vary depending on the direction of gravity, varying by up to approximately 0.1 pF between when the cantilever is being pulled towards the baseplate by gravity and when it is pulled away from the baseplate. It is also important to make sure the flexible coaxial cables do not tangle or stretch excessively during rotation, for fear of breakage during high field measurements.

During high field measurements, we have found that the General Radio (GR) 1616 analogue capacitance bridge offers higher precision than all electronic capacitance bridges tested. The GR bridge allows us to set a reference capacitance that balances the capacitance of the magnetometer, and outputs a proportionate voltage as the magnetometer capacitance changes. Initially during my PhD, we provided input voltage to the GR bridge using General Radio 1311-A audio oscillators, which output up to 100 V at frequencies on the order

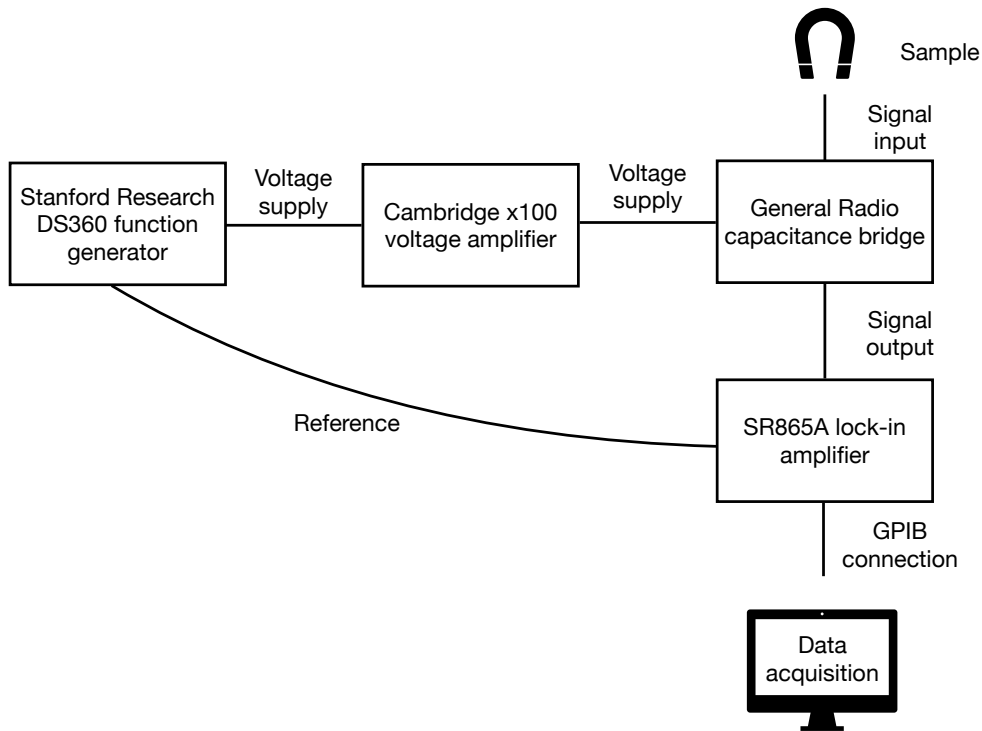


Fig. 3.9. Capacitive torque measurement setup. A schematic diagram showing the electronics setup for capacitive cantilever torque magnetometry measurements.

of kHz. Since these oscillators often drifted in measurement frequency and voltage, and did not provide the option of fine tuning the output frequency, they were later replaced by a combination of the Stanford Research Systems DS360 low distortion function generator with a $100\times$ gain high voltage amplifier developed by the Cavendish Laboratory electronics workshop. In addition to improved voltage and frequency stability, the DS360 allows us to tune the output frequency to avoid background noise peaks and harmonics from other measurement channels. The latter is typically done with the help of either a standalone spectrum analyzer, or the spectrum analysis function built into the Stanford Research Systems SR865A lock-in amplifier. The SR865A lock-in amplifier also allows us to fine tune the averaging and filtering of the voltage signal from the GR bridge, which leads to a marked improvement in noise performance. With the new measurement setup, we are able to achieve

a peak-to-peak noise of less than 10^{-7} pF in optimal conditions. The capacitance reading can be converted into units of torque through the following relationship:

$$\tau = Lk\delta = Lkd_0 \frac{\Delta C}{C_0}, \quad (3.4)$$

where L is the distance along the length of the cantilever between the anchored hinge and the sample, k is the cantilever spring constant, δ is the deflection of the cantilever, d_0 is the separation between the cantilever and the base plate, and ΔC is the change in capacitance, and C_0 is the capacitance without deflection. For typical values of $L = 3.8$ mm, $k = 28$ N/m, $d_0 = 0.1$ mm, and $C = 1$ pF, the optimal noise performance is approximately 10^{-12} N·m. A schematic for the electronics setup is shown in Fig. 3.9.

In addition to striving for an improved signal-to-noise ratio, it is important to make sure the measurement is operating in the expected regime. For torque magnetometry, two important considerations involve sample thermalization and sample magnetization. To provide the highest possible cooling power to the samples, all torque measurements had been performed in liquid ^3He . Before each magnet run, care is taken to allow for a sufficiently long condensation time, where the time varies between different cryostats and is advised by local user support personnel at each magnet lab. Despite the excellent cooling power provided by liquid helium, the sample could suffer from local heating due to field induced eddy currents. While eddy current heating is expected to be small in insulators, we still take care in checking that quantum oscillation amplitudes measured with different field sweep rates – which affects the induced currents – are comparable to within noise level.

As described earlier in this section, our torque magnetometry setup assumes the sample magnetization scales linearly with the applied magnetic field. To ensure this is the case, direct magnetization of the material is measured. While SQUID measurements are sufficient for low magnetic fields, extraction magnetometry is often employed for high fields. In YbB_{12} , a study of direct magnetization up to 70 T has been reported in Ref. [69]. As reproduced in Fig. 3.10A, the direct magnetization of YbB_{12} remains linear up to the anisotropic insulator-to-metal transition field. While an equivalent high field study could not be found for FeSb_2 , we have performed extraction magnetometry measurements up to an applied field of 60 T

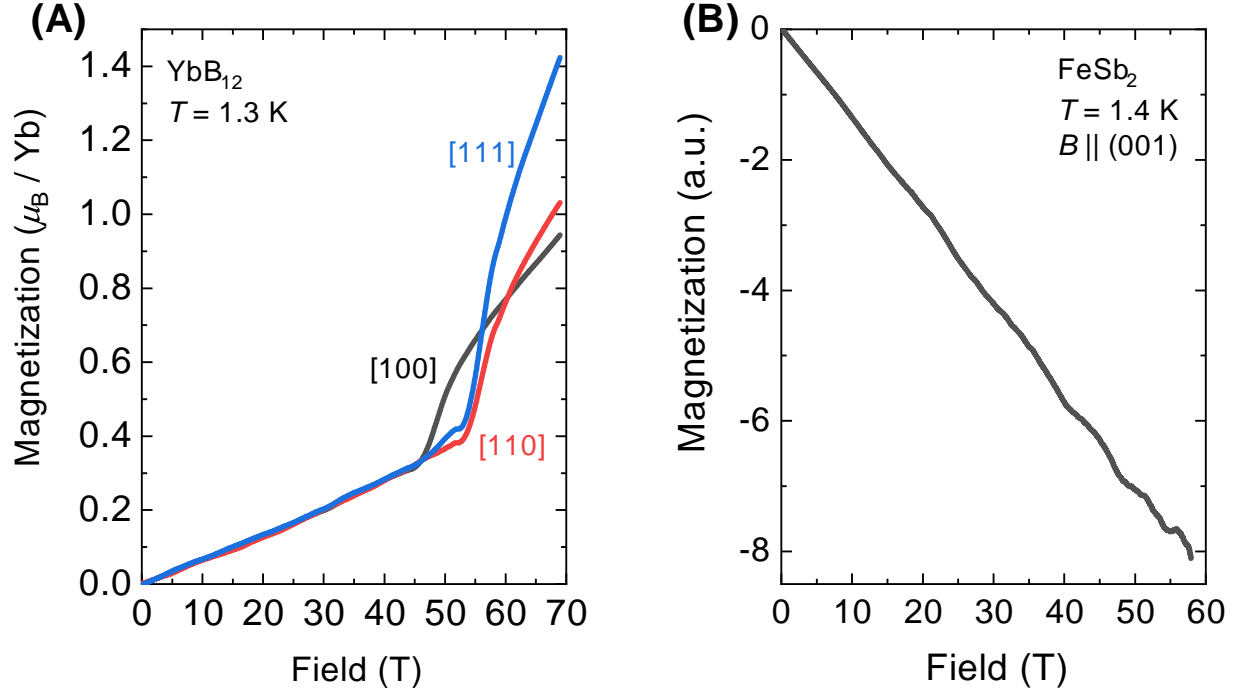


Fig. 3.10. Direct magnetization of YbB₁₂ and FeSb₂. (A) Magnetization of YbB₁₂ single crystals in applied magnetic fields up to 68 T aligned along three high symmetry directions [100], [110], and [111] reproduced from Ref. [69]. The measurement shows magnetization increasing linearly with applied magnetic field up to the insulator-to-metal transition field, suggesting our assumption that magnetization is in the linear regime for torque measurements is valid. (B) Magnetization measured on a collection of single crystals of FeSb₂ in applied magnetic fields up to 58 T along the [001] crystallographic direction. A collection of samples was used to maximize signal size. While the small diamagnetic signal from FeSb₂ complicated the calibration of the absolute signal size, the measurement shows direct magnetization scaling linearly with applied magnetic field up to at least 58 T. This validates our assumption that magnetization is in the linear regime for torque measurements for FeSb₂.

with collaborator Atsushi Miyake at ISSP in Japan. Although the small signal size in FeSb₂ has made it difficult to calibrate the absolute size of magnetization, our preliminary measurements show that the direct magnetization in FeSb₂ scales linearly with applied fields up to 60 T.

3.2.3 Electrical Transport

Wiring

Contacted electrical transport measurements were performed with the conventional four-probe method [70], a schematic of which is shown in Fig. 3.13. 25 μm diameter gold wires were attached either with DuPont 4929N air-cured silver epoxy or spot welded to the samples. The outer two wires supply current I_{applied} , which induces a voltage V_{measured} that is measured across the two inner wires. The resistance of the sample between the two inner wires can be calculated from Ohm's law:

$$R = \frac{V_{\text{measured}}}{I_{\text{applied}}}. \quad (3.5)$$

Although the four-probe method avoids the issue of contact resistances contributing to the measured voltage, resistance on all wire contacts still has to be minimized to avoid Ohmic heating and allow the use of high measurement frequencies. For a typical electropolished YbB_{12} single crystal, the resistance from a pair of contacts made with the 4929N silver paint at room temperature is on the order of 10 Ω . This can be reduced to less than 5 Ω by cleaning the sample surface with dilute nitric acid (HNO_3) immediately prior to attaching the gold wires with silver paint. A further improvement can be made by using the DuPont 6838N silver epoxy, which is cured at elevated temperatures of approximately 70°C. An alternative method of spot welding wires directly onto the sample, where the wire is welded by a sudden, large voltage discharge of around 7 V, can produce contact resistances of less than 1 Ω at room temperature. The improvement in contact resistance from acid cleaning and spot welding suggests the contact resistances are in part due to surface oxide layers. As such, further improvements could be possible through surface preparation techniques such as electron beam annealing [71, 72] followed by in-situ wiring in an inert atmosphere.

The contact resistances from the four procedures described above were tested across the temperature range between 1.8–300 K in a Quantum Design Inc. PPMS to select the most suitable method for high field measurements at low temperatures. These measurements were performed by attaching two additional current-supply wires directly onto the voltage probes

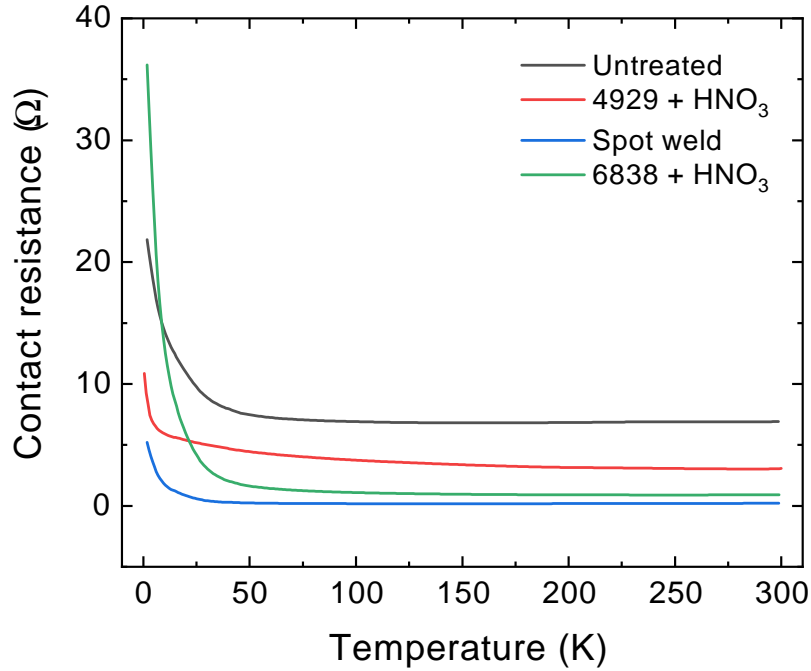


Fig. 3.11. Comparison of contact resistances for gold wires attached using various preparation methods. Contact resistance of 25 μm diameter gold wire attached using DuPont 4929N silver paint, DuPont 6838 silver epoxy, with nitric acid cleaning immediately prior to wiring, and with spot welding, as a function of temperature between 1.8–300 K. The measurements were performed using a Quantum Design Inc. PPMS using frequencies on the order of ≈ 20 Hz.

in the four-point configuration. Then, for each measurement, two voltage readings are taken at each temperature, one with the current wires on the sample, and one with the current wires on the voltage probes. This procedure allows the sample resistance to be subtracted accurately, leaving behind only the resistance due to the interface between the voltage probes and the sample. As the PPMS provides an exceptionally quiet measurement environment, frequencies on the order of a few tens of Hz were used for these measurements.

All four contacting techniques saw marked increases in contact resistance at low temper-

atures. This behavior is to be expected: as energy gaps open up in YbB_{12} and FeSb_2 at low temperatures, the interfaces between the gold wires and the sample effectively become metal-semiconductor junctions. While the behavior of this kind of interface is complex – with entire textbooks written on the subject [73] – the Ohmic nature of the contacts implies that contact resistances must be minimized to prevent Ohmic heating of the samples.

Surprisingly, at low temperature, the DuPont 6838N silver epoxy shows the highest contact resistance by a wide margin, despite its good performance at room temperature. The DuPont 4929N attached after dilute HNO_3 cleaning offers the best performance outside of spot welding. A plot of the contact resistances from the four wiring methods is shown in Fig. 3.11. The same test was conducted on FeSb_2 , with qualitatively comparable results but generally higher contact resistances at low temperature. Heeding to the lesson from this series of tests, spot welded contacts were made to all high field samples.

Experimental setup

The electrical transport measurement setup was different between DC and pulsed fields due to the drastically different measurement timescales. In DC fields, current was sourced from a Keithley 6221 AC/DC current source, which can supply arbitrary AC waveforms between 100 fA and 100 mA at frequencies between 1 mHz and 100 kHz. Frequencies of less than 100 Hz are typically used to minimize out-of-phase signal, which corresponds to capacitive and inductive components of the complex impedance. The precise frequency was chosen by looking for background noise troughs with the help of a spectrum analyzer. In order to maximize thermalization, the samples were mounted on polycrystalline quartz pieces and immersed in liquid ^3He for quantum oscillation measurements.

The amplitude of the electrical current was chosen to avoid Ohmic heating. To arrive at an appropriate current amplitude, successive field sweeps were performed at base temperature of the cryostat with progressively lower applied currents. The quantum oscillation amplitude was checked for each current amplitude; if the sample is affected by local Ohmic heating, the oscillation amplitude will scale inversely with the applied current. Fig. 3.12 shows changes in

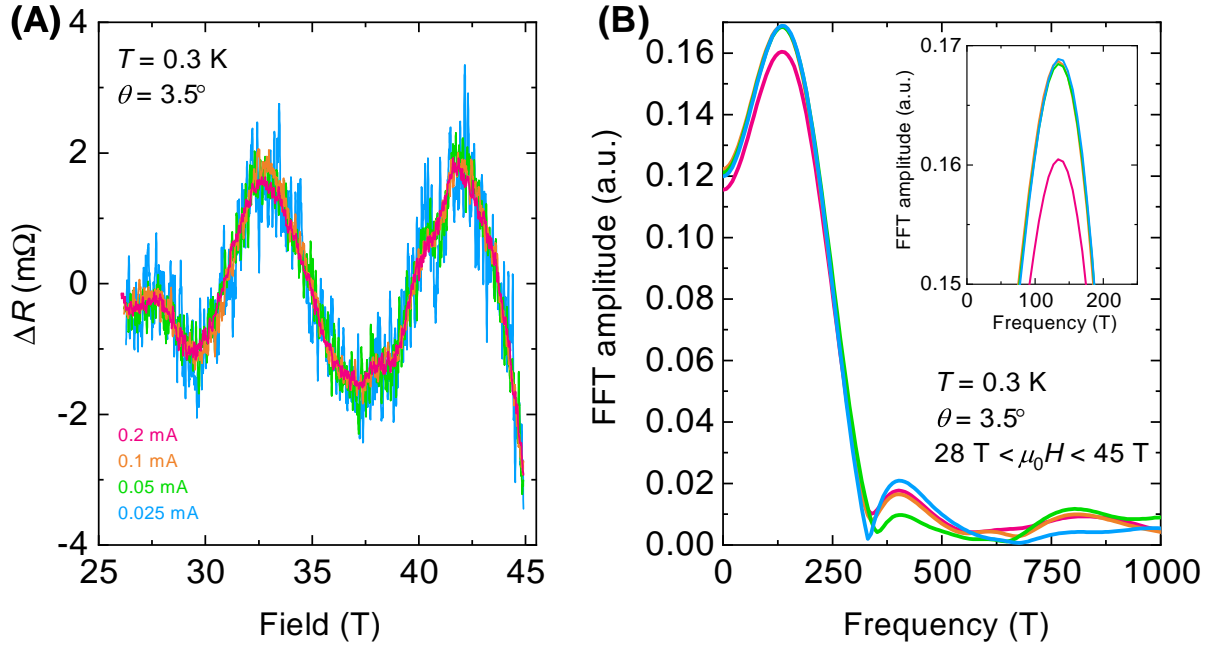


Fig. 3.12. Checking for local heating on electrical transport sample. (A) Quantum oscillations in the electrical resistivity of YbB_{12} measured with various applied currents at a temperature of 0.3 K and a magnetic field tilt angle of 3.5° from the [001] axis in the [001]-[111]-[110] rotation plane, after fifth-order polynomial background subtraction. An increase in oscillation amplitude can be seen with decreasing applied current, suggesting notable local Ohmic heating was present at high applied currents. **(B)** FFTs of the quantum oscillations shown in (A), showing an increase in oscillation amplitude with decreasing current, agreeing with visual inspection of the data in (A). The inset shows a zoom-in of the ≈ 150 T frequency peak, showing minimal change for the lowest applied currents.

quantum oscillation amplitude as a function of applied current during testing in the hybrid magnet. As both the subtracted oscillations and the FFTs show, a decrease in current from 0.2 mA to 0.1 mA produced a marked increase in the size of the dominant ≈ 150 T oscillations, while further decreasing the current to 0.05 mA and 0.025 mA produced minimal changes. Since the 0.025 mA signal showed significantly worse noise performance than the 0.05 mA signal, currents of 0.05 mA were used to measure quantum oscillations in the resistivity of YbB_{12} . This current yielded induced voltages on the order of 10's to 100's of

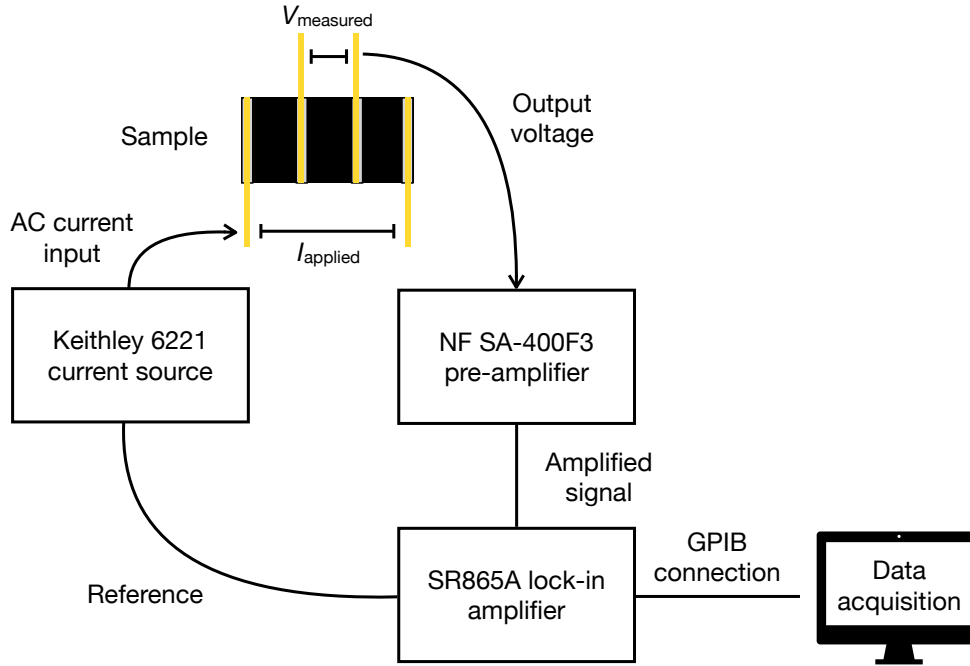


Fig. 3.13. Four-point contacted transport measurement setup. A schematic diagram showing the electronics setup for four-point transport measurements in DC magnetic fields.

μV at base temperature in the hybrid magnet, depending on the sample geometry and the exact base temperature reached. The measured voltage is amplified by a NF SA-400F3 low noise pre-amplifier before being measured by a Stanford Research Systems SR865A digital lock-in amplifier and recorded on a computer. The optimal signal-to-noise ratio in terms of quantum oscillation amplitude size for the dominant ≈ 150 T oscillation in YbB_{12} is typically on the order of $10\times$ to $100\times$. A schematic of this setup is shown in Fig. 3.13.

In pulsed fields, a National Instruments PXIe-6124 modular test system was used to simultaneously supply current and measure voltage. A voltage was generated by the PXI system across a shunt resistor on the order of $\text{k}\Omega$ placed in parallel with the sample, thereby generating a constant current through the sample. The current amplitude was chosen by applying successively lower current at zero field until the measured resistance reading stops

3. Experimental Methods

changing. A few current choices were then checked with field pulses to ensure a good signal-to-noise ratio. For resistance measurements performed on FeSb₂ at ISSP in Japan, a current of approximately 50 μ A was used at temperatures between 1.6 – 30 K to avoid heating effects, and a current of 1.2 mA was used above 30 K for improved signal size. At the switchover temperature, multiple field pulses were performed to check for overlap between the low and high current measurements. The large difference in the current used compensates for the two orders of magnitude decrease of resistance in FeSb₂ from 1.6 K to 30 K.

Pulsed magnets experience large vibrational noises when the current is discharged through the magnet coil, which affects the measurement noise behavior much more prominently than vibrations in DC magnets. In order to filter out low frequency vibrational noise from the magnet pulse, much higher measurement frequencies of 20 – 200 kHz was used for the applied current. The optimal frequency was chosen to produce a low background noise and a small, constant phase angle across all fields and temperatures. A drift in phase angle is particularly likely to occur in pulsed field measurements due to the high frequencies used. The phase angle needs to be kept as close to constant as possible to ensure the measured changes in voltage reflect changes in sample resistance rather than changes in the capacitive or inductive components of the complex impedance. This can be monitored by measuring the phase difference between the input current and voltage readout.

An additional consideration for resistivity measurements in pulsed fields relates to signal filtering. While filtering is usually performed by the SR865A lock-in amplifier for DC field measurements, we typically use tunable band pass filters in the Stanford Research Systems SR560 Voltage Pre-amplifier. An improvement in noise could be made by pairing the NF SA-400F3 low noise pre-amplifiers that we use in DC fields with fixed-frequency band pass filters custom made by colleague Alexander J. Hickey and the Cavendish Laboratory electronics workshop. While this setup yields multiple times better noise performance compared to the SR560, the fixed 100 \times gain on the NF SA-400F3 occasionally overloads the PXI system when measuring FeSb₂ at low temperatures due to high sample resistances.

Since the high measurement frequencies on the order of tens to hundreds of kHz exceeds the capabilities of traditional lock-in amplifiers, a digital method of locking in was required.

This was done using a program written by colleague Alexander J. Hickey, which produced a marked improvement in runtime efficiency and a more comprehensive range of tuning options than existing programs. When measuring the magnetoresistance of FeSb_2 in ISSP, we achieved a signal-to-noise ratio on the order of $100\times$, which, although could be improved further, was deemed sufficient for the purpose of extracting gap sizes as a function of applied field.

3.2.4 Proximity Detector Oscillator

The proximity detector oscillator (PDO) is a radio frequency contactless resistivity measurement [74]. It is a variation of the tunnel diode oscillator (TDO) setup developed for improved robustness in pulsed field environments [75]. Unlike four-point contacted resistivity, contactless techniques are sensitive to material skin depth, which is determined by a combination of resistivity and susceptibility. Although directly interpreting the radio frequency oscillator signal is often complicated [76, 77], the fast response times and the ability to operate in frequency ranges well above vibrational noises make these techniques exceptionally useful in pulsed field measurements.

Both TDO and PDO have been extensively used for measuring quantum oscillations in high magnetic fields, which are often required to access the normal state of superconductors and other high field material phases. One question that naturally arises regarding oscillator techniques pertains to how well they reproduce the results of conventional measurement techniques such as contacted resistivity and torque. As a study of the organic superconductor $\kappa\text{-(ET)}_2\text{Cu(NCS)}_2$ shows, quantum oscillation frequencies measured by TDO [78] shows good agreement with SdH [79] and dHvA [80] frequencies measured by other techniques. A more recent study using PDO on the $\text{YBa}_2\text{Cu}_3\text{O}_{6.51}$ high temperature superconductor also shows good agreement [81]. We can therefore be confident that these oscillator techniques are capable of sensing material properties in a comparable manner to contacted electrical transport and magnetic torque.

To understand how the PDO circuit sustains resonant oscillations and responds to changes

3. Experimental Methods

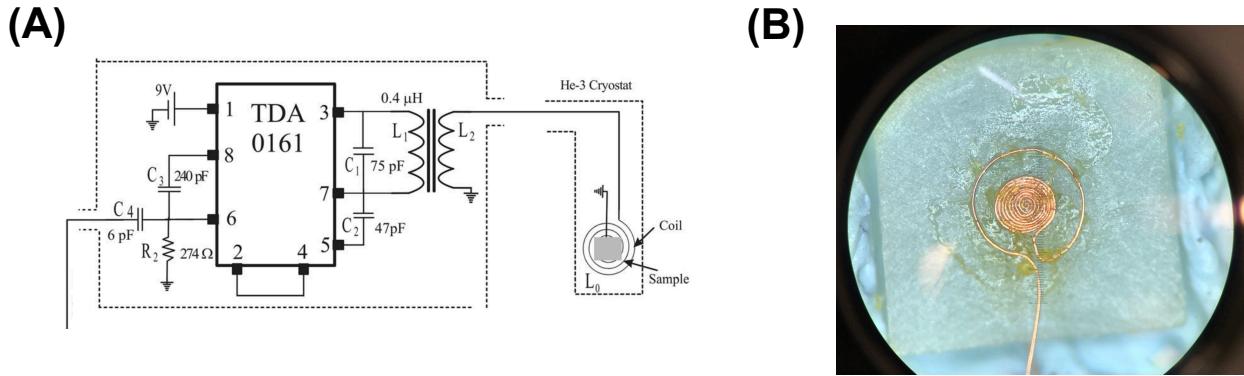


Fig. 3.14. Proximity diode oscillator setup. (A) Schematic diagram of the circuitry around the TDA0161 integrated circuit chip. Image reproduced from Ref. [74]. (B) Picture of a hand-made sample coil used in the PDO circuit. The sample is secured on top of the coil with GE varnish, which provides adhesion and thermalization.

in sample properties, we examine the circuit design following Ref. [74]. The PDO consists of a resonant LC tank circuit with a component that compensates for losses. Our PDO circuit follows that described in Ref. [74], which uses a TDA0161 integrated circuit chip from STMicroelectronics, typically used in metal detectors, as the self-compensating element. The chip exhibits negative effective differential resistance between pins 3 and 7 in Fig. 3.14A. The negative differential resistance stabilizes changes to the oscillating LC signal to maintain a stable amplitude. The sample of interest can be placed in either the inductor or the capacitor in the LC circuit, and the change in the resonant frequency $f = \pi/2\sqrt{LC}$, where L is the inductance and C is the capacitance of the circuit, is measured to infer changes in sample properties.

PDO data presented in this thesis were collected with the circuit in inductor mode, where the sample was placed on an inductor coil. In this mode, the resonant frequency of the PDO circuit reflects changes in coil inductance caused by changes in the sample skin depth:

$$\frac{\Delta f}{f_0} = -\frac{\Delta L}{2L}, \quad (3.6)$$

where f_0 and L are the initial frequency and inductance of the circuit, respectively. The

effective inductance of the PDO circuit is determined by a number of circuit parameters:

$$L_{\text{eff}} = L_1 \left[1 - \frac{M^2}{L_1(L_2 + L_0 + L_{\text{coax}})} \right], \quad (3.7)$$

where L_0 , L_1 , and L_2 are circuit components shown in Fig. 3.14A.

Experimental setup

The pulsed field quantum oscillation data on YbB_{12} presented in this thesis were collected using PDO circuits made by the Cavendish Laboratory electronics workshop following Fig. 3.14A [74]. The inductor L_0 was hand-made by myself using 25 μm diameter insulated copper wires. The number of turns in the inductor was varied according to the sample size; the coil should be as large as possible, but without becoming exposed from underneath the sample. This usually came to between 5 – 15 turns. As can be seen in Fig. 3.14B, a counter-turn was added to the outside of the completed coil. The counter turn was made to have approximately the same surface area as the sum of the combined surface areas of the inner turns, which helps minimize induced voltages caused by the magnet pulse.

During experiments, pins 2 and 4 on the TDA0161 IC chip are shorted together so that the PDO circuit oscillates without a sample coil connected. Usually, losses arising from the sample coil and the coaxial cables on the measurement probe would lead to a lower signal amplitude and prevent the PDO circuit from oscillating at room temperature altogether. During the course of my PhD, we have found that the ultra-low attenuation provided by the model SC-086/50-SB-B semi-rigid coaxial cables from Coax Japan Co. circumvents this issue. A loaded PDO circuit that oscillates at room temperature was useful, for it allowed us to troubleshoot background noise without cooling the sample. This became particularly important in HLD, where it was necessary to diagnose whether the magnet itself was a source of RF noise. Construction of measurement probes that incorporated the new semi-rigid coaxial cables and noise troubleshooting in HLD were performed in collaboration with colleague Alexander J. Hickey.

3. Experimental Methods

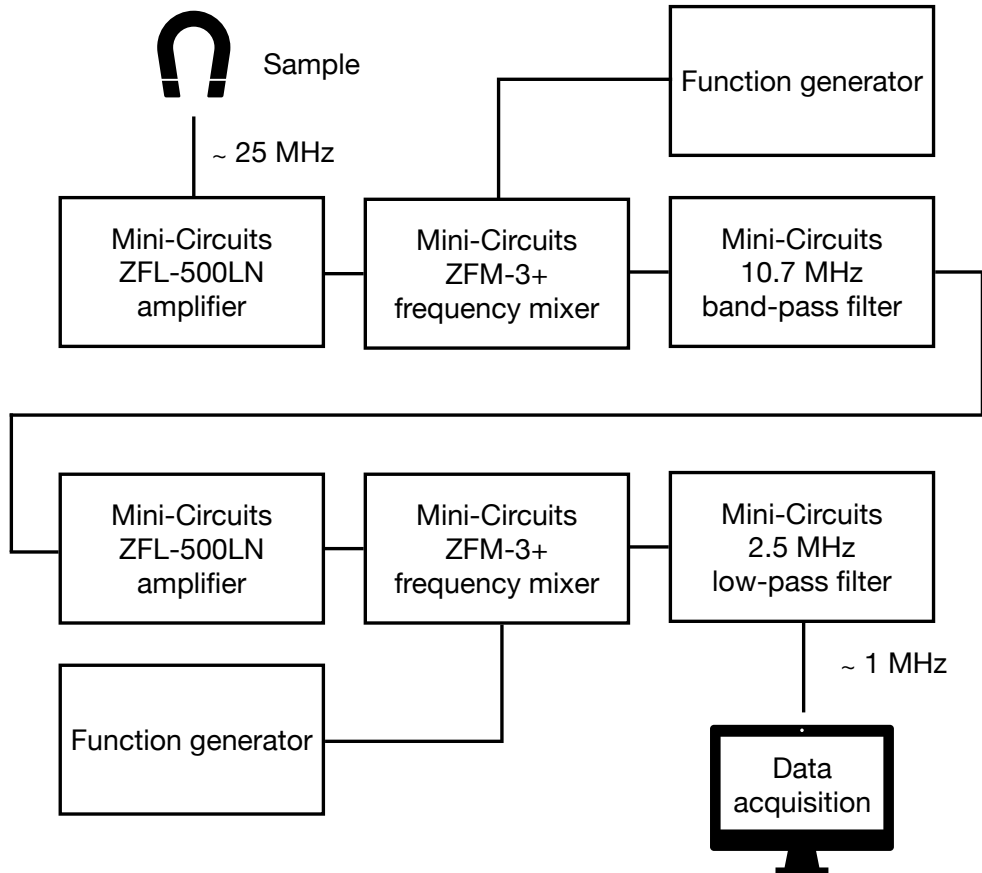


Fig. 3.15. Proximity detector oscillator measurement setup. A schematic diagram showing the signal processing circuit for bringing down the raw PDO resonant frequency to a frequency that can be digitized and processed by a computer. Either one or two stages of amplification, mixing, and filtering was performed depending on which produced lower noise and better stability. Regardless of how many stages of mixing was performed, the final output frequency was always tuned to ~ 1 MHz for digitization and acquisition.

To tune the coupling between the sample and the PDO circuit, the number of turns in inductor L_2 was adjusted. As this affected both the amplitude and resonant frequency of the circuit, capacitor C_2 was changed to maintain a resonant frequency between approximately 25 – 40 MHz. The oscillating signal was first amplified before being passed through a frequency

mixer to bring the output frequency to an appropriate value for band pass filtering. Either one or two stages of mixing and filtering was performed, depending on which produced lower noise and better signal stability. The final output frequency was tuned to ≈ 1 MHz and digitized by a PXI system acquiring at 15 MHz sampling rate. The digitized data was then converted into frequency reading with a sliding discrete FFT program written by colleague Alexander J. Hickey. Under ideal conditions, we achieved an in-field peak-to-peak noise of 40 Hz in PDO resonant frequency with 80 μ s averaging and 40 μ s sliding windows in the 70 T pulsed magnet in HLD. A block diagram for the PDO signal processing circuit is shown in Fig. 3.15.

Due to the large and rapidly changing magnetic induction during a pulsed field measurements, eddy current heating was an important consideration for quantum oscillation measurements in the metallic phase of YbB_{12} . For this reason, the HLD 70 T long pulse magnet was particularly suited for the task of measuring quantum oscillations on heavy fermion materials, since its pulse length of over 100 ms is up to an order of magnitude longer than other magnets that reach comparable fields. To provide maximum cooling power, the samples were immersed in liquid ^3He in a custom cryostat built by HLD. Thermalization of measurement wires along the probe was also important in minimizing heat from being transported down the cryostat.

Care was taken to ensure that good overlap is achieved between the rising-field and falling-field portions of each pulse. Particular attention was paid to ensure that the signal overlaps at 0 T immediately before and after the pulse, that the insulator-to-metal transition field agrees for the rising- and falling-field portions, and that the quantum oscillation sizes are comparable (See Fig. 3.16). While every effort was made to reduce heating, it was inevitable that some amount of heating takes place. As shown in Fig. 3.16B, the quantum oscillation amplitude was noticeably smaller on the falling-field portion of the sweep; comparing the last oscillation period, the oscillation amplitude decreases by $\approx 25\%$ for the falling-field portion of the sweep. We therefore use the quantum oscillation amplitude from the increasing-field portion of the sweeps in the Lifshitz-Kosevich amplitude analysis to further minimize the effect of heating.

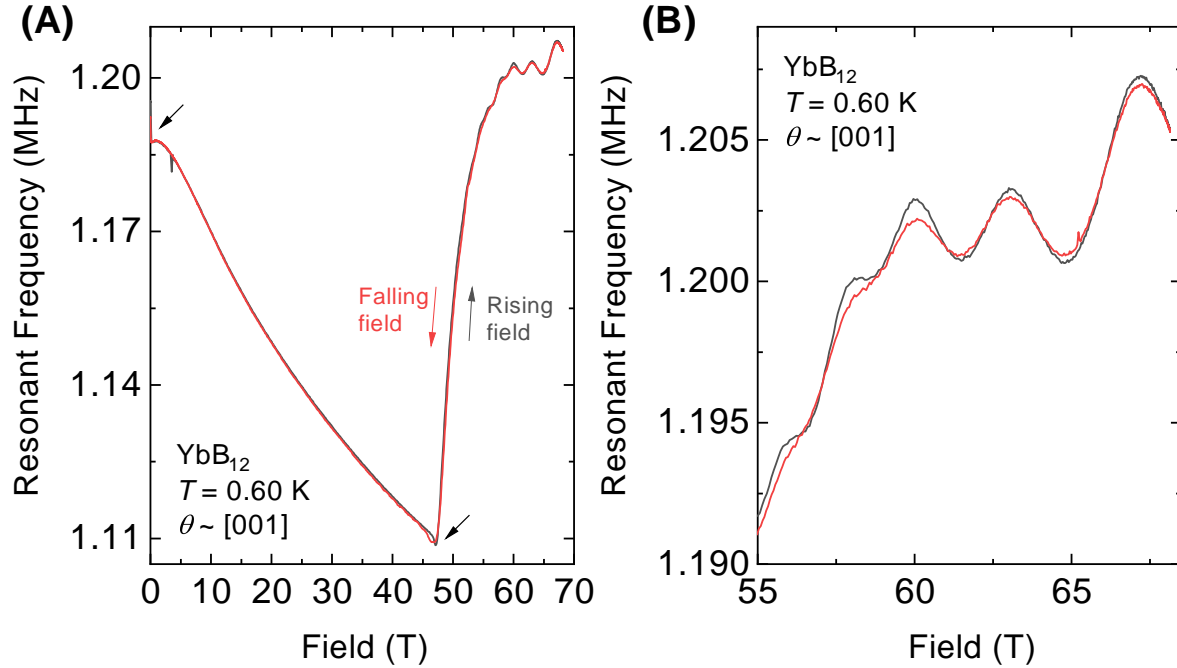


Fig. 3.16. Checking for local heating on PDO sample. (A) PDO resonant frequency for a YbB_{12} sample as a function of applied magnetic field for rising (black) and falling (red) portions of the pulse. The overall form of the background shows good overlap between the rising and falling portions of the pulse, with the zero field frequency and insulator-to-metal transition field (marked by arrows) agreeing well. (B) The highest field portion of the PDO resonant frequency shown in (A), where prominent quantum oscillations are visible. While the location of the peaks and troughs agree well between the rising and falling portions of the pulse, the oscillation amplitude is seen to decrease during the falling portion of the pulse. This suggests that local heating has occurred during the pulse.

3.3 Quantum oscillation background subtraction

As discussed in Chapter 2, quantum oscillations appear as undulations in physical properties such as magnetization and electrical resistivity. While effort is made to select high quality samples that show large quantum oscillations compared to the background signal, background subtraction methods are important in cases where the size of the oscillation is

small compared to the background. This was particularly relevant for YbB_{12} and FeSb_2 , both of which exhibit large background signals.

Two background subtraction techniques were used for the analysis of quantum oscillations in YbB_{12} and FeSb_2 : polynomial fitting and local regression. We typically use polynomial subtraction, where a global least squares fit to the measured torque, resistivity, or PDO resonant frequency background is performed using a n^{th} order polynomial. This technique has the advantages of being simple and produces a smooth background. However, polynomial subtraction could introduce notable spurious signal if the polynomial order is mismatched. Fig. 3.17 illustrates this problem through an overlay of a fourth order “fit” polynomial to a fifth order “data” polynomial, along with their difference. As we can see in the figure, zeroes in the residual correspond to points at which the fit crosses the data, and large spurious peaks appear in the residual between such crossings. In general, an n^{th} order fit can introduce up to n spurious peaks in the subtraction. In order to circumvent this problem, multiple fits using different polynomial orders are typically performed to check that features in the subtracted data appear at consistent locations. Where possible, we also compare the subtractions to derivatives of the raw background, which introduce a phase difference but maintains the oscillation frequencies.

Recently, we have adopted a local regression technique known as LOESS in collaboration with colleagues Máté Hartstein, Alexander J. Hickey, and Prof. G. G. Lonzarich. Whereas the polynomial fit technique performs a global regression across the whole data range, LOESS performs a weighted, local low-order polynomial fit at each point in the data range [82]. A regression function value is then computed for each local fit, and the results across the full data range are aggregated to produce a fit to the measured data. In other words, LOESS fits a second or third order polynomial (which the user chooses) to a few Teslas of data (again a choice of the user), where data points closer to the point of interest is weighted more heavily than data points further away. This low order polynomial is evaluated at the point of interest, yielding a value for the background fit. This process is repeated across the full range of the data set, and the results from each local fit are aggregated to form the background.

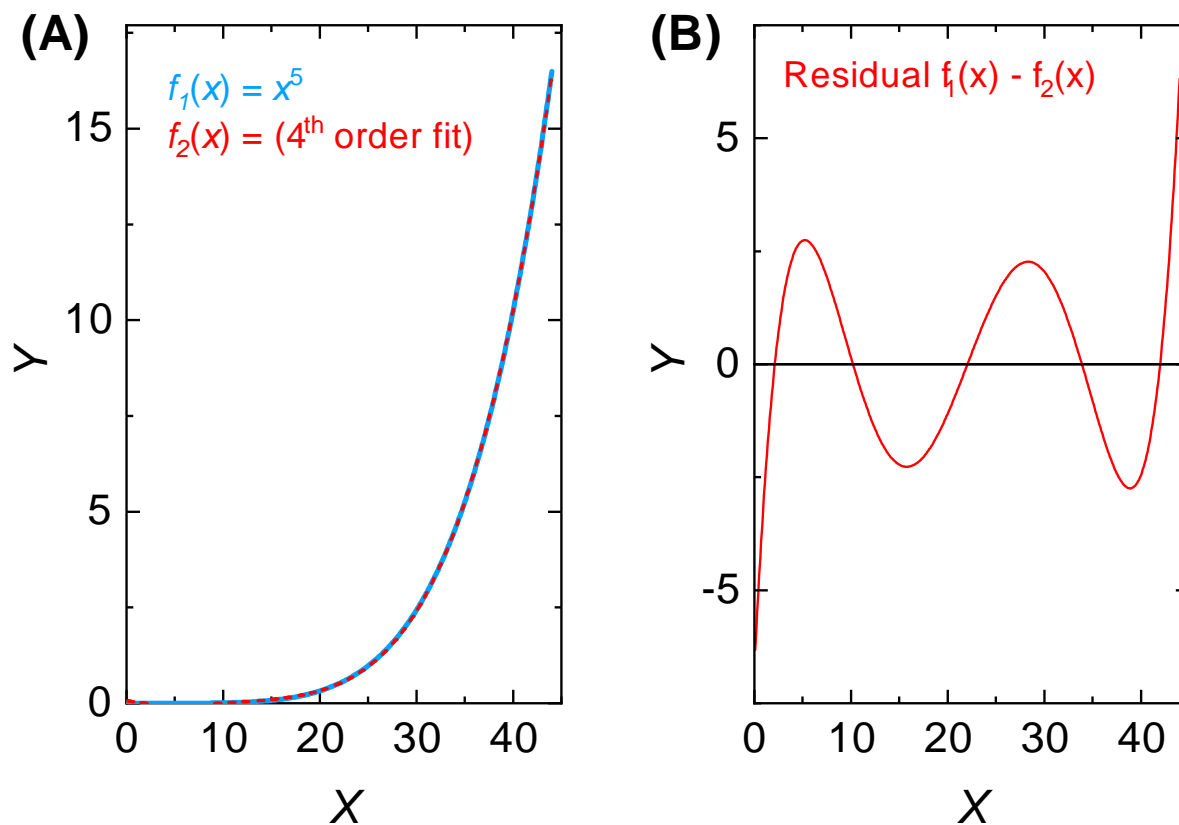


Fig. 3.17. Potential errors from polynomial background subtraction. (A) Fitting a fifth-order polynomial (blue solid line) with a fourth-order polynomial (red dashed line). Good qualitative agreement is seen between the background and the fit. (B) The residual after subtracting the fourth-order polynomial fit from the fifth-order polynomial background shown in (A). Despite the good agreement between the background and the fit seen in (A), four spurious peaks and large tails at the extremities are introduced in the residual.

The LOESS technique has several advantages over conventional polynomial background fits. As we saw in Fig. 3.17B, fitting a single function across an entire dataset often leads to large residuals at the extremities. By performing local fits and evaluating the fits at their midpoints, LOESS avoids such residual tails. Since LOESS does not require a global background function to be specified, it is also able to handle unusual background shapes more

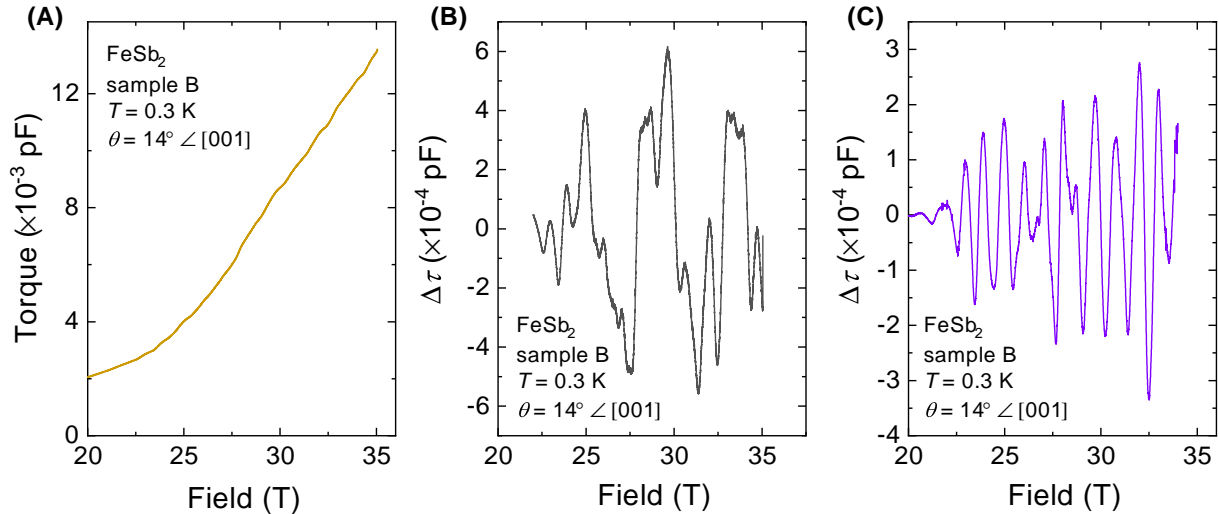


Fig. 3.18. Comparison of LOESS with global regression background subtraction. (A) Magnetic torque background on which subtraction methods will be compared, showing a change in background slope just below 25 T and quantum oscillations that are small but visible on top of the large torque background. (B) Quantum oscillations extracted using a fifth order polynomial background subtraction. Oscillations can be seen on top of five broad peaks introduced by the polynomial background subtraction. (C) Quantum oscillations extracted using LOESS background subtraction. This method avoids large spurious features that are not visible in the raw torque background shown in (A).

flexibly compared to global fits. For instance, LOESS can subtract backgrounds across features such as changes in the background slope. As the background is produced by averaging out signal and noise, the technique is particularly effective when the signal size is small compared to the background size. Fig. 3.18 compares background subtractions performed with a fifth-order polynomial and with LOESS, highlighting the tendency for global regression to introduce large spurious peaks when quantum oscillations are small as a fraction of the background size.

Despite its many advantages over conventional polynomial background subtraction, LOESS has a number of drawbacks. Since LOESS fits to local subsets of the data, the results can be skewed by features in the data if the chosen fit window is too narrow. For instance,

3. Experimental Methods

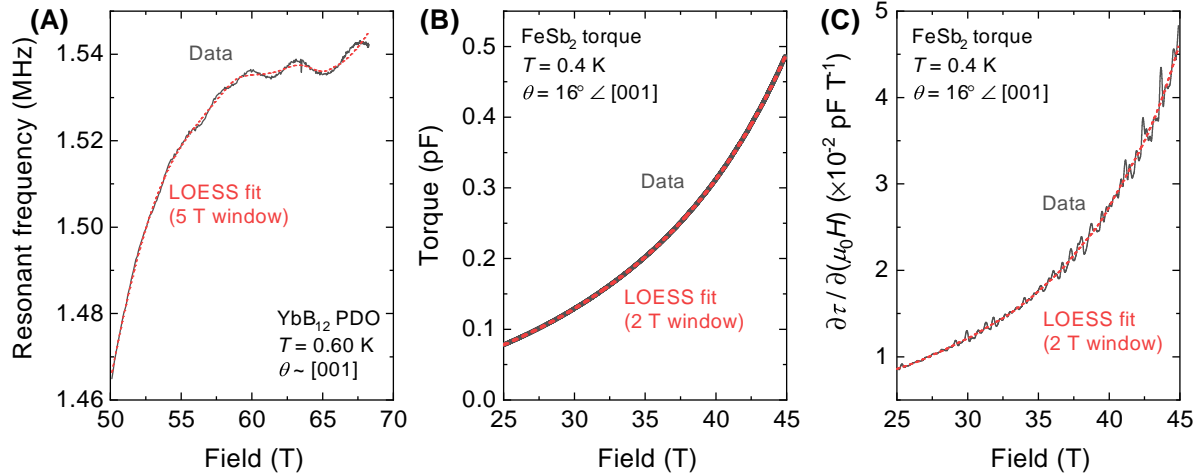


Fig. 3.19. Potential errors from LOESS background subtraction. (A) Fitting to the background signal of YbB_{12} measured with PDO (solid black line) using the LOESS algorithm with a 5 T window for local regression (dashed red line). As the fit shows, the LOESS algorithm is not suited for background fits when a large local regression window compared to the quantum oscillation period cannot be used. Even a relatively large window of 5 T produces a background that is influenced by the oscillations. (B) Fitting to the torque background of FeSb_2 (solid black line) using the LOESS algorithm with a 2 T window for local regression (dashed red line). Good agreement is seen across the full field range examined. (C) First-order derivative of the torque background shown in (B) (solid black line) overlaid with a first-order derivative of the LOESS fit (red dashed line). Good agreement is seen between the derivatives of the data and the fit, suggesting that spurious features have not been introduced as a result of the background subtraction.

the technique performs poorly on large amplitude quantum oscillations whose periods are comparable to or larger than the desired fit window, such as those observed in the metallic phase of YbB_{12} (Fig. 3.19A). In these scenarios, the LOESS algorithm has to perform local fits across a much wider field range compared to the quantum oscillation period in order to smooth out the oscillations and extract the background. Such a restriction limits the use of LOESS when only a few periods of oscillations could be observed in the available field range for a particular experiment. This problem is usually not difficult to overcome, since polynomial subtractions typically perform well when the quantum oscillation amplitude is

large compared to the background. If polynomial subtraction is undesirable, an iterative approach could also be adopted, where consecutive subtractions are performed until the local regression converges.

Since LOESS does not follow a predefined functional form across the whole data range, another drawback is that the technique could produce unusual backgrounds, and therefore spurious features in the subtraction. In order to account for this potential problem, care must be taken to ensure that the background produced by LOESS agrees with the data. This can be done by looking at derivatives of the fit. While the first and second derivatives do not necessarily have to be constant – changes to the derivatives are to be expected if we fit across a change in background slope or other features – the derivatives must be free of features that are not visible in the raw data. Fig. 3.19B and C show an example of a desirable LOESS background fit and a derivative check for the fit.

3.4 Numerical simulations of quantum oscillations

For measured quantum oscillations that exhibit complex waveforms consisting multiple frequencies with comparable amplitudes, conventional methods of establishing the periodicity of the oscillations in inverse magnetic field, such as Landau level index plots, cannot be used. For instance, quantum oscillations observed in the field-induced metallic phase of YbB_{12} presented in Chapter 4 are comprised of four dominant frequencies with similar amplitudes. The peaks that are visible in such raw spectra are often the product of the convolution of multiple frequencies, rather than peaks associated with any individual frequency component. In order to determine the periodicity of the oscillations in such cases, we computationally simulate the measured oscillations with the Lifshitz-Kosevich formula.

Simulations of measured quantum oscillation data are routinely performed with gradient descent optimization functions to fit the Lifshitz-Kosevich formula with multiple frequency components to the experimental data. Since the quantum oscillations in the metallic phase of YbB_{12} consists of at least six frequencies, it was found that gradient descent is easily trapped by local minima and is unable to produce satisfactory simulations. To overcome this problem,

3. Experimental Methods

we have developed a new simulation algorithm using the Particle Swarm function, which is part of the Global Optimization Toolbox in Matlab.

Particle Swarm is an iterative, global optimization function that is modeled on the behavior of bird flocks and fish schools [83, 84]. The algorithm randomly initializes a set of candidate solutions, referred to as particles, and iteratively moves the particles in parameter space according to their assigned velocities. During each iteration, the particle velocities are updated to nudge them towards the locally best known solution as well as the globally best known solution.

One advantage of the Particle Swarm algorithm over conventional optimization methods such as gradient descent is that the algorithm can search large parameter spaces with large numbers of local minima. The element of randomness in Particle Swarm, as well as the fact that the particles are influenced by the globally best known solution, make the algorithm less likely to be trapped in local minima. This feature of Particle Swarm is particularly relevant for fitting complex quantum oscillation data, as each frequency can have up to five independent parameters (this will be discussed below).

One drawback of Particle Swarm is that the algorithm does not guarantee the optimal solution, or even a satisfactory solution, will be found. This is potentially problematic since our aim is to show evidence that experimentally measured quantum oscillations are physically real, rather than artifacts of the experimental or the data analysis procedures. In this regard, such fits to measured quantum oscillations should be regarded as simulations – they suggest whether the observed oscillations could be reproduced with reasonable parameters. On its own, the success of a simulation in replicating the observed oscillations does not guarantee the experimentally observed quantum oscillations are real. It should be regarded as one piece of evidence among many, for instance reproducibility across samples, agreement to the LK temperature analysis, among others, in suggesting that experimentally observed quantum oscillations are physically real. On the other hand, failure to simulate the observed oscillations, particularly a failure to reproduce the locations of observed peaks, would suggest that the observed oscillations may be spurious.

With the advantages and limitations of the Particle Swarm algorithm in mind, we pro-

ceed to discuss how the algorithm is used to simulate experimentally observed quantum oscillations. As discussed in Chapter 2, magnetization quantum oscillations is described by the Lifshitz-Kosevich formula [13, 44]:

$$\widetilde{M} = A \cdot R_T \cdot R_D \cdot B^{1/2} \cdot \sin\left(\frac{2\pi F}{B} + \phi\right), \quad (3.8)$$

where A is some prefactor, F is the quantum oscillation frequency, B is the applied magnetic field, and ϕ is some phase factor. $R_T = X/\sinh X$ is the temperature damping term, in which the coefficient $X = 2\pi^2 k_B T m^*/e\hbar B$ can be simplified to $X \approx 14.7 \cdot T m^*/B$, where m^* is the quasiparticle effective mass in units of bare electron mass (m_e) and T is the measurement temperature. $R_D = \exp(-B_D/B)$ is the Dingle damping term, where B_D is the Dingle coefficient in units of Teslas. Since magnetic torque is given by $\boldsymbol{\tau} = \mathbf{m} \times \mathbf{B}$, an additional factor of B is introduced to Equation 3.8 for dHvA oscillations measured with torque magnetometry.

To numerically simulate the observed quantum oscillations, Equation 3.8 was supplied to the Particle Swarm function with A , B_D , F , and ϕ as free parameters for each frequency. F was allowed to vary within a small range from the frequencies indicated by FFT peaks of the measured data to account for uncertainties in the FFTs. The effective masses (m^*) obtained from LK temperature dependence fits for each measured quantum oscillation frequency was used. In general, the effective mass can also be left as a free parameter when a LK temperature dependent analysis is not available. The algorithm then minimizes a difference function that takes into account Equation 3.8 and the measured data. Since a simple difference between the two would heavily bias the high field region where quantum oscillation amplitudes are largest, a term inverse to R_D is introduced to the difference function to balance the weighting across the full measurement field range.

To validate the Particle Swarm algorithm's ability to reproduce published fits, we apply the algorithm to quantum oscillations measured on the high temperature cuprate superconductor $\text{YBa}_2\text{Cu}_3\text{O}_{6.56}$. We use the data presented in Fig. 4 in Ref. [85], where fits have been performed using a two-frequency neck and belly Fermi surface model. To simplify the procedure, we consider only the sweep taken at $\theta = 0^\circ$. In addition to the damp-

3. Experimental Methods

ing factors shown in Eq. 3.8, an additional field-dependent damping factor is introduced: $R_w = J_0[2\pi\Delta F_{\text{neck - belly}}/B \cos\theta J_0(k_F c \tan\theta)]$. Here, J_0 is the Bessel function of the first kind, and $\Delta F_{\text{neck - belly}}$ is the Fermi surface corrugation frequency. Since we only consider the $\theta = 0$ sweep, the damping term simplifies to $R_w = J_0[2\pi\Delta F_{\text{neck - belly}}/B]$. Simulations were performed either using the published values for $\Delta F_{\text{neck - belly}}$, or with the values left as free parameters, yielding qualitatively comparable results.

As shown in Fig. 3.20A, the Particle Swarm algorithm is able to reproduce the published quantum oscillations in $\text{YBa}_2\text{Cu}_3\text{O}_{6.56}$ with high accuracy, yielding comparable fits to those shown in Ref. [85]. Crucially, the algorithm yields quantum oscillation frequencies that are within approximately 1% of the published values, as well as Dingle damping factors that are within approximately 10% of the published values. It should be noted, however, that comparably high quality simulations can be produced with parameters that differ from the published results by more than a factor of two. Fig. 3.20B shows three qualitatively comparable simulations produced using various parameters. The variation in simulation parameters speaks to the difficulty in pinpointing a simulation that reflects physical reality, and serves as a reminder that these simulations should only be one of many pieces of evidence to suggest the observed quantum oscillations are physically real.

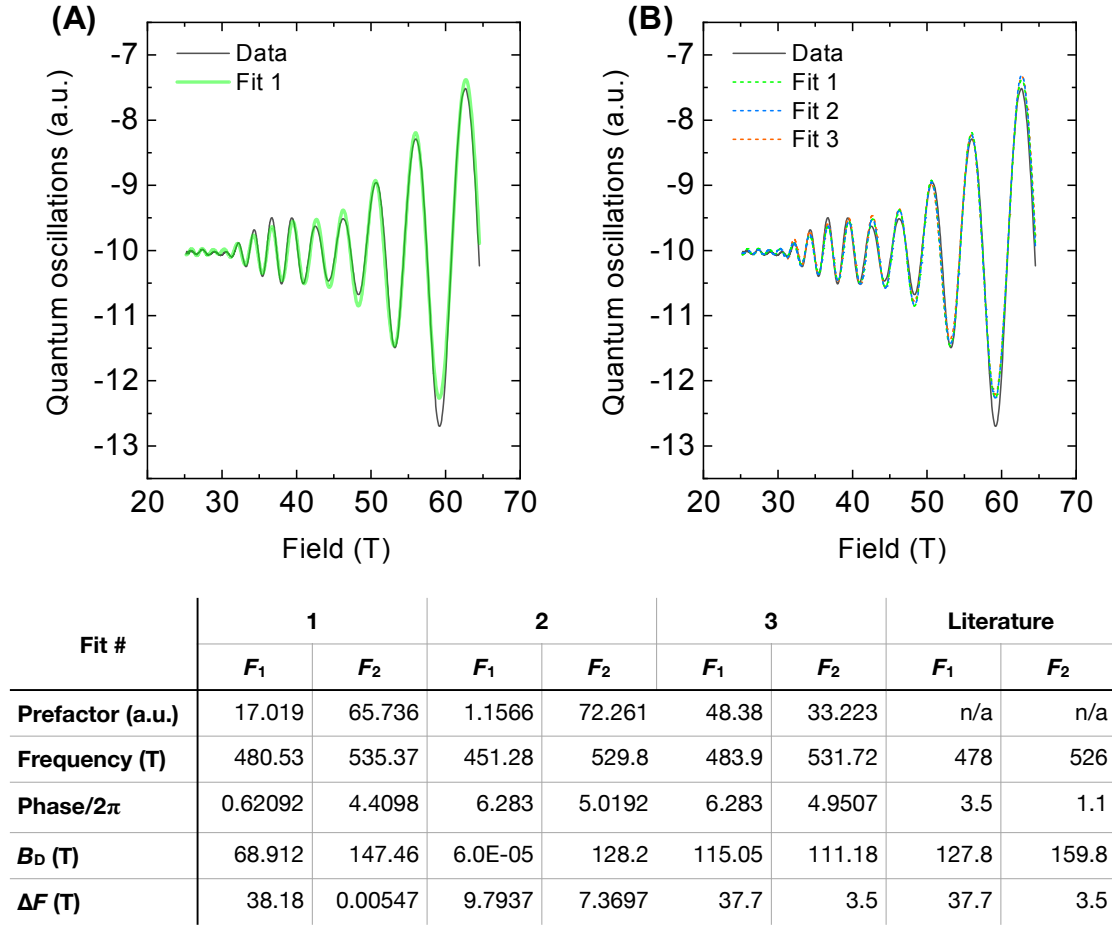


Fig. 3.20. Validating the Particle Swarm fitting algorithm. (A) A test fit using the Particle Swarm algorithm to simulate quantum oscillations measured on $\text{YBa}_2\text{Cu}_3\text{O}_{6.56}$ with a field alignment of $\theta = 0^\circ$ as shown in Fig. 4 of Ref. [85]. Good agreement is seen between the fit and the data across the full measured field range. (B) Three independent simulations performed using the Particle Swarm algorithm overlaid with the quantum oscillation data from Ref. [85] shown in (A). Simulation parameters for are presented in the table, which also shows the parameters used for the fit published in Ref. [85]. The fit performed by Ref. [85] includes additional damping terms that account for spin splitting, which is not field dependent, and has therefore been simplified into a single prefactor term for the Particle Swarm fits. Fits #1 and #2 were performed with $\Delta F_{\text{neck - belly}}$ as free parameters, while Fit #3 was performed with $\Delta F_{\text{neck - belly}}$ values from Ref. [85]. Good agreement is seen for the three fits despite their varying parameters.

3. Experimental Methods

Chapter 4

Unconventional insulating quantum oscillations in YbB_{12}

4.1 Introduction

YbB_{12} is an f -electron Kondo insulator with similar physical properties to SmB_6 . First synthesized in 1983 [45], electrical transport measurements on YbB_{12} reveal a high temperature energy gap of ≈ 5 meV down to 14 K and a low temperature gap of ≈ 2 meV below [47]. The narrow indirect gaps revealed by contacted transport are accompanied by a direct energy gap of ≈ 200 meV observed using tunneling spectroscopy [86] and optical spectroscopy [87]. While the above electrical properties of YbB_{12} are highly similar to those in SmB_6 , the low temperature resistivity plateau that has been associated with topological surface states in SmB_6 [18] was only recently observed in YbB_{12} [88]. ARPES data, likely measured using samples that show a low temperature resistivity plateau, indeed suggest the existence of topological surface conduction states in YbB_{12} [89]. However, it remains to be seen whether YbB_{12} samples without a resistivity plateau would yield comparable ARPES data, and whether a comparably multi-faceted support for surface states in SmB_6 – for instance, by investigating the thickness dependence of resistance ratios [90] and Hall effect [91]

– can be replicated for YbB_{12} .

The similarities between YbB_{12} and SmB_6 continue in their magnetic properties, with both materials showing nonmagnetic ground states at low temperatures. While early polycrystalline YbB_{12} samples show a large susceptibility upturn at low temperatures [45], a suppression of the upturn in high quality single crystal samples suggests that the low temperature ground state is non-magnetic and the upturn is due to impurities [49]. A spin gap of ≈ 10 meV has been observed through neutron scattering measurements [92, 93], with magnetic excitations occurring at an energy scale of ≈ 20 meV and above [94]. However, more recent measurements have raised the prospect that a larger spin gap of ≈ 40 meV could exist, and that lower energy magnetic excitations arise from in-gap modes [95].

The possible existence of in-gap states in YbB_{12} has previously been raised through the observation of a finite residual linear coefficient of the low temperature specific heat capacity in the insulating phase [15], a phenomenon that has also been a puzzling signature of SmB_6 [14]. While a residual linear specific heat capacity could be attributed to impurities rather than in-gap states, recent experiments on high quality samples suggest this not to be the case. Two separate studies conducted on YbB_{12} single crystals have found finite linear specific heat capacity at low temperatures, which remains robust against applied magnetic fields [96, 97] (reproduced in Fig. 4.1A). A finite linear contribution to thermal conductivity at low temperatures has also been reported for YbB_{12} [96] (reproduced in Fig. 4.1B). The linear contribution to thermal conductivity is seen to grow with applied magnetic fields, a behavior that has previously been observed in SmB_6 [12]. Since a linear contribution to thermal conductivity is associated with itinerant fermionic heat carriers, it is unlikely to originate from localized impurities [96]. Relatedly, a finite density of states inside the energy gap of YbB_{12} has also been observed using tunneling spectroscopy [98]. Taken together with the anomalous thermal properties, we find strong evidence for unusual itinerant fermionic states inside the charge gap of YbB_{12} .

More importantly to this thesis, YbB_{12} shows a crucial distinction to SmB_6 with its field-induced insulator-to-metal (IM) transition occurring at as low as 47 T [69, 100]. A sharp change in magnetization is seen, with electrical resistivity decreasing by more than a

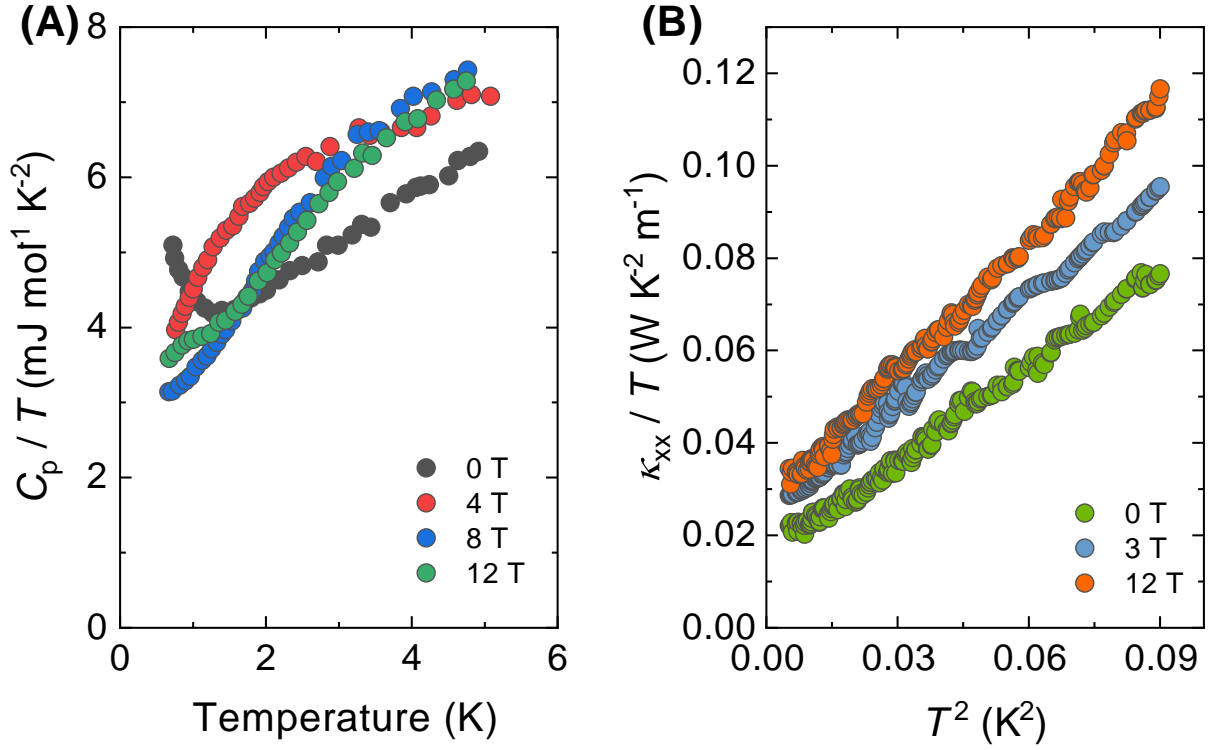


Fig. 4.1. Unusual thermal properties reported for YbB₁₂. (A) Specific heat capacity of YbB₁₂ in various applied magnetic fields as a function of temperature, showing a residual linear contribution at low temperatures in all field strengths. A residual linear contribution to the low temperature specific heat is associated with low energy fermionic excitations and is not expected for an insulator. (B) Longitudinal thermal conductivity of YbB₁₂ in various applied magnetic fields as a function of temperature, showing a residual linear contribution that is enhanced by applied magnetic fields. Such a field-enhanced linear contribution is attributed to itinerant low-energy fermionic excitations, which is not expected in insulators. Both datasets reproduced from Ref. [96].

couple of orders of magnitude leading up to the transition field before plateauing above [69] (reproduced in Fig. 4.2A, B). An associated sharp increase in the linear specific heat capacity has also been reported, suggesting that a heavy fermion phase forms above the transition [97] (reproduced in Fig. 4.2C). Indeed, there is evidence that the Kondo mechanism remains intact above the transition. A recent magnetization study shows the IM transition broadens

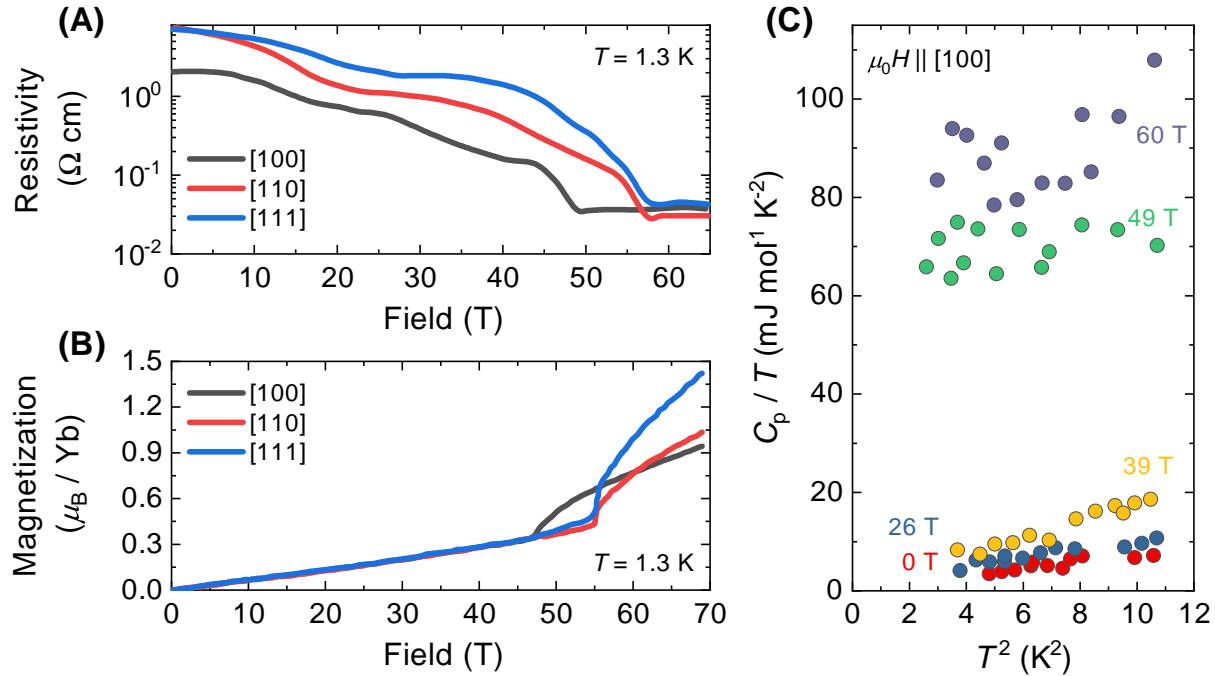


Fig. 4.2. Field-induced insulator-to-metal transition of YbB_{12} . (A) Magnetoresistance of YbB_{12} with the magnetic field applied along three high symmetry directions of [100], [110], and [111]. Resistivity is seen to decrease by orders of magnitude before plateauing above the insulator-to-metal transition fields at $\approx 47 \text{ T}$ along [100] and at $\approx 54 \text{ T}$ along [110] and [111]. Data reproduced from Ref. [69] (B) Magnetization of YbB_{12} with the magnetic field applied along three high symmetry directions of [100], [110], and [111]. A linear magnetization is seen up to the insulator-to-metal transition fields of $\approx 47 \text{ T}$ along [100] and at $\approx 54 \text{ T}$ along [110] and [111], above which the magnetization sharply increases. Data reproduced from Ref. [69]. (C) Specific heat capacity of YbB_{12} as a function of temperature at high applied magnetic fields, with the field applied along the [100] high symmetry direction. A sharp increase in the linear contribution to specific heat is seen above the insulator-to-metal transition field of $\approx 47 \text{ T}$, suggesting that a heavy fermion metallic phase forms above the transition. Data reproduced from Ref. [99].

and vanishes above $\approx 30 \text{ K}$, much lower than the Kondo temperature of $\approx 240 \text{ K}$ [101]. The IM transition is therefore likely to be associated with a lower energy scale phenomenon than than Kondo hybridization. The collapse of Kondo hybridization has been suggested

to occur at ≈ 100 T, where a second sharp change to the magnetization of YbB_{12} has been observed [99]. This point remains speculative, however, as access to high fields above 100 T is limited and complementary measurements are not yet available.

4.2 Sample characterization

For high field quantum oscillation measurements, we use single crystal YbB_{12} samples grown through a collaboration with Dr. Natalya Shitsevalova's group at the National Academy of Sciences of Ukraine in Kiev and Prof. Geetha Balakrishnan's group at Warwick University (see Chapter 3 for details). As described in Chapter 3, elemental characterization of the samples was performed using scanning electron microscopy and x-ray diffraction at Warwick University, while single crystallinity was confirmed using a x-ray Laue diffraction camera in Cambridge.

Low and intermediate field electrical property characterizations performed on the samples in Cambridge agree well with established literature [98, 100]. As shown in Fig. 4.3B, contacted electrical resistivity measurements performed in a Quantum Design Inc. PPMS show a clear exponential upturn that corresponds to the energy gap opening. Applied magnetic fields of 14 T led to a notable suppression of the low temperature resistivity, in agreement with the literature on field-induced gap reduction [69, 100]. The inset to Fig. 4.3B shows an Arrhenius fit to the measured electrical resistivity at ambient magnetic fields, yielding an indirect gap of ≈ 5 meV. The low temperature resistivity plateau that serves as a telltale sign of surface conducting states, a signature of SmB_6 , appears highly sample dependent in YbB_{12} and has yet to be observed in our samples.

Low temperature specific heat capacity measurements performed on our single crystal YbB_{12} samples also agree well with the literature [15], revealing a finite residual linear coefficient that is reminiscent of SmB_6 [12]. Fig. 4.3C shows measured specific heat capacity of a single crystal of YbB_{12} as a function of temperature down to 0.4 K in ambient magnetic field and in an applied field of 14 T. While the value of the linear coefficient at temperatures above the upturn at ≈ 12 K is enhanced by the applied magnetic field, as would be expected

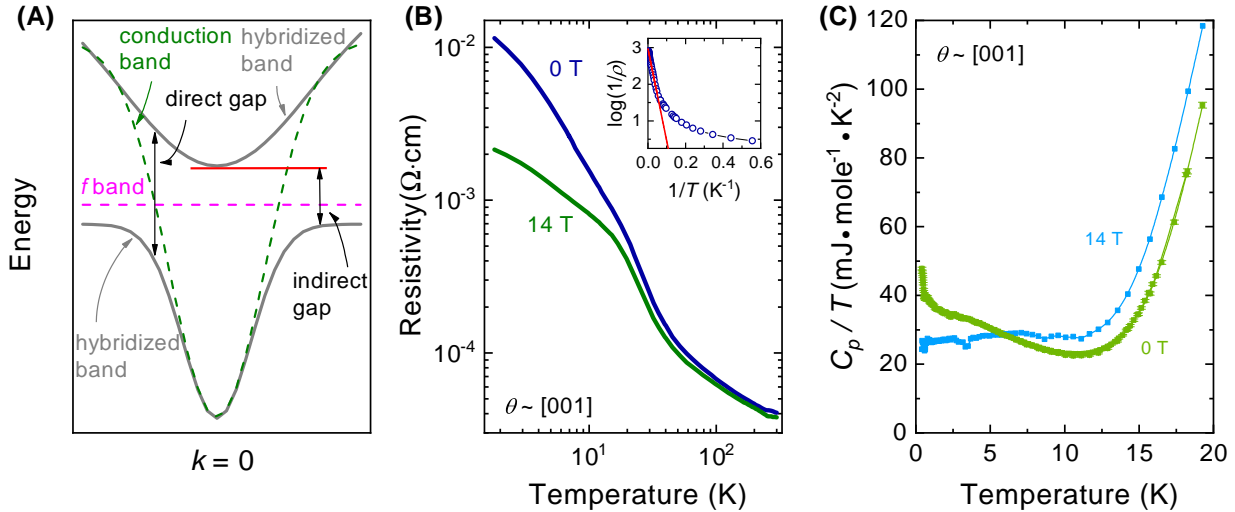


Fig. 4.3. Electrical resistivity and specific heat capacity of YbB_{12} . (A) A schematic diagram depicting the band structure of a Kondo insulator where hybridization between the localized f -electrons and the conduction electrons opens a charge gap. (B) Measured electrical resistivity of a single crystal of YbB_{12} in ambient magnetic field and in an applied field of 14 T between 1.8–300 K, showing a suppression of the resistivity upturn at low temperature with applied field. The electric current and magnetic field were both aligned close to the [001] high symmetry axis. (Inset) An Arrhenius fit to the electrical resistivity revealing a charge gap of ≈ 5 meV. (C) Measured specific heat capacity of a single crystal of YbB_{12} in ambient magnetic field and in an applied field of 14 T down to a temperature of 0.4 K with the field aligned close to the [001] high symmetry axis. A finite linear coefficient γ is observed, reminiscent of the behavior in SmB_6 [12, 102]. The measured linear coefficient is comparable to that reported in Ref. [15]. While the value of the linear term at temperatures above the upturn at ≈ 12 K is enhanced by the applied magnetic field, as would be expected for a reduction in the charge gap, the low temperature upturn is suppressed by the applied field, suggesting its correspondence to a secondary low energy scale that is suppressed by applied magnetic fields.

for a field-induced reduction of the activation gap, the upturn itself is suppressed by the applied field, suggesting an origin in a secondary low energy scale. This trend agrees with recently published specific heat capacity measurements performed on YbB_{12} samples grown by an independent research group in Ref. [96], a portion of which is reproduced in Fig. 4.1.

When selecting samples for high magnetic field quantum oscillation measurements, we choose samples with clean Laue diffraction patterns and high inverse residual resistivity ratios [iRRR $\equiv R(T = 2 \text{ K})/R(T = 300 \text{ K})$, where R is the measured resistance and T is the temperature]. Sample quality is reflected by iRRR in two ways. Since YbB₁₂ is a conductor at room temperature, impurities and imperfections in the crystal lead to a higher scattering rate that increases resistivity. When the energy gap opens in YbB₁₂ at low temperatures, conduction channels formed by impurities and crystal imperfections suppress resistivity. The effect of impurities and crystal defects on iRRR has previously been studied in SmB₆, where point defects introduced through radiation damage [53] and off-stoichiometry [54] resulted in a decrease in low temperature resistivity and an increase in high temperature resistivity. In SmB₆, the effect of surface conduction states on iRRR also has to be considered. The resistance of SmB₆ becomes independent of sample thickness at low temperatures as a result of surface conduction states; this means that iRRR develops a thickness dependence through the high temperature resistance. In order to compare between samples, the iRRR number has to be divided by sample thickness. It should be noted that this procedure may not be necessary in YbB₁₂, since our samples do not show the low temperature resistance plateau that has been associated with surface conduction states in SmB₆. In practice, we have examined both iRRR and iRRR/thickness out of caution, and found a comparable trend between samples across both methods.

4.3 Quantum oscillations in the unconventional insulating phase of YbB₁₂

Despite the many similarities in transport and thermal properties between SmB₆ and YbB₁₂, YbB₁₂ proves to be an important contrast to SmB₆ when it comes to bulk quantum oscillations in the insulating phase. Whereas SmB₆ has thus far only shown quantum oscillations in magnetic torque in its insulating phase, YbB₁₂ exhibits prominent quantum oscillations in both magnetic torque and electrical transport onsetting from far below the field-induced insulator-to-metal transition.

4.3.1 de Haas-van Alphen (dHvA) oscillations

Magnetic torque quantum oscillations in YbB₁₂ were measured in collaboration with colleague Máté Hartstein and published in Ref. [103]. Fig. 4.4A shows the magnetic torque background measured on a single crystal of YbB₁₂ at a temperature of 0.3 K, with the applied magnetic field aligned 13° from the [001] high symmetry in the [001]-[111]-[110] rotation plane. Quantum oscillation peaks are visible on top of the raw background from as low as 35 T.

Since the oscillations are small compared to the background, this is an ideal opportunity to make use of the LOESS background subtraction technique described in Chapter 3. Fig. 4.4B shows a comparison of three different background subtractions on the sweep in Fig. 4.4A, performed using LOESS, a 4th order polynomial fit, and an 8th order polynomial fit. Dashed lines in the figure indicate peaks in the subtracted data; the three peaks at the highest fields are visible on the background, as indicated by arrows in Fig. 4.4A, while peaks at lower fields are only visible after subtraction. We can see that features in the torque revealed by LOESS background subtraction are also visible in the two polynomial subtractions, suggesting that the features are physically real.

Comparing the two polynomial subtractions, we see that polynomial subtraction is prone to introducing spurious signal. The 4th order polynomial subtraction produces three large peaks in the intermediate field ranges, as well as tails at either end of the field window, that are not reproduced in the 8th order polynomial subtraction. Even higher order polynomial fits further improve the subtraction, notably by reducing the discrepancy from LOESS in the field range between 33–35 T. Since high order polynomial subtractions converge toward the LOESS subtraction, we can be confident that the LOESS produces a reliable subtraction of the torque background.

To further improve our noise performance, multiple field sweeps were performed at every temperature and angle for averaging. Fig. 4.5A shows an overlay of six field sweeps after LOESS background subtraction. Although individual sweeps show visible white noise and shot noise, the six sweeps agree exceptionally well overall. Upon averaging the six sweeps,

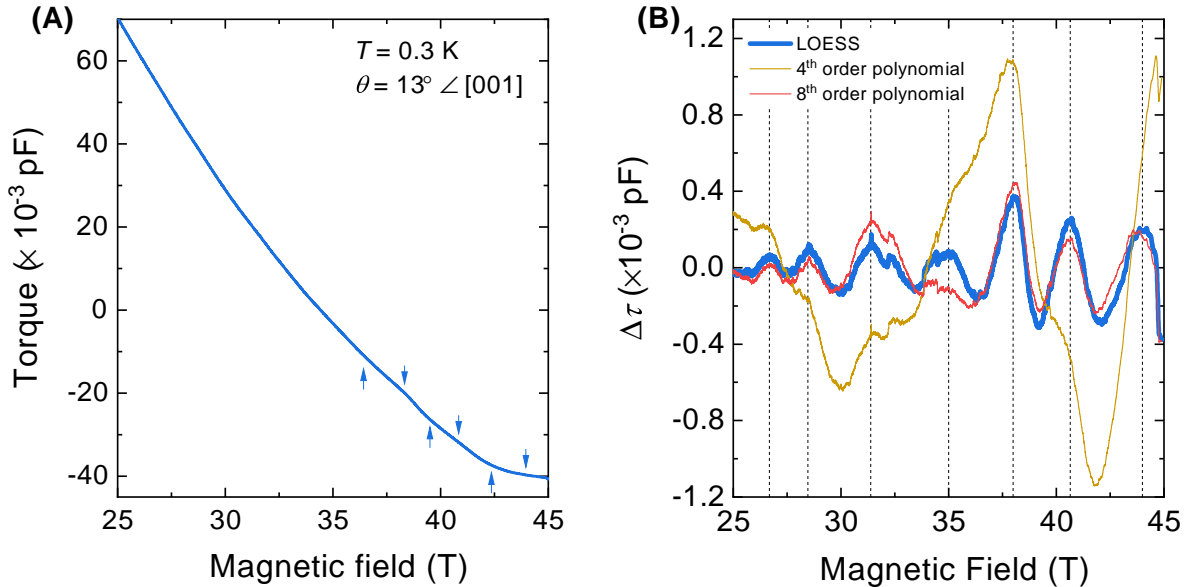


Fig. 4.4. Subtraction of magnetic torque background in insulating YbB_{12} . (A) Magnetic torque background measured on a single crystal of YbB_{12} at a temperature of 0.3 K and a magnetic field tilt angle $\theta = 13^\circ$ from the [001] high symmetry direction in the [001]-[111]-[110] rotation plane. Quantum oscillation peaks are visible on top of the torque background, as indicated by the arrows. (B) Changes in magnetic torque $\Delta\tau$ obtained by three background subtraction methods, using LOESS, a 4th order polynomial fit, and an 8th order polynomial fit. Vertical dashed lines mark peak features in the subtraction, which can be seen across all three sets of subtracted data. Large differences are seen between the two polynomial subtractions, suggesting the method is prone to introducing sizable spurious signal. The 8th order polynomial fit produces a similar subtraction to LOESS; even higher polynomial fits further reduce the difference. High order polynomial subtractions converge toward the LOESS subtraction, suggesting the LOESS produces a reliable subtraction of the torque background.

we arrive at the clean sweep in Fig. 4.5B, where quantum oscillations unambiguously onset from as low as 25 T, far below the insulator-to-metal transition at ≈ 47 T [69, 100].

To determine the frequency of the torque quantum oscillations, we perform Fast Fourier transform (FFT) on the averaged background subtracted data. As shown in Fig. 4.6A, torque quantum oscillations in YbB_{12} consist of two prominent frequencies at the highest measured

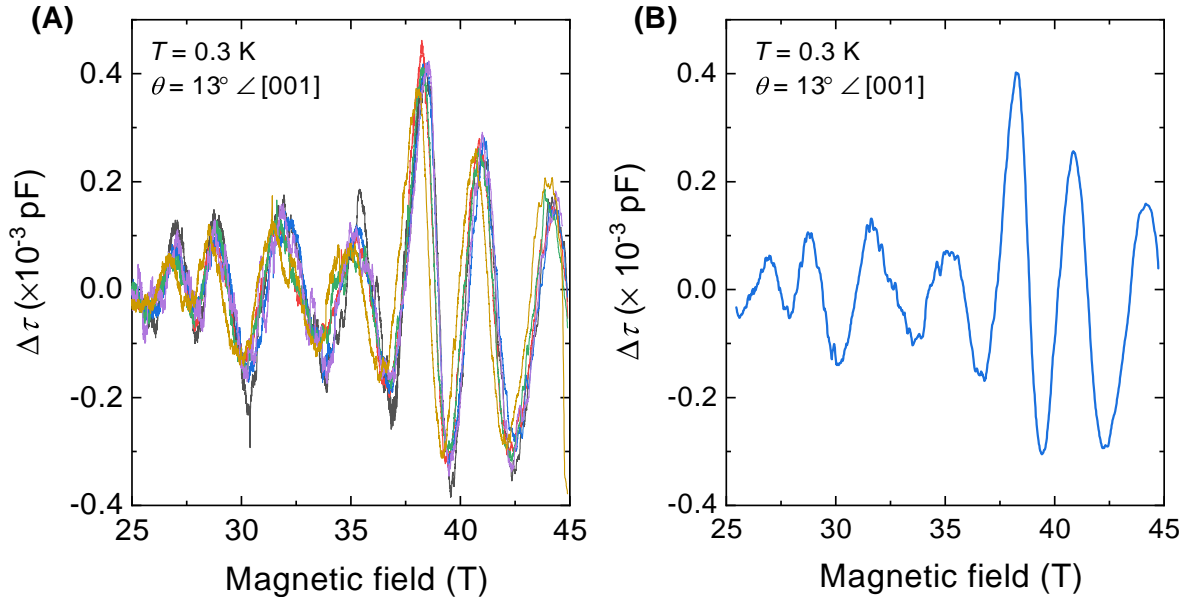


Fig. 4.5. dHvA oscillations in insulating YbB_{12} . (A) Overlay of six background-subtracted magnetic torque $\Delta\tau$ sweeps measured on a single crystal of YbB_{12} at a temperature of 0.3 K and a magnetic field tilt angle $\theta = 13^\circ$ from the $[001]$ high symmetry direction in the $[001]$ - $[111]$ - $[110]$ rotation plane. While individual sweeps are affected by white noise and shot noise, good agreement is seen across all six sweeps. (B) Average of the six background-subtracted magnetic torque sweeps shown in (A), producing a clean signal minimally affected by white noise and shot noise. Quantum oscillations are visible from as low as 25 T, far below the insulator-metal transition at ≈ 47 T [69, 100].

field range, with amplitudes that far exceed the FFT noise floor. By taking the FFT peak amplitudes for each frequency and using the FFT noise floor as the uncertainty, we can use the Lifshitz-Kosevich (LK) analysis to determine the effective mass of each frequency. Fitting to the temperature dependence of the quantum oscillation amplitudes, we find heavy quasiparticle effective masses (m^*) of $4.5(5) m_e$ for the 300(70) T frequency and $7(2) m_e$ for the 700(90) T frequency (Fig. 4.6B and 4.6C).

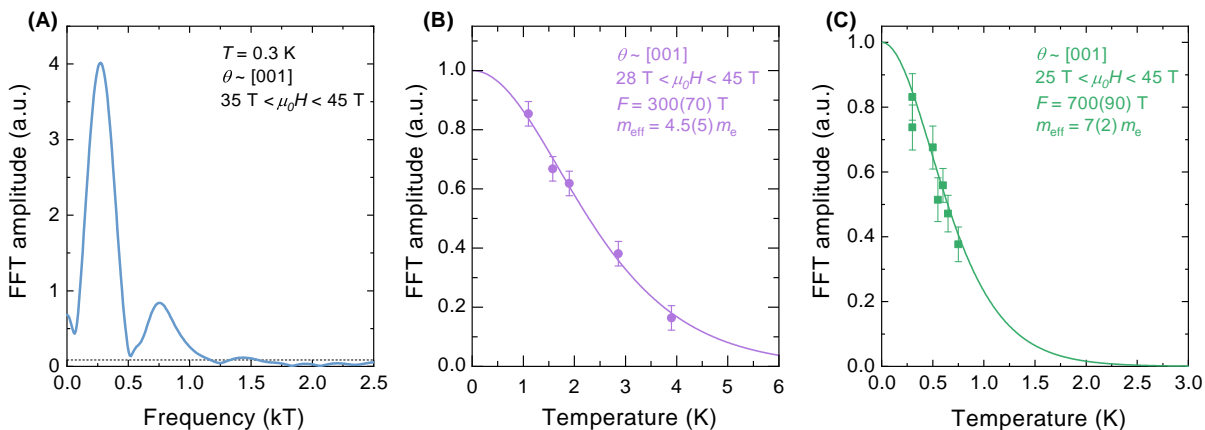


Fig. 4.6. Lifshitz-Kosevich temperature dependence of dHvA oscillations in insulating YbB₁₂. (A) An example fast Fourier transform (FFT) of the background-subtracted dHvA oscillations for a field range of 35–45 T at a temperature of 0.3 K with the magnetic field aligned close to the [001] high symmetry axis. (B and C) Temperature dependence of the dHvA oscillation amplitude for the 300(70) T and 700(90) T frequencies, where the oscillation amplitude is obtained from the FFT amplitudes. Lifshitz-Kosevich fits to the temperature dependence reveal heavy quasiparticle effective masses (m^*) of $4.5(5) m_e$ for the 300(70) T frequency and $7(2) m_e$ for the 700(90) T frequency. The larger uncertainty for the 700(90) T frequency results from the lack of higher temperature data points for this dataset.

4.3.2 Shubnikov-de Haas (SdH) oscillations

In addition to quantum oscillations in magnetic torque, YbB₁₂ exhibits prominent quantum oscillations in electrical resistivity. Fig. 4.7A shows the electrical resistance measured on a single crystal of YbB₁₂ at a temperature of 0.3 K, with the applied magnetic field aligned close to the [001] high symmetry direction. Quantum oscillation peaks can be seen on top of the resistance background from as low as 30 T, as indicated by arrows in the figure.

Similar to magnetic torque, the relatively small quantum oscillation amplitude compared to the resistance background suggest another opportunity to deploy LOESS background subtraction. Fig. 4.7B shows a comparison of three background subtractions, using LOESS, a 4th order polynomial fit, and a 5th order polynomial fit. Here, in contrast to magnetic

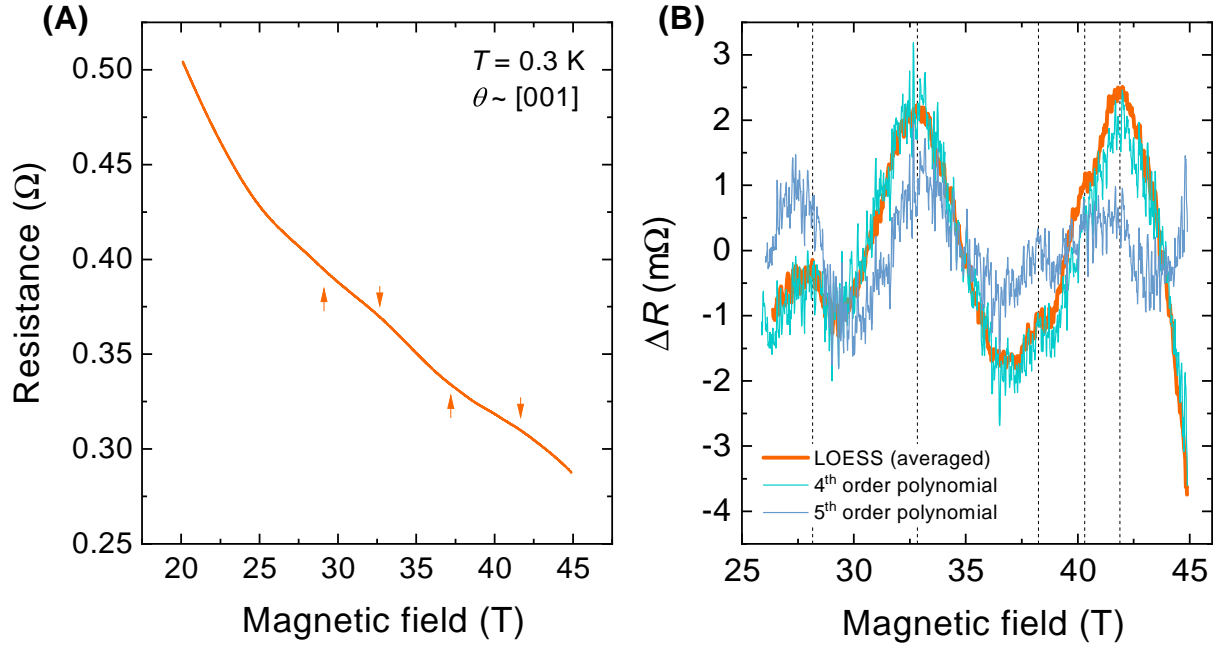


Fig. 4.7. Subtraction of electrical resistance background in insulating YbB_{12} . (A) Measured electrical resistance of a single crystal of YbB_{12} at a temperature of 0.3 K with the applied magnetic field aligned close to the [001] high symmetry axis. Quantum oscillation peaks are visible on top of the background resistance, as indicated by the arrows. (B) Changes in measured electrical resistance ΔR obtained by three background subtraction methods, using LOESS, a 4th order polynomial fit, and a 5th order polynomial fit. Vertical dashed lines mark peak features in the subtraction, which can be seen across all three sets of subtracted data. While good agreement is seen between LOESS and the 4th order polynomial subtraction, notable differences appear to the 5th order polynomial subtraction. Since the Dingle envelope of the dominant low frequency oscillation is expected to lead to an increase in the overall oscillation amplitude with field, in agreement with the LOESS and 4th order polynomial subtractions, the 5th order polynomial subtraction likely overfits the data.

torque, the 4th order polynomial fit produces a subtraction that closely follows the LOESS subtraction. While the 5th order polynomial fit shows similar peak and trough features, the amplitude of these features are different from those in the other two subtraction methods. To determine which subtraction method is more realistic, we appeal to the fact that Dingle damping of quantum oscillations decreases with increasing field. As we will see below, SdH

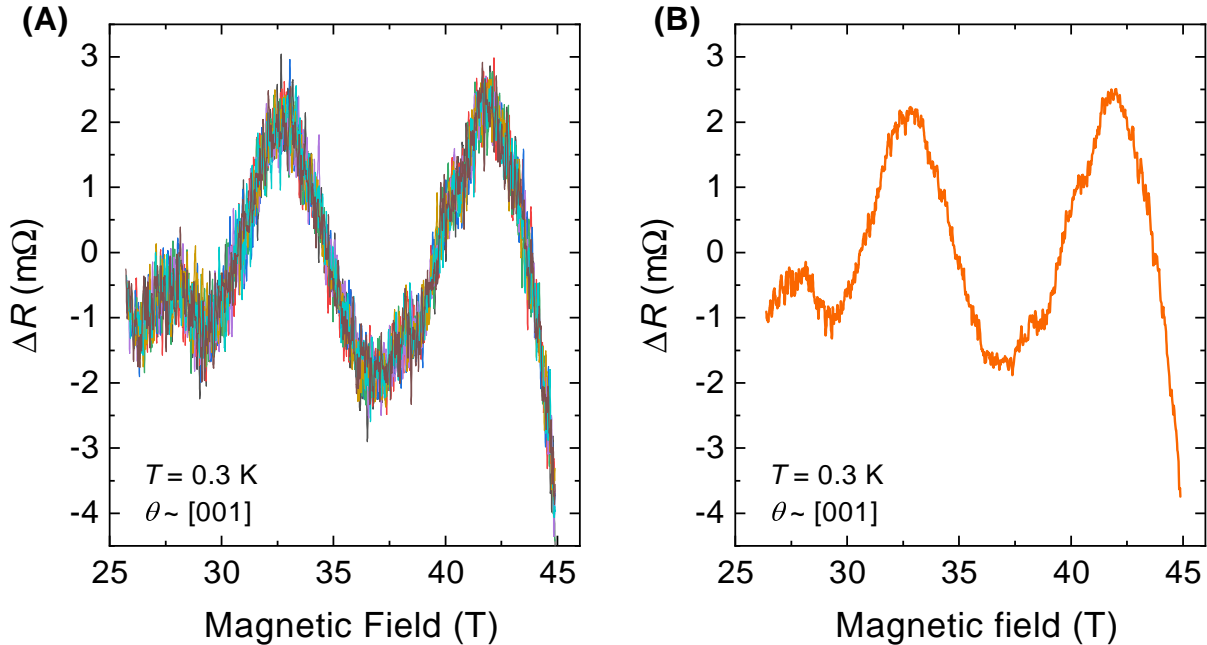


Fig. 4.8. SdH oscillations in insulating YbB_{12} . (A) Overlay of eight background-subtracted electrical resistance ΔR field sweeps measured on a single crystal of YbB_{12} at a temperature of 0.3 K with the applied magnetic field aligned close to the [001] high symmetry axis. Good agreement is seen between all eight sweeps. (B) Average of the eight background-subtracted electrical resistance field sweeps shown in (A), producing a clean signal minimally affected by white noise and shot noise. Quantum oscillations are visible from as low as 25 T, while smaller amplitude high frequency oscillations on top of the lower frequency oscillations become visible above ≈ 35 T.

oscillations in insulating YbB_{12} consists of a dominant slow frequency accompanied by two faster ones with notably smaller amplitudes. The Dingle envelope of the dominant frequency is expected to lead to an increase in quantum oscillation amplitude with increasing field, in agreement with the LOESS and 4th order polynomial subtractions. It is therefore likely that the 5th order polynomial subtraction overfits the data, thereby leading to a dominant oscillation that decreases in amplitude with increasing field.

As we can see from the subtractions in Fig. 4.7B, electrical transport signal tends to be

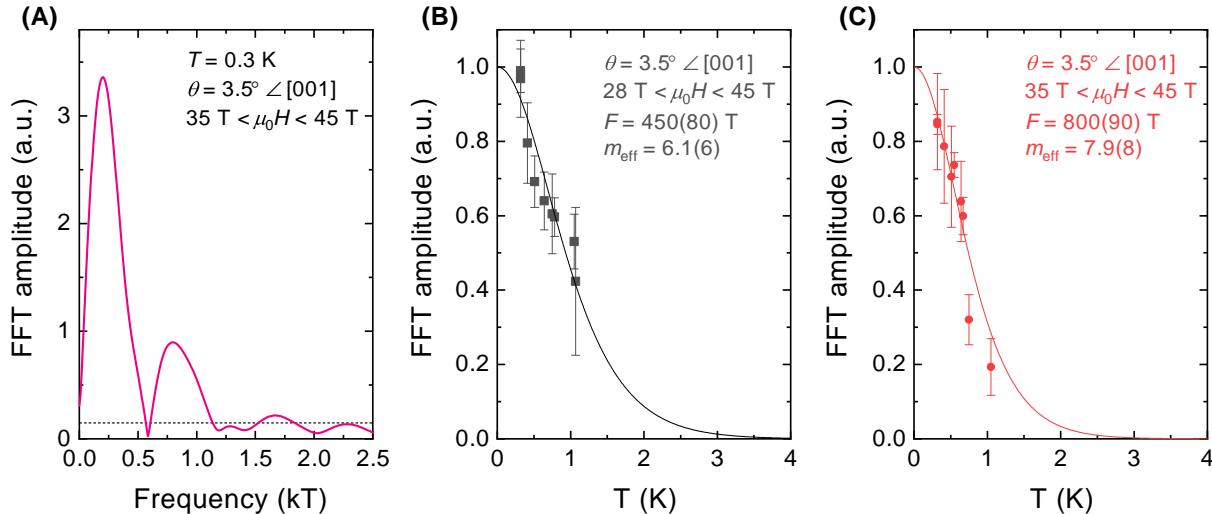


Fig. 4.9. Lifshitz-Kosevich temperature dependence of SdH oscillation in insulating YbB_{12} . (A) An example Fast Fourier transform (FFT) of the background-subtracted SdH oscillations for an applied magnetic field range of 35–45 T at a tilt angle $\theta = 3.5^\circ$ from the [001] high symmetry direction in the [001]-[111]-[110] rotation plane. (B and C) Temperature dependence of the quantum oscillation amplitude for the 450(80) T and 800(90) T frequencies, where the oscillation amplitude is obtained from the FFT amplitudes. Lifshitz-Kosevich fits to the temperature dependence reveal heavy quasiparticle effective masses (m^*) of 6.1(6) m_e for the 450(80) T frequency and 7.9(8) m_e for the 800(90) T frequency.

affected by sizable white noise. While we have gone to great lengths to optimize the sample geometry and the measurement setup, details of which are explained in Chapter 3, the size of the grown single crystal boules limits the level of optimization that could be made. To further improve our measured signal-to-noise ratio, we average multiple field sweeps. Fig. 4.8A shows an overlay of eight field sweeps after LOESS background subtraction. Good agreement is seen across the eight sweeps, and an average of the eight, shown in Fig. 4.8B, reveals a clean oscillation profile. Similar to the case of magnetic torque, we see that SdH oscillations in insulating YbB_{12} onset from fields as low as 25 T, far below the insulator-to-metal transition at $\approx 47 \text{ T}$ [69, 100].

Following the same procedure as magnetic torque, we determine the SdH oscillation fre-

quency by performing FFTs on the background-subtracted signal. As shown in Fig. 4.9A, two prominent frequency peaks are visible in the highest measured field range, with amplitudes far above the FFT noise floor. A third peak at ≈ 450 T is visible as a shoulder to the ≈ 150 T peak. By taking the FFT peak amplitudes and using the FFT noise floors as error, we can perform LK analysis on the SdH oscillations in the same way as the torque oscillations. Fits to the temperature dependence of the SdH oscillation amplitude reveal moderately heavy quasiparticle effective masses (m^*) of $3.2(2) m_e$ for the 150(90) T frequency, $6.1(6) m_e$ for the 450(80) T frequency, and $7.9(8) m_e$ for the 800(90) T frequency (Figs. 4.9B and 4.9C). The observed SdH oscillation frequencies and effective masses are very similar to those observed for dHvA oscillations, suggesting a common origin between the two types of quantum oscillations. A summary of the observed quantum oscillation frequencies and their corresponding effective masses is shown in Table 4.1.

4.4 Quantum oscillations in the field-induced metallic phase of YbB₁₂

YbB₁₂ has a relatively accessible anisotropic insulator-to-metal transition that onsets at applied magnetic fields between 47–54 T [69]. This provides us with an opportunity to measure quantum oscillations in the field-induced metallic phase using pulsed magnetic fields and compare them to those observed in the insulating phase.

We employed the proximity detector oscillator (PDO) technique to measure quantum oscillations in the field-induced metallic phase of YbB₁₂. Fig. 4.10A shows PDO resonant frequency measured during the rising portion of a field sweep on a single crystal of YbB₁₂, with the applied magnetic field aligned close to the [001] high symmetry direction. A sharp change in the measured PDO resonant frequency is seen at ≈ 47 T, corresponding to the onset of the insulator-to-metal transition [69, 100]. Above the transition, prominent oscillations on top of the PDO background can be seen.

In contrast to DC magnetic field measurements in the insulating phase of YbB₁₂, it

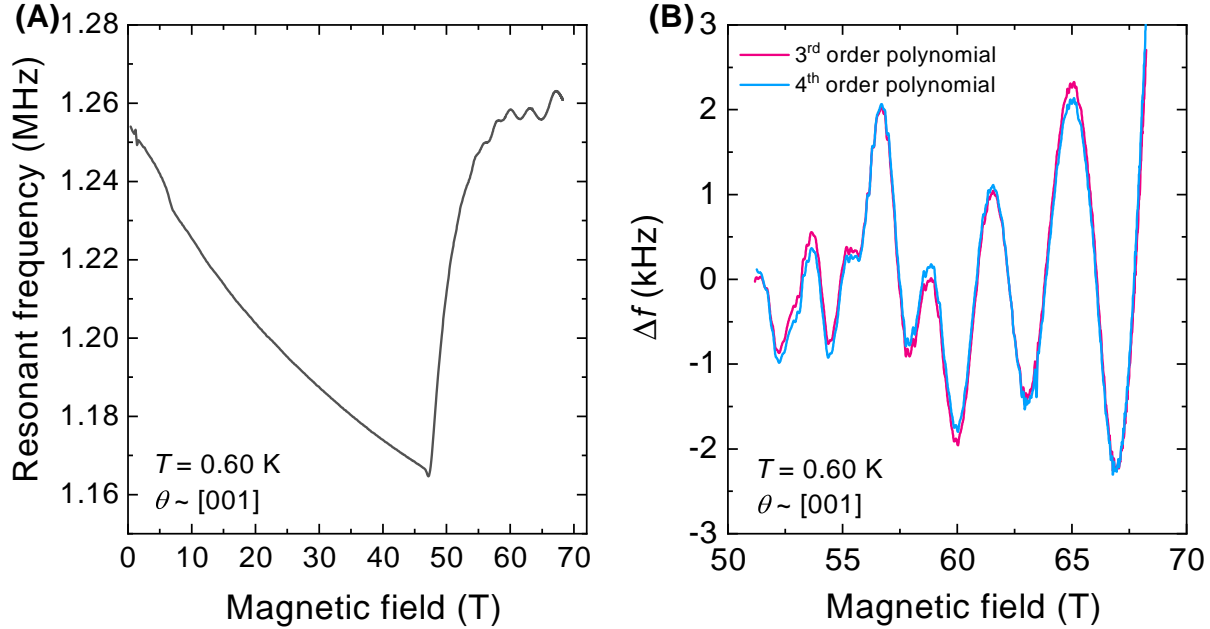


Fig. 4.10. Quantum oscillations in electrical transport measured in the high magnetic field-induced metallized phase of YbB_{12} . (A) Electrical transport measured with the contactless proximity detector oscillator (PDO) technique on a single crystal of YbB_{12} at a temperature of 0.6 K with the applied magnetic field aligned close to the [001] high symmetry direction. The insulator-to-metal transition is reflected by the sharp change in the resonant frequency at ≈ 47 T [69]. Above the transition, large amplitude quantum oscillations are visible on top of the measured PDO background. (B) Changes in the PDO resonant frequency Δf obtained by two background subtraction methods, using a 3rd order polynomial fit and a 4th order polynomial fit. Good agreement is seen between the two subtractions, suggesting that minimal spurious signal is introduced by either method.

was impractical to average multiple field sweeps with the 70 T pulsed magnet in Dresden due to the long cooling time of over three hours. Fortunately, the large signal size in the metallic phase allowed us to extract clean quantum oscillations without the need to average. Fig. 4.10B shows oscillations extracted using two background subtraction methods, a 3rd order polynomial fit and a 4th order polynomial fit, from the sweep shown in Fig. 4.10A. Good agreement is seen between the two subtractions, suggesting that minimal spurious

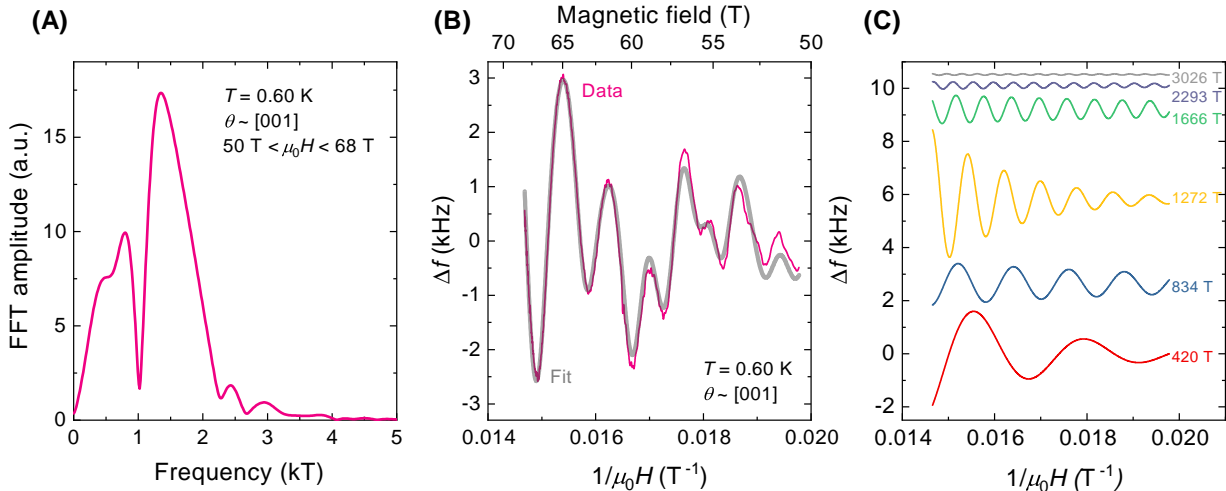


Fig. 4.11. Quantum oscillations in electrical transport measured in the high magnetic field-induced metallized phase of YbB_{12} . (A) FFT of the background subtracted oscillations shown in Fig. 4.10B. Multiple frequencies from ≈ 400 T up to ≈ 3000 T can be seen. (B) Background subtracted oscillations from Fig. 4.10B plotted in reciprocal field (solid red line), overlaid with a simulation of the oscillations using the six frequencies visible in the FFT in (A) (solid grey line). The prefactor, phase, and Dingle damping for each frequency were left as free parameters, while the frequencies were allowed to vary within a small range from the FFT peaks. The simulation shows good overall agreement with the measured data and faithfully reproduces the location of all peak features seen in the data. (C) Component frequencies used to produce the simulation shown in (B). The components show reasonable relative amplitudes when viewed in comparison with the FFT in (A), as well as sensible Dingle damping.

signal is produced by either method. As previously noted in Chapter 3, the large oscillation size in the metallic phase of YbB_{12} makes LOESS unsuitable for the task of background subtraction; the method was therefore not used when analyzing metallic phase oscillations in YbB_{12} .

The complex waveform seen in the metallic phase of YbB_{12} raises the question of whether the oscillations are periodic in reciprocal field. To help address this concern, we simulate the observed oscillations using the particle swarm algorithm introduced in Chapter 3. To begin,

we determine the frequency component of the background subtracted oscillations through an FFT, as shown in Fig. 4.11A. Multiple frequencies between ≈ 400 T and ≈ 3000 T are seen, with varying amplitudes. The six frequencies visible in the FFT are supplied to the simulation algorithm, with the prefactor, phase, and Dingle damping as free parameters, and the frequencies allowed to vary within a small range from the FFT peaks. Although the ≈ 1700 T frequency is only visible as a subtle shoulder to the ≈ 1300 T peak in Fig. 4.11A, it becomes more clearly visible at higher temperatures, as shown in Fig. 4.12B, where the peak amplitude decreases with a different temperature damping than the ≈ 1300 T peak. A representative simulation of the background subtracted oscillations is shown in Fig. 4.11B, and the component frequencies are shown in Fig. 4.11C. The simulation agrees well with the measured data, and, crucially, manages to faithfully reproduce the location of all peak features seen in the data. The component frequencies also show reasonable relative amplitudes compared to the relative amplitudes of the FFT peaks in Fig. 4.11A, as well as sensible Dingle damping. The agreement between the simulation and the data therefore suggests that the measured oscillations are periodic in reciprocal field.

To further test whether the measured waveform reflects quantum oscillations, we perform LK analysis on field sweeps measured between 0.60 K and 2.0 K. Fig. 4.12A shows nine field sweeps measured at distinct temperatures after 3rd order polynomial background subtraction. Oscillatory features are exceptionally consistent across the full temperature range, as expected for quantum oscillations. The features are strongly suppressed by increasing temperature, a trend further demonstrated by FFTs of the background-subtracted oscillations in Fig. 4.12B. Using the FFT peak amplitudes and the noise floor as the uncertainty, an LK analysis of the temperature dependent oscillation amplitude reveals heavy quasiparticle effective masses (m^*) between $8.5(1) - 17(3) m_e$, as shown in Fig. 4.12C. The good agreement with LK temperature dependence and successful simulation of the measured waveform together serve as strong evidence that our data indeed reflects quantum oscillations. A summary of the quantum oscillation frequencies and their corresponding effective masses in both the insulating and metallic phases of YbB_{12} is shown in Table 4.1.

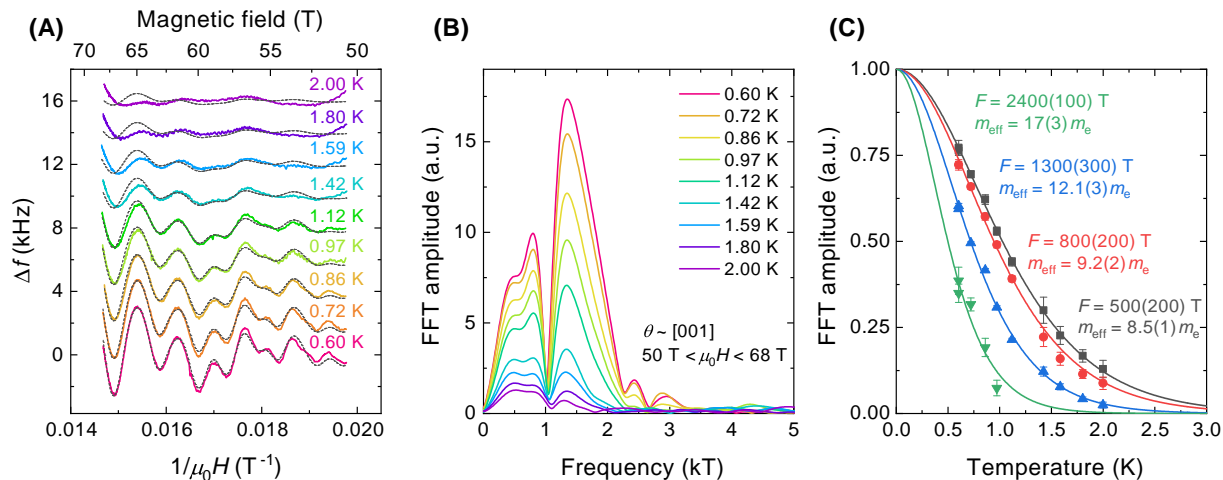


Fig. 4.12. Lifshitz-Kosevich temperature dependence of the quantum oscillations measured in high magnetic field-induced metallic phase of YbB₁₂. (A) Solid lines show changes in PDO resonant frequency Δf after 3rd order polynomial background subtraction. The oscillations are rapidly suppressed with increasing temperature, as expected for quantum oscillations with heavy effective masses. Dashed lines show simulations of the observed oscillations using all six frequencies seen in Fig. 4.11A, where a fit was performed on the subtracted oscillations at 0.6 K, and the temperature parameter was changed for higher temperature data without refitting. Details on the simulation procedure can be found in Chapter 3. (B) FFTs of the background-subtracted quantum oscillations at various temperatures shown in (A) for the field range 50–68 T. Strong temperature suppression of the oscillations is seen. The ≈ 1700 T peak becomes more clearly distinguishable from the ≈ 1300 T frequency at higher temperatures, where the peak amplitude decreases with a different temperature damping than the ≈ 1300 T peak. (C) Temperature dependence of the quantum oscillation amplitude for select frequencies, where the oscillation amplitude is obtained from FFT amplitudes. Lifshitz-Kosevich fits to the temperature dependence reveal heavy quasiparticle effective masses (m^*) of $8.5(1) m_e$ for the 500(200) T frequency, $9.2(2) m_e$ for the 800(200) T frequency, $12.1(3) m_e$ for the 1300(300) T frequency, and $17(3) m_e$ for the 2400(100) T frequency. It is worth noting that although all fits agree comparably well to the data, the higher frequency oscillations have larger uncertainties as they are suppressed to below the noise floor much quicker than lower frequency oscillations.

4. Unconventional insulating quantum oscillations in YbB_{12}

Insulating phase				Metallic phase	
Frequency (T)	Mass (m_e)	Frequency (T)	Mass (m_e)	Frequency (T)	Mass (m_e)
dHvA ($\theta \sim [001]$)		SdH ($\theta = 3.5^\circ \angle [001]$)		PDO ($\theta \sim [001]$)	
		150(90)	3.2(2)	500(200)	8.5(1)
300(70)	4.5(5)	450(80)	6.1(6)	800(200)	9.2(2)
700(90)	7(2)	800(90)	7.9(8)	1300(200)	12.1(3)
				1700(200)	16(5)
				2300(200)	17(3)
				3000(200)	14(3)

Table 4.1. Observed multiple quantum oscillation frequencies and effective masses in the insulating and metallic phases of YbB_{12} . Multiple quantum oscillation frequencies and cyclotron effective masses measured with capacitive torque magnetization (dHvA) and four-point contacted resistivity (SdH) in the insulating phase of YbB_{12} , and with proximity detector oscillator (PDO) contactless electrical transport in the magnetic field-induced metallic phase of YbB_{12} . The applied magnetic field was aligned close to the $[001]$ high symmetry direction for dHvA and PDO measurements, and was aligned 3.5° from the $[001]$ high symmetry direction in the $[001]$ - $[111]$ - $[110]$ rotational plane for the SdH measurements. The FFT field range was $50 \text{ T} < \mu_0 H < 68 \text{ T}$ for PDO, $35 \text{ T} < \mu_0 H < 45 \text{ T}$ for the 800 T frequency in SdH, $25 \text{ T} < \mu_0 H < 45 \text{ T}$ for the 700 T frequency in dHvA, and $28 \text{ T} < \mu_0 H < 45 \text{ T}$ for other frequencies in dHvA and SdH.

4.5 Bulk origin of quantum oscillations in the unconventional insulating phase

The question of whether the unconventional insulating phase quantum oscillations arise from bulk or surface states has been a hotly contested topic since the discovery of quantum oscillations in SmB_6 [11, 104]. As was the case for SmB_6 , two primary routes to address this question include determining the absolute amplitude of the torque oscillations and mapping the angle dependence of oscillation frequencies [11, 12, 103]. A comprehensive treatment of this question was given in a recent thesis by colleague Máté Hartstein [105]; I will follow a similar analysis here for completeness of our discussion.

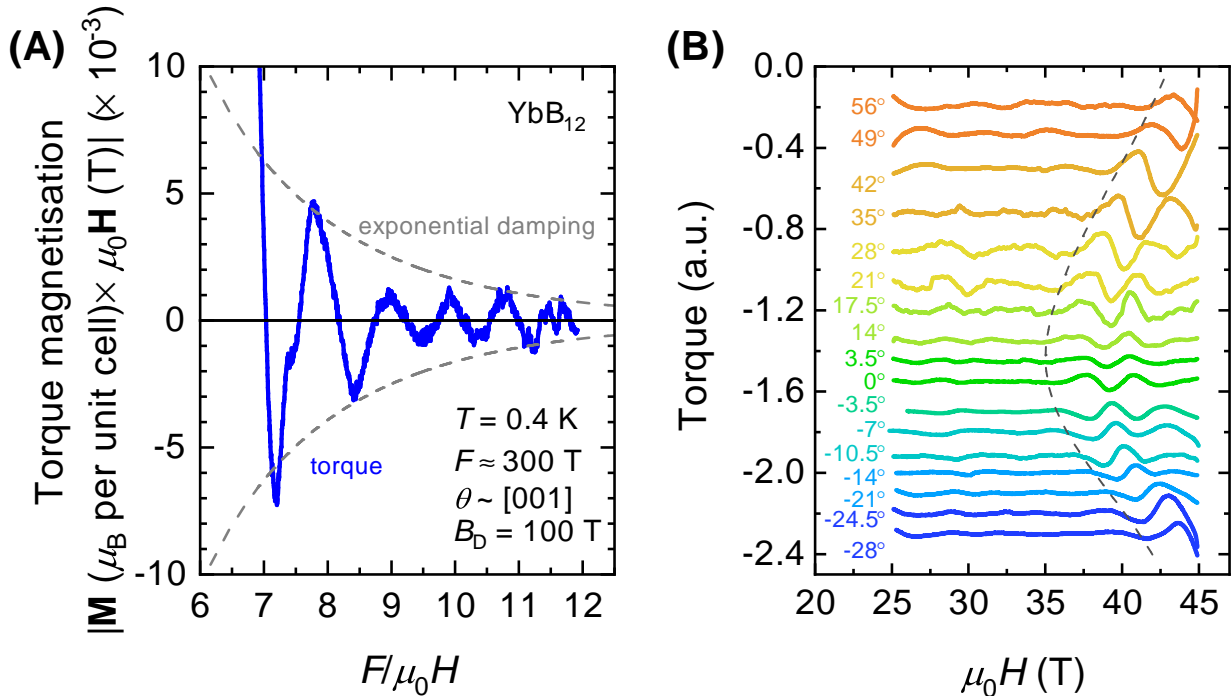


Fig. 4.13. Evidence for bulk origin of quantum oscillations in insulating YbB_{12} . (A) Magnetic torque quantum oscillations converted to absolute units of Bohr magnetons (μ_{B}) per unit cell for the dominant 300 T frequency. (B) Magnetic torque quantum oscillations measured across a wide range of magnetic field tilt angles. The dashed line is a guide to the eye showing the approximate onset fields of prominent quantum oscillations as a function of angle.

We first convert the measured torque signal from capacitance into absolute units of μ_{B} per unit cell. Using the Lifshitz-Kosevich formula, we can estimate the theoretical amplitude of magnetic torque quantum oscillations to be between $1-4 \times 10^{-4} \mu_{\text{B}}$ per unit cell at an applied magnetic field of 45 T for the dominant 300(70) T frequency (see Appendix A for details on the calculation). This agrees to within an order of magnitude with the experimentally measured torque amplitude, as shown in Fig. 4.13A. In contrast, if the measured magnetic torque is attributed solely to surface layers, which occupy approximately 1 in 10^4 unit cells in a typical sample for torque measurements, the absolute amplitude per unit cell would be

4. Unconventional insulating quantum oscillations in YbB₁₂

exceedingly large. The order of magnitude agreement between the LK theoretical estimate and the experimentally measured quantum oscillation amplitude therefore serves as a strong evidence against quantum oscillations arising from surface states or impurity inclusions.

The angle dependence of quantum oscillation frequency is less straightforward to investigate in YbB₁₂ than it was in SmB₆ [11, 12], due to a correlation between the angle-dependent insulator-to-metal transition and the onset of quantum oscillations in the unconventional insulating phase. While sizable quantum oscillations are visible from as low as ≈ 25 T when the field is aligned close to the [001] high symmetry direction, both our group and Ref. [88] have observed the quantum oscillation onset shift notably higher in field at angles towards the [111] and [110] high symmetry directions (Fig. 4.13B). Although we and Ref. [88] have arrived at a comparable interpretation of electrical transport quantum oscillations as arising from the sample bulk, we have come to contrasting interpretations of torque quantum oscillations. Whereas our group sees minimal angular dependence of the quantum oscillation frequencies [103], Ref. [88] argue that torque quantum oscillation frequencies follow a two-dimensional angular dependence. The contrasting interpretations are difficult to resolve without measuring magnetic torque to magnetic fields above 45 T, as the increase in quantum oscillation onset field limits us to a small range of angles where a meaningful number of oscillation peaks can be resolved below 45 T.

Despite the inconclusive evidence on the angle dependence of quantum oscillation frequency, it should be noted that, unlike electrical transport, magnetic torque is a bulk technique that captures contributions from the entire sample. Further, the correlation between the quantum oscillation onset and the bulk insulator-to-metal transition fields suggest the oscillation are inherent to the bulk of the material. Considered in light of the order of magnitude agreement between theoretical and experimental quantum oscillation amplitudes, it would be difficult to imagine that such large torque signals observed by both our group and Ref. [88] are due to thin surface layers.

Indeed, complementary measurements of bulk thermodynamic properties suggest charge neutral low energy excitations exist in the insulating bulk of YbB₁₂. As discussed earlier in this chapter, the specific heat capacity of YbB₁₂ was found to exhibit a residual linear

coefficient γ not long after the the material was first synthesized [15, 103]. The finite γ coefficient that is persistent in applied magnetic fields, together with a non-zero temperature linear coefficient of thermal conductivity that is enhanced by applied magnetic fields (Fig. 4.1) [96], complement the large amplitude quantum oscillations as evidence for bulk excitations in the insulating phase of YbB_{12} .

4.6 Gapless origin of quantum oscillations in the unconventional insulating phase

One of the most pressing questions in the study of insulating quantum oscillations is whether the quantum oscillations arise from novel gapless excitations in the charge gap, such as spinons, composite excitons, or Majorana fermions [106–111] or gapped excitations, such as tunneling or Kondo breakdown [112–117]. To distinguish between gapless and gapped models of quantum oscillations in the unconventional insulating phase, we turn to the temperature dependence of the quantum oscillation amplitude observed in YbB_{12} .

To examine the possibility of gapped excitations, we examine the simplest case of a weakly interacting gapped system with a single particle gap. Models of such gapped excitations have for example been proposed for BCS superconductors [112] and for weakly interacting insulators [113, 114]. Experimentally, such behavior have for instance been observed in unconventional superconductors, where quantum oscillations are visible in the vortex state of these systems despite the existence of a finite superconducting gap [118–121]. For this category of gapped models of quantum oscillations, the quantum oscillation amplitude is expected to plateau or peak at low temperatures. The cause of a plateau or peak in quantum oscillation amplitude is most easily pictured in the case of tunneling: the lower the thermal energy in the system, the harder it is for a quasiparticle to tunnel across the energy gap and contribute to quantum oscillations. Such behavior contrasts the prediction of conventional LK theory, where the quantum oscillation amplitude is expected to follow a $X/\sinh(X)$ dependence on temperature down to 0 K [13]. Other models of weakly interacting gapped

systems invoke quantum oscillations arising from modulation of the gap resulting from an inverted band structure, which also predict a saturation in the quantum oscillation amplitude that deviate from the LK model [115–117].

This picture is modified in the case of strongly correlated insulators, which are expected to host novel excitations inside the charge gap that are driven by strong correlation. Even pre-dating the discovery of quantum oscillations in SmB_6 , models of single-band Mott insulators hosting a Fermi sea comprising low energy spin excitations have been proposed [106, 107]. Following the discovery of quantum oscillations in SmB_6 , numerous theories of novel, non-conductive low energy fermionic excitations have been put forward. For instance, Majorana fermions [108–110] and composite fermionic excitons [111] are expected to host charge-neutral Fermi seas that give rise to quantum oscillations without participating in charge transport. A more detailed discussion of the models proposed thus far will be given in Chapter 6; for the purpose of distinguishing quantum oscillations from gapped and gapless excitations, we note that quantum oscillation amplitudes in gapless models are expected to increase at low temperatures, for instance obeying an LK form in the case of low energy excitations that follow Fermi-Dirac statistics.

In order to distinguish between gapless and gapped models of quantum oscillations, we therefore turn to the growth of quantum oscillation amplitudes at low temperatures. As previously shown in Fig. 4.12B, quantum oscillation amplitudes in the field-induced metallic phase of YbB_{12} grows in accordance with the LK theory down to the lowest measured temperatures, as expected for a metal with low-energy excitations that obey Fermi-Dirac statistics. The presence of neutral gapless excitations in the insulating phase is expected to produce a similar increase in quantum oscillation amplitude at low temperatures. In contrast, a gapped origin of quantum oscillations would be expected to yield a non-LK plateau or decrease in quantum oscillation amplitudes at low temperatures [112, 113]. As shown previously in Fig. 4.6 for magnetic torque and Fig. 4.9 for electrical resistivity, the amplitude of both types of quantum oscillations observed in the insulating regime of YbB_{12} agree well with the LK theory down to the lowest measured temperatures, far below the gap temperature beneath which gapped models of quantum oscillations predict a plateau or decrease in amplitude.

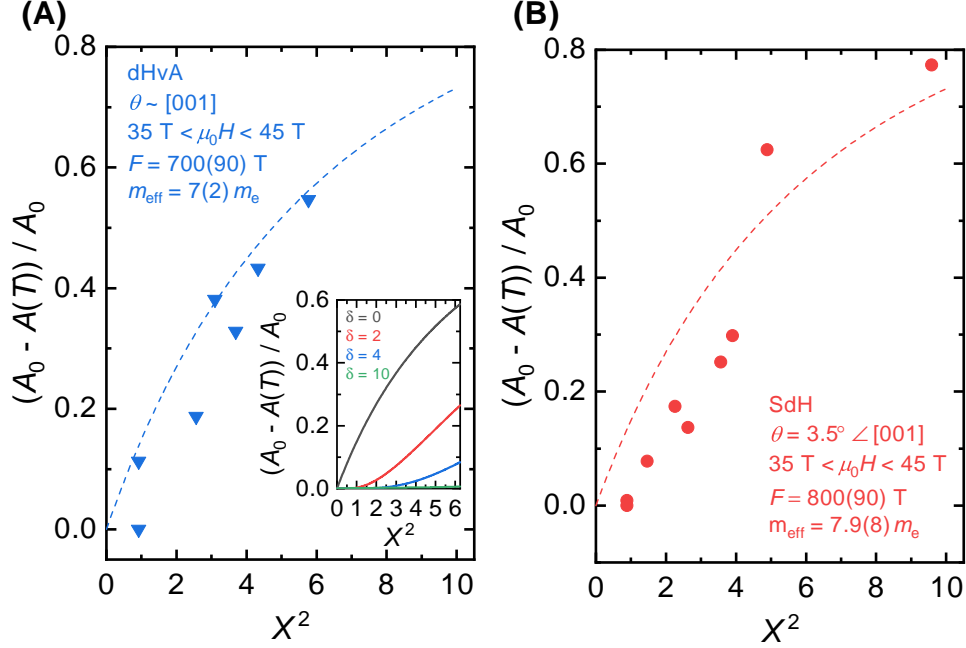


Fig. 4.14. Gapless low energy excitations yield low temperature Lifshitz-Kosevich growth of quantum oscillation amplitude in the insulating phase of YbB_{12} . (A) Low temperature expansion highlighting the growth of 700 T frequency dHvA oscillation in the insulating phase at the lowest measured temperatures, with the applied magnetic field aligned close to the [001] high symmetry direction (derivation in Appendix B). $A(T)$ is the quantum oscillation amplitude at temperature T , A_0 is the amplitude at the lowest measured temperature, $X = 2\pi^2 k_B T / \hbar \omega_c$ is the temperature damping coefficient in the LK formula [13], $\delta = 2\pi\Delta / \hbar \omega_c$ where Δ is the isotropic gap size and ω_c is the cyclotron frequency. Experimental data (solid triangles) exhibits good agreement with gapless model simulation (dashed line). (Inset) Low temperature expansion of quantum oscillation amplitude expected for gapped models as described in Refs. [112, 113], showing non-LK activated behavior for various finite gap sizes. Such non-LK behavior contrasts the exponential growth in amplitude expected for gapless low energy excitations ($\delta = 0$). The gap size of YbB_{12} at 40 T is $2\Delta \approx 15 \text{ K}$, which for the 700 T frequency dHvA oscillation with an effective mass of $7 m_e$ corresponds to $\delta \approx 12$ [100]. Model calculations are shown in Appendix B. (B) Low temperature expansion highlighting the growth of the 800 T frequency SdH oscillations in the insulating phase at the lowest measured temperatures, with the applied field aligned 3.5° away from the [001] high symmetry direction in the [001]-[111]-[110] rotation plane. Measured quantum oscillation amplitude (solid circles) exhibits good agreement with gapless model simulation (dashed line).

The growth in the measured quantum oscillation amplitude at low temperatures can be further highlighted by comparing a low temperature expansion of the data to model simulations of the oscillation amplitude arising from gapped models. As shown in the inset to Fig. 4.14A, gapped models of quantum oscillations experience a strong amplitude suppression even for small gap sizes (a derivation of the model is given in Appendix B). For insulating YbB₁₂, the isotropic gap size is $2\Delta \approx 15$ K [100] at 40 T, the mean of the field range in which the temperature dependence of quantum oscillation amplitudes was measured. Gapped models with such a gap size would be expected to show an almost constant quantum oscillation amplitude at the low temperatures. The measured quantum oscillation amplitudes in both magnetic torque and electrical resistivity, low temperature expansions of which are shown in Fig. 4.14A and Fig. 4.14B, respectively, instead exhibit significant growth at the lowest measured temperatures. The low temperature growth in quantum oscillation amplitude agrees well with the expectation for gapless models ($\delta = 0$ in Fig. 4.14A inset), rather than that of gapped models (the gap size of YbB₁₂ at 40 T corresponds to $\delta \approx 12$ for the two frequencies shown in Fig. 4.14). This comparison therefore provides strong evidence that quantum oscillations observed in the insulating phase of YbB₁₂ arise from gapless excitations that do not participate in longitudinal charge transport.

4.7 Insulating Fermi surface mirroring a heavy fermion semimetal

To contextualize our quantum oscillation study of YbB₁₂, we compare the results to the only other insulator in which quantum oscillations have been studied in detail: SmB₆. In SmB₆, high frequency quantum oscillations up to at least 15 kT with low quasiparticle effective masses (m^*) of less than $1 m_e$ have been reported [11, 12, 122]. The high frequency quantum oscillations with light effective masses observed in SmB₆ have been compared to its isostructural non-magnetic metallic counterpart, LaB₆ [123, 124]. As we can see in Fig. 4.15, the similarities between SmB₆ and LaB₆ spans the high quantum oscillation frequency and the geometry of the corresponding Fermi surface sections. This resemblance suggests that

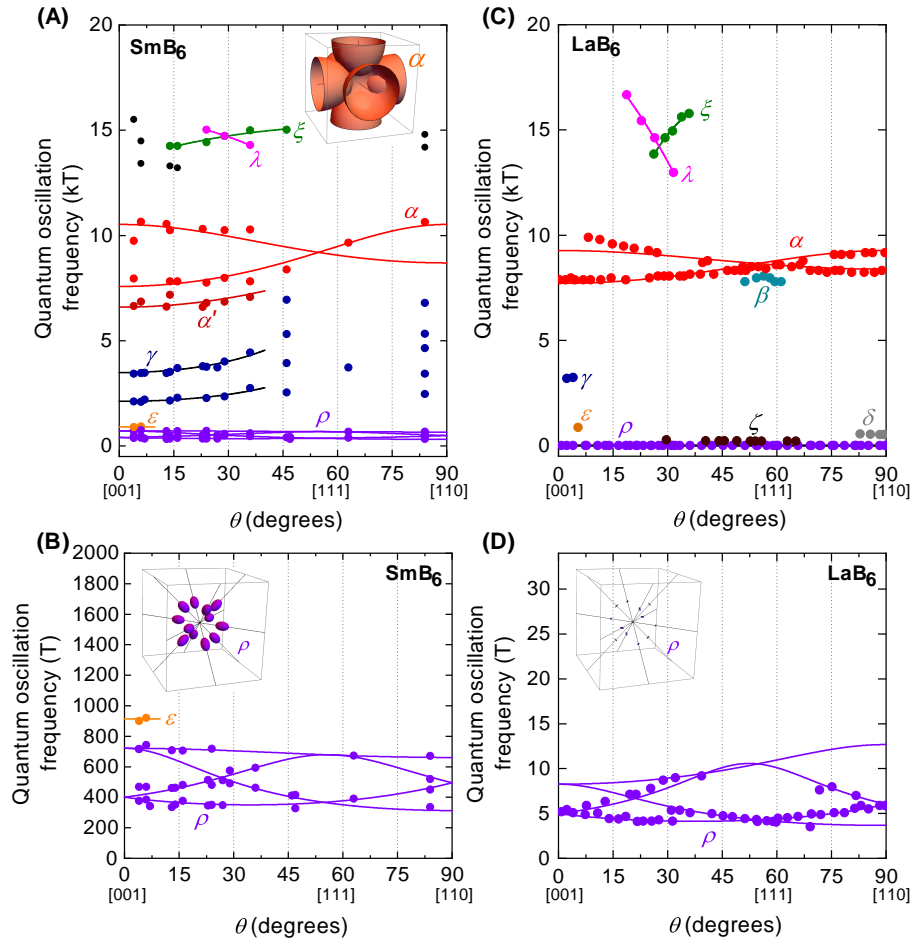


Fig. 4.15. Insulating SmB_6 exhibits conduction electron-like Fermi surface. (A-B) Angular dependence of magnetic torque quantum oscillation frequency measured on single crystal SmB_6 samples grown by the floating zone method that avoids flux contamination. High frequency α oscillations on the order of kT correspond to large Fermi surface sections, a simulation of which is shown in the inset of (A). Fermi surface simulation of the low frequency ρ oscillations is shown as an inset to (B). (C-D) Angular dependence of quantum oscillation frequency of the non-magnetic metallic LaB_6 . The high frequency quantum oscillations on the order of 10's of kT are similar to those in SmB_6 in terms of both frequency and geometry. Low frequency quantum oscillations in the ρ branch also exhibit a similar geometry to the ρ branch in SmB_6 . Figure adapted from Ref. [122], and was made by colleague Máté Hartstein.

4. Unconventional insulating quantum oscillations in YbB₁₂

the insulating Fermi surface in SmB₆ mirrors a conduction electron Fermi surface with highly dispersive carriers.

Following the same prescription, we compare the quantum oscillations observed in the insulating phase of YbB₁₂ to that of its isostructural non-magnetic metallic counterpart, LuB₁₂. In LuB₁₂, quantum oscillations with frequencies up to tens of kT have previously been reported, with associated quasiparticle effective masses (m^*) of no more than $\approx 2 m_e$ for all frequencies [125, 126]. The reported results agree with confirmatory torque measurements performed by colleague Máté Hartstein, whose intermediate field measurements reveal magnetic torque quantum oscillation frequencies up to ≈ 4 kT with light effective masses (m^*) of no more than $0.5 m_e$ (Fig. 4.16A, B). Bandstructure calculations performed by our collaborator Michelle Johannes show dispersive boron bands crossing the Fermi energy in LuB₁₂, with the heavy lutetium d - and f -bands far away from the Fermi energy, in agreement with previous calculations (Fig. 4.16C) [125, 127]. The calculations produce large Fermi surface sections with light effective masses, in agreement with experimental data (Fig. 4.16D). We therefore find that, unlike the case of SmB₆, the small and heavy Fermi surface sections revealed by magnetic torque and electrical transport quantum oscillation measurements on YbB₁₂ do not correspond to those of a dispersive conduction electron Fermi surface from an isostructural non-magnetic dodecaboride.

The comparison to LuB₁₂ suggests that the heavy effective masses observed in YbB₁₂ is influenced by correlation effects. To explore this possibility, our collaborator Michelle Johannes has performed density functional theory calculations for YbB₁₂. To this end, the modified Becke-Johnson (mBJ) potential was used to approximate the exchange interaction with a screening term, which is widely deployed in calculations of semiconductor materials [128]. Spin-orbit coupling was included using the second variational method, and resulted in a strong reordering of the bands. These calculations produce a non-magnetic ground state with an indirectly gap of 21 meV, a direct gap of 80 meV, and a nominally Yb³⁺ semiconducting state, in general agreement with experimental data and previous calculations [47, 86, 87].

Instead of highly dispersive boron bands near the Fermi energy like in LuB₁₂, the band-

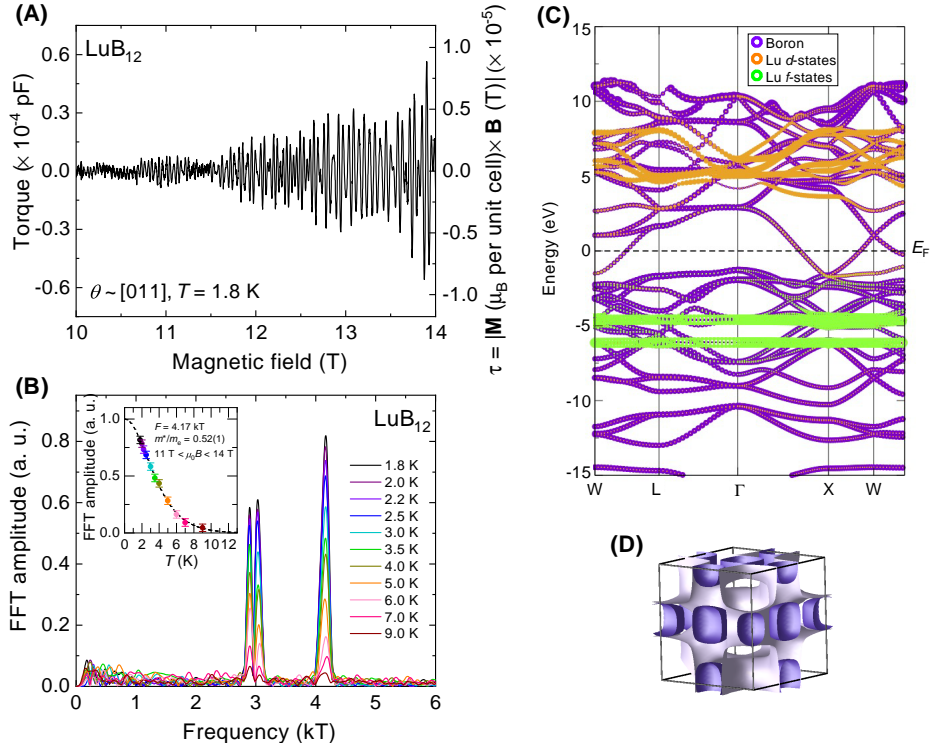


Fig. 4.16. Fermi surface of the non-magnetic metal LuB_{12} . (A) Magnetic torque measured by colleague Máté Hartstein on a single crystal of LuB_{12} at 1.8 K with the field applied along the $[110]$ high symmetry direction. (B) FFT of the torque quantum oscillations shown in (A), revealing multiple frequencies on the order of kT. The inset shows an LK temperature dependence fit of the 4.17 kT frequency, revealing an effective mass (m^*) of $0.52(1) m_e$. (C) Bandstructure of LuB_{12} calculated by collaborator Michelle Johannes, where purple circles correspond to boron bands, orange circles correspond to lutetium d -bands, and green circles correspond to lutetium f -bands. Dispersive boron bands can be seen to cross the Fermi energy. (D) Fermi surface corresponding to the bandstructure in (C), showing large pockets that correspond well to the measured high frequency quantum oscillations.

structure calculations show heavily hybridized boron and ytterbium f -states near the Fermi energy of YbB_{12} (Fig. 4.17A, B). If they were in a metal, these largely non-dispersive bands would be expected to yield heavy effective masses. To get a sense of what Fermi surface

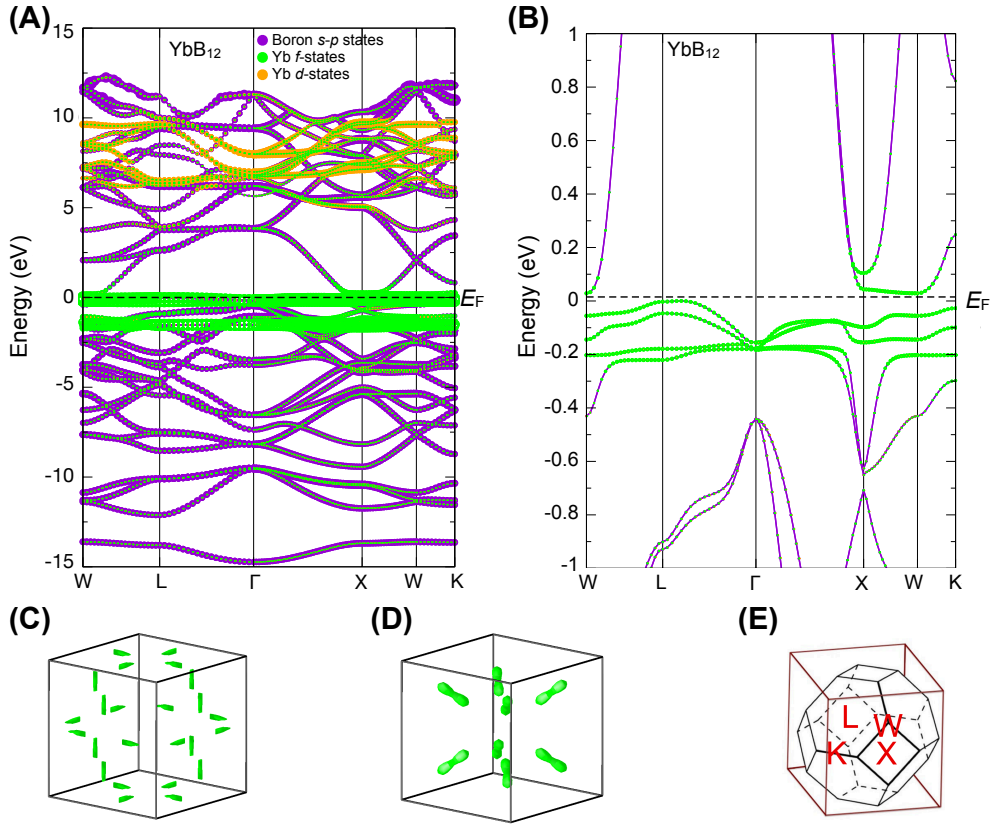


Fig. 4.17. Bandstructure calculation of YbB_{12} in the unconventional insulating phase. The calculated bandstructure of YbB_{12} shown over a wide energy range in (A) with an expanded view around the Fermi energy E_F in (B). Several characters are projected out of the eigenvectors at each k -point and the resulting weight is indicated by a circle of proportional size. Green circles correspond to Yb f -states, orange circles to Yb d -states, and violet circles to boron states. (C) Small needle-shaped Fermi surfaces of YbB_{12} obtained using the modified Becke-Johnson potential for a small positive energy shift. (D) small peanut-shaped Fermi surfaces of YbB_{12} obtained using the modified Becke-Johnson potential for a small negative energy shift. (E) A schematic of the conventional face-centred cubic Brillouin zone used for the band structures within the cubic Brillouin zone used for the Fermi surfaces. Calculations were performed by our collaborator Michelle Johannes [103].

we would expect to observe if the ground state of YbB_{12} were a metal, we shift the calculated energy by ± 0.7 meV such that the Fermi energy lies in the valence or the conduction bands. These energy shifts produce multiple electron and hole Fermi surface sections, shown

in Fig. 4.17C and D, which would correspond with multiple low quantum oscillation frequencies on the order of hundreds of T. The non-dispersive nature of the bands would also imply heavy quasiparticle effective masses of $\approx 6 m_e$ for the electron pockets and $\approx 9 m_e$ for the hole pockets [103]. These are comparable to the quantum oscillation frequencies and effective masses we observe in experiments. Although shifting the Fermi energy in the bandstructure calculation to simulate the Fermi surface that would arise from the valence and conduction bands of insulating YbB₁₂ can at best be considered a thought experiment, the exercise nevertheless suggests the insulating phase quantum oscillations reflect the material's bandstructure in a comparable way to conventional metallic quantum oscillations.

4.8 Comparison with quantum oscillations observed by independent research group

Concurrent to our group's progress on YbB₁₂, two papers have been published by an independent research group at the University of Michigan on quantum oscillations in the insulating and metallic phases of YbB₁₂ [88, 129]. While the experimental data presented by our group and the Michigan group are broadly consistent, there are key differences in our interpretation of the data. In this section, we will evaluate some of the differences in interpretation.

In the insulating phase of YbB₁₂, the two groups have reported highly similar results, with a crucial difference being that the Michigan group only observed one quantum oscillation frequency each in magnetic torque and electrical transport. Using the same capacitive torque and four-point contacted electrical transport technique as our group, the Michigan group reports a ≈ 700 T frequency for dHvA oscillations a ≈ 800 T frequency for SdH oscillations, with effective mass (m^*) of $6.6 m_e$ and $14.6 m_e$, respectively, for the applied field aligned along the [001] direction [88]. The frequencies reported by the Michigan group agree well with our values. Meanwhile, even though the Michigan group's effective mass for torque oscillations is also in agreement with our value, their effective mass for SdH oscillations is much higher than ours. This difference in effective mass could potentially be explained by

4. Unconventional insulating quantum oscillations in YbB_{12}

the fact that the Michigan group had access to a dilution refrigerator. The dilution fridge enabled access to temperatures down to ≈ 60 mK, about a fifth of the base temperature our group had access to using the ^3He cryostats in NHMFL in Tallahassee and HFML in Nijmegen. As such, it would be desirable to measure SdH oscillations on our YbB_{12} down to dilution fridge temperatures such that a like-for-like comparison could be made with the Michigan group's SdH data.

The fact that the Michigan group did not observe low frequency oscillations less than 500 T is more puzzling. One potential explanation for the appearance of low frequency oscillations is the inclusion of other phases of Yb-B compounds. This is unlikely on two fronts. First, elemental characterization performed using scanning electron microscopy and powder X-ray diffraction by our collaborating crystal growth group in Warwick University detected minimal off-stoichiometric phases. Further, YbB_6 , a neighboring phase in the Yb-B phase diagram [48], has a dHvA oscillation frequency of ≈ 400 T [88]. This frequency is distinct from the low frequency dHvA and SdH oscillations that we have observed (see Table 4.1). It is therefore difficult to explain this difference without further measurements, potentially involving a larger set of new samples so that a trend can be revealed.

In the field-induced metallic phase of YbB_{12} , the data between the two groups is largely in agreement, but the two groups have come to distinctly contrasting interpretations [129]. Fig. 4.18A shows an overlay of the quantum oscillations measured using PDO in the metallic phase of YbB_{12} by both groups. The peak and trough features generally correspond well between the two groups, with subtle but consistent differences in location which could potentially be explained by a difference in sample alignment during measurement. FFTs of the quantum oscillations measured by the two groups also show a similar overall profile. Differences in the exact frequencies observed could again potentially be explained by a difference in field alignment.

Despite the overall similarities in the observed quantum oscillations, the Michigan group has proposed that the quantum oscillations in the metallic phase consists of a single field-dependent frequency with field-dependent effective mass [129]. Such an interpretation was required since the measured complex quantum oscillation waveform could not be simulated

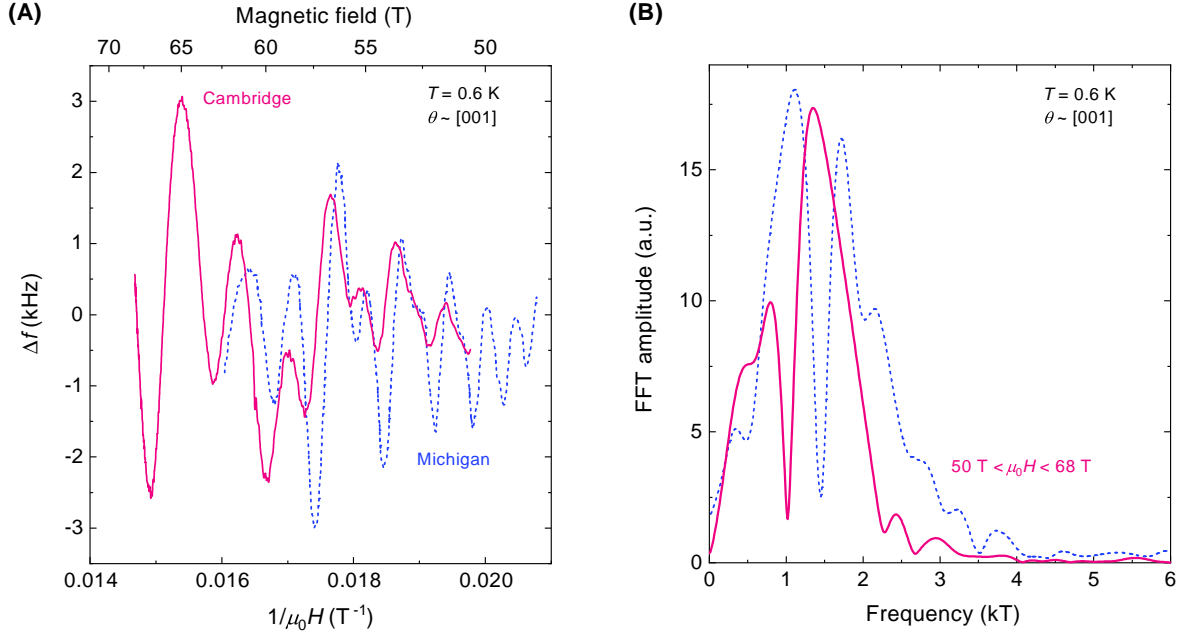


Fig. 4.18. Comparing quantum oscillations in metallic YbB_{12} with data from Michigan group. (A) Background subtracted quantum oscillations measured by PDO in the field-induced metallic phase of YbB_{12} by our (solid red line) group and the Michigan group (dashed blue line) [129]. The peak and trough features correspond well between the two groups, with subtle but consistent differences in location which could potentially be explained by a difference in sample alignment during measurement. (B) FFTs of the quantum oscillations in (A), showing a similar overall form of the frequency spectrum, with differences in the exact frequencies observed potentially explained by field alignment. The Michigan data in both (A) and (B) have been reproduced from Ref. [129].

with the three most prominent frequencies, at ≈ 1.1 kT, ≈ 1.7 kT, and ≈ 2.1 kT. As we have seen in this chapter, however, the observed complex quantum oscillation waveform in the field-induced metallic phase of YbB_{12} can be simulated when all frequencies in the FFT spectrum are taken into account. Indeed, the close correspondence in frequency and effective mass of the low frequency quantum oscillations across the insulating and metallic phases, shown in Table 4.1, could be naturally interpreted as an insulating phase Fermi

4. Unconventional insulating quantum oscillations in YbB_{12}

surface that mirrors the heavy fermion Fermi surface in the metallic phase. The appearance of multiple additional heavy Fermi surface sheets that follows from this approach would also correspond well with the steep increase in linear specific heat coefficient across the field-induced insulator-to-metal transition [97].

Chapter 5

Unconventional insulating quantum oscillations in FeSb₂

5.1 Introduction

First synthesized in 1959 [130], FeSb₂ is a *d*-electron correlated insulator that forms an orthorhombic crystal structure with lattice constants of $a = 5.83 \text{ \AA}$, $b = 6.53 \text{ \AA}$, and $c = 3.19 \text{ \AA}$, as shown in Fig. 5.4A [51, 131]. Two indirect gaps in electrical transport have been reported for FeSb₂, a larger gap of $\approx 14 \text{ meV}$ between $\approx 20\text{--}100 \text{ K}$, and a smaller gap of $\approx 6 \text{ meV}$ below [132, 133]. These are accompanied by a large direct gap of 130 meV revealed by optical conductivity measurements, thereby forming a multi-gap structure similar to SmB₆ and YbB₁₂ [134].

Unlike in SmB₆ and YbB₁₂, where electrical transport is isotropic, FeSb₂ shows significant anisotropy in its electrical properties. In addition to resistivity values that differ by orders of magnitude when the electrical current is applied along different crystal axes (Fig. 5.1A), several reports have found a metal-to-insulator transition in electrical transport when electric currents are applied along the crystal *b*-axis (Fig. 5.1B) [135–137]. The transition has been found to be sample dependent even within a single study, and, strangely, a corresponding

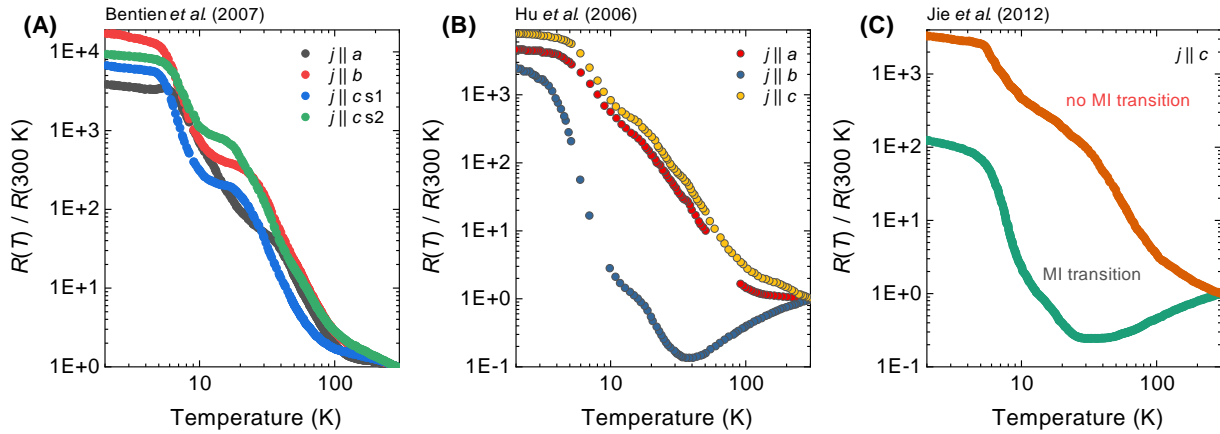


Fig. 5.1. Anisotropic electrical transport in FeSb₂. Electrical transport of FeSb₂ from three separate reports, shown as the temperature dependent resistivity as a function of the resistivity at 300 K for ease of comparison. Significant anisotropy can be seen when the electric current is aligned along different crystal axes. **(A)** Electrical transport reported by Ref. [140], showing insulating behavior along all three crystal axes. Features in the resistivity background, such as the intermediate and low temperature plateaux, appear at different temperatures for different current alignment. **(B)** Electrical transport reported by Ref. [137], where a metal-to-insulator transition is revealed when the electric current is applied along the crystal *b*-axis. **(C)** Electrical transport reported by Ref. [139], where a metal-to-insulator transition has been observed on certain samples when the electric current is applied along the crystal *c*-axis.

transition was not observed in optical conductivity [135]. The transition has therefore been attributed to impurity conduction channels, which could arise in flux grown samples like the ones used in these studies from excess Sb inclusion [138]. A metal-to-insulator transition in electrical transport when current is applied along the crystal *c*-axis has also been reported; however, such a transition is even more elusive than the *b*-axis transition, as it has only been reported by one study (Fig. 5.1C) [139].

At low temperatures, FeSb₂ exhibits a nonmagnetic ground state, with no magnetic ordering observed by early Mossbauer measurements [141], and no evidence for localized magnetic moments on the Fe atoms from recent neutron scattering measurements [142].

Accordingly, FeSb₂ exhibits small magnetic susceptibility at low temperatures, but the sign of the susceptibility appears sample dependent. Small paramagnetic susceptibility has been recorded along the *a*- and *b*-axes on certain flux grown samples (Fig. 5.2A and B) [137, 138, 143], while other flux grown samples show diamagnetism along all crystal axes at low temperatures (Fig. 5.2C) [136]. The samples which are diamagnetic at low temperatures exhibit a crossover into paramagnetism at ~ 100 K, which has been suggested to be the result of thermally induced changes in bond angle affecting the strength of orbital mixing [16]. Indeed, several structural anomalies have been observed in this temperature range. The shear modulus, which typically softens with increasing temperature, exhibits an unusual hardening in FeSb₂ at ≈ 100 K [144]. Optical conductivity also reveals several lattice vibration modes that are not expected from group theory, which undergo changes below ≈ 100 K [135]. The concurrent appearance of these structural changes and the evolution into paramagnetism suggests a correlation between the electronic and lattice degrees of freedom in FeSb₂ [144].

In the past two decades, FeSb₂ has gathered much attention for its colossal Seebeck coefficient S , which reaches as high as ≈ -45 mV K⁻¹ at low temperatures, corresponding to a power factor [S^2/ρ , where ρ is electrical resistivity] of ≈ 2.3 mW K⁻² (Fig. 5.3) [140]. Although these numbers are higher than commercial Bi₂Te₃-based thermoelectric materials, the figure of merit [$S^2T/\rho\kappa$, where κ is thermal conductivity] for FeSb₂ is low due to the high thermal conductivity at low temperatures. Since thermal conductivity consists largely of lattice contributions in the temperature range where the thermopower peaks, the low figure of merit limits the commercial prospect of FeSb₂ as a thermoelectric material [140].

Despite the limited commercial prospects, FeSb₂ raises an interesting question regarding the origin of the large Seebeck coefficient. Indeed, although Seebeck coefficients up to ~ -10 mV K⁻¹ have been independently reported, the very high Seebeck coefficient of ≈ -45 mV K⁻¹ has yet to be reproduced [145, 146]. In order to understand the highly sample dependent thermopower, and potentially find a path towards better thermoelectric materials, the research community has been engaged in a lively discussion on whether the large Seebeck coefficient arises from electron-electron correlations or electron-phonon interactions.

A number of arguments have been put forth for an electron correlation origin of the

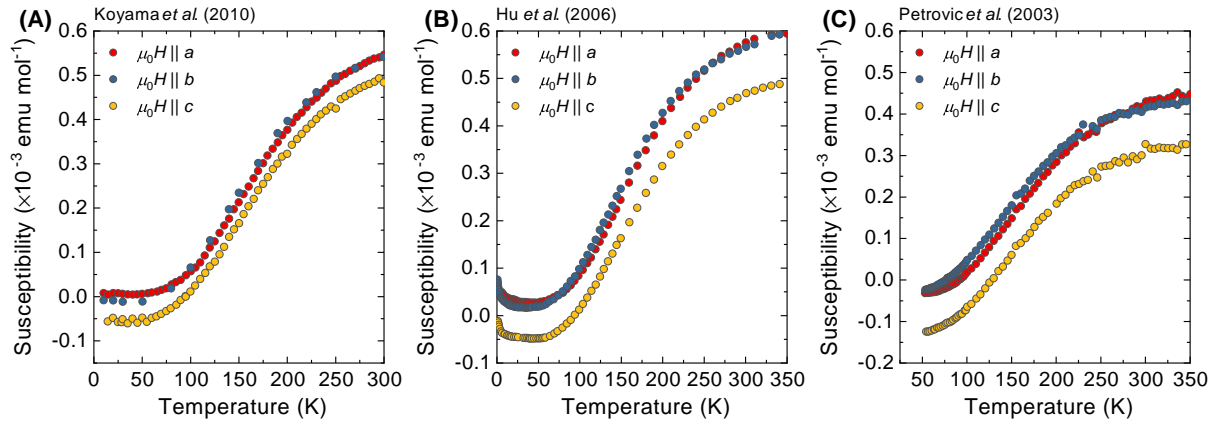


Fig. 5.2. Anisotropic magnetic susceptibility in FeSb₂. Magnetic susceptibility of FeSb₂ from three separate reports, showing an anisotropy when the external magnetic field is applied along different crystal axes. **(A)** Magnetic susceptibility reported by Ref. [143], showing diamagnetic response when the field is applied along the *b*- and *c*-axes but paramagnetic response when the field is applied along *a*-axis. **(B)** Magnetic susceptibility reported by Ref. [137], showing diamagnetic response only when the field is applied along the *c*-axis and paramagnetic response otherwise. **(C)** Magnetic susceptibility reported by Ref. [136], showing diamagnetic response for all field alignments.

colossal Seebeck coefficient in FeSb₂, which mostly involve comparing electrical and thermal properties. In the original report of the colossal Seebeck coefficient, it was noted that the magnitude of the peak in the Seebeck coefficient varies for samples with similar thermal conductivity, which predominantly arises from phonon contributions in the temperature range where the peak in thermopower is observed [140]. This would suggest that phonons are not the main contributor to the large thermopower. Indeed, comparing the Seebeck coefficient of FeSb₂ to the isostructural but weakly correlated homologues of FeAs₂ and RuSb₂, FeSb₂ exhibits a thermopower peak that is approximately an order of magnitude higher, despite similar thermal conductivity between the three materials [50]. It has also been reported that the temperature profile of the Nernst effect resembles the temperature profile of magnetoresistance, rather than that of thermal conductivity, which suggests a correlation between electronic and thermal properties [133]. Additionally, while a metal-to-

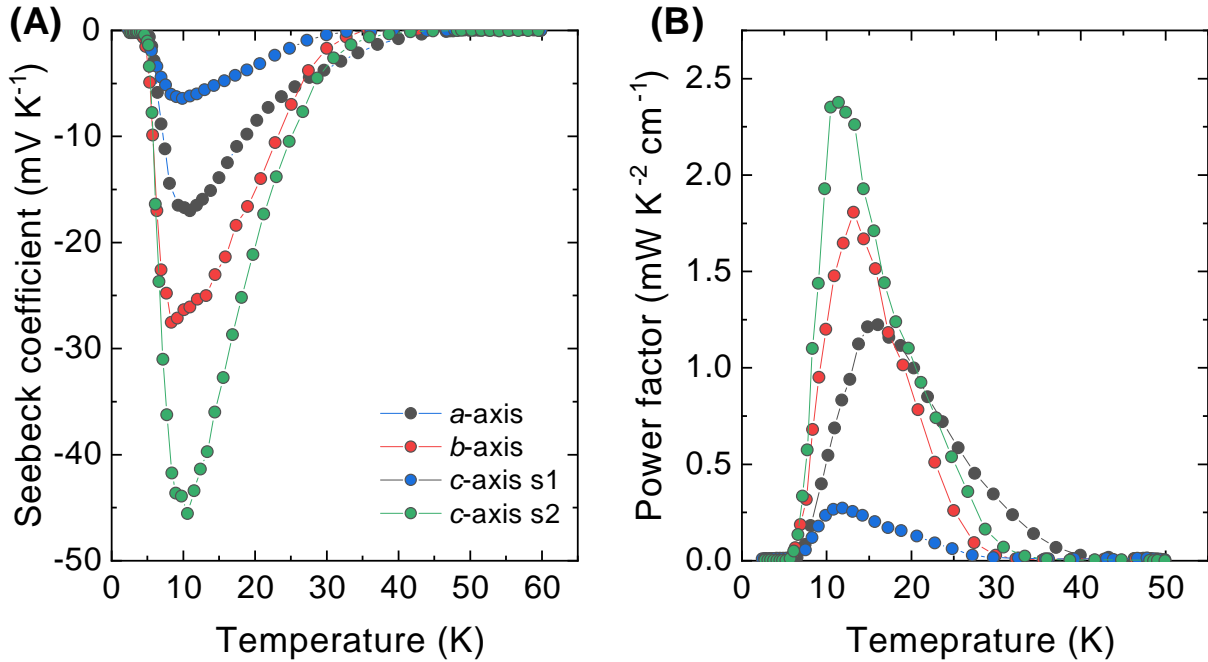


Fig. 5.3. Colossal Seebeck coefficient in FeSb₂. (A) A colossal Seebeck coefficient that reaches as high as ≈ -45 mV K⁻¹ has been reported in FeSb₂, raising the material's prospect for use in thermoelectric devices [140]. (B) The high power factor of ≈ 2.3 mW K⁻² observed in FeSb₂ is higher than those for commercial Bi₂Te₃-based thermoelectric materials, but a low figure of merit due to high lattice thermal conductivity limits the viability of FeSb₂ in commercial applications.

insulator transition in electrical transport along the crystal *c*-axis has yet to be reproduced, it has been reported that the steepness of this transition correlates with the magnitude of the thermopower peak, another link between electronic and thermal properties [139].

Strong evidence has also been reported for a phonon drag origin of the colossal Seebeck coefficient. Prior to the discovery of the colossal Seebeck coefficient, it was reported that optical conductivity measurements reveal a change in the phonon modes as the energy gap opens at ≈ 70 K, suggesting a coupling between electron and lattice degrees of freedom [17]. Indeed, while the shape of the thermopower can be modeled with calculations

involving the electronic structure of FeSb₂, the calculations are unable to reproduce the magnitude of the thermopower, suggesting other contributions such as phonon drag play a role [139, 144, 145]. Recently, studies correlating the magnitude of the Seebeck coefficient with sample size have also shown support for phonon drag. The Seebeck coefficient has been reported to increase with increasing sample size, whereas resistivity remains independent of sample dimensions [147]. It has also been found that the thermopower is much smaller in polycrystalline samples of FeSb₂ compared to single crystals [131]. Such a dependence on sample size and single-crystallinity could be explained by a reduction in phonon mean free path. Furthermore, a large effective mass on the order of 5 m_e observed from cyclotron resonance, attributed to low carrier mobility, would also suggest that the large thermopower arises from phonons [147].

As we can see, the quest to pin down the origin of the large Seebeck coefficient in FeSb₂, and therefore find ways to engineer better thermoelectric materials, is still underway. In the midst of this, we have approached FeSb₂ for a different reason – that the small gap, nonmagnetic, low temperature ground state of the material may be partial to insulating quantum oscillations. Indeed, optical conductivity measurements have revealed some non-vibrational spectral weight survive inside the gap at low temperatures, pointing to the possible existence of in-gap states that have been proposed for insulating quantum oscillations in SmB₆ and YbB₁₂ [17]. FeSb₂ has also recently been found to host potentially topological surface conduction states, drawing a further parallel to SmB₆ and YbB₁₂ [19, 148].

As it turned out, FeSb₂ indeed exhibits magnetic torque quantum oscillations at low temperatures, allowing us to add a third member to the group of unconventional quantum oscillatory insulators. In addition to expanding the group with the first d -electron insulator, the discovery in FeSb₂ is particularly significant because it reveals a novel metamagnetic transition within the unconventional insulating phase that accompanies an enhancement in quantum oscillation amplitude and frequency spectrum. The discovery of a metamagnetic transition that couples to insulating quantum oscillations provides important clues for the mechanism that underlies unconventional Fermi surfaces.

5.2 Sample characterization

For high magnetic field quantum oscillation measurements, we used single crystals grown with the chemical vapour transport (CVT) technique by Ke-Jun Xu from Prof. Zhi-Xun Shen’s group at Stanford University (see Chapter 3 for details). The CVT technique, following the work in Ref. [50], avoids extraneous flux inclusion and minimizes impurity and disorder introduced by high temperature growth methods [149–151]. In addition to elemental analysis conducted in Stanford, we have performed additional characterization measurements in the UK. To confirm the high quality of these CVT samples, we worked with Exeter Analytical UK Ltd., an external company, to scan for inclusions across a broad range of elements using ion-coupled plasma optical emission spectroscopy (ICP-OES). Table 5.1 shows the results of the ICP-OES measurement, which rules out the majority of impurity elements to within the instrument detection limit of 10 parts per million (ppm), with the highest impurity concentration of a still very low < 100 ppm for Sulphur. Similarly, energy-dispersive X-ray spectroscopy performed by S. M. Fairclough in the Department of Materials Science and Metallurgy in Cambridge and Raman spectroscopy performed by R. T. Phillips in the AMOP group in the Physics Department in Cambridge collectively provide further evidence of the high sample quality [152].

Electrical resistance characterization, similar to those performed on YbB_{12} , provides more evidence of high sample quality. Fig. 5.4B shows the inverse resistance ratios [$i\text{RRR} \equiv R(T = 2 \text{ K})/R(T = 300 \text{ K})$, where R is the measured resistance and T is the temperature] measured at ambient magnetic fields with the applied electric current \mathbf{j} aligned along the [001] direction on the single crystal FeSb_2 samples that showed quantum oscillations. An electrical activation gap of ≈ 14 meV is observed, as well as $i\text{RRR}$ values of the order 10^6 , an order of magnitude higher than in previous reports. Similar to the case for YbB_{12} , high $i\text{RRR}$ values are an indication of high sample quality in FeSb_2 [54, 138]. The activation gap is seen to persist up to applied magnetic fields of at least 55 T, as evidenced by the electrical resistance measurements in pulsed magnetic fields shown in Fig. 5.4C.

Intermediate field magnetic susceptibility measurements, performed by colleague Alexan-

Concentration (parts per million)	Elements
< 10	Ag, Al, As, B, Ba, Be, Ca, Cd, Co, Cu, Dy, Er, Eu, Hg, Ho, In, Ir, K, La, Li, Lu, Mg, Mn, Mo, Na, Nb, Ni, Os, Pb, Rb, Re, Ru, Sc, Se, Si, Sn, Sr, Tb, Ti, Tm, V, Y, Yb, Zn, Zr
< 20	Au, Ga, Ge, Hf, Pr, Rh, Sm, Tl
< 30	Bi, Nd, P, Pd, Pt
< 40	W
< 50	Ce
50-100	S
> 100	None

Table 5.1. Chemical impurity analysis through mass spectroscopy. Chemical impurity analysis using ion coupled plasma optical emission spectroscopy performed on samples from the same growth batches as those used in quantum oscillation measurements. The extremely low impurity content, with no impurities detected above 100 parts per million, is evidence of very high sample quality.

der J. Hickey in the Quantum Design Inc. MPMS, provide further evidence of ultra low impurity levels. Fig. 5.5A shows measured magnetic susceptibility against temperature at constant applied magnetic field, measured upon warming after zero-field cooling. The low value of magnetic susceptibility and the agreement between the two measurements at applied fields of 0.05 T and 7 T indicate a non-magnetic ground state. The small low-temperature tail measured at a low applied field of 0.05 T also qualitatively suggests low impurity content [138]. Indeed, a Langevin fit to the magnetization as a function of applied magnetic field, shown in Fig. 5.5B, yields a magnetic impurity content of 60(20) ppm (see Appendix C for the fit procedure) [152]. Pulsed magnetic field measurements up to an applied field of 60 T using a collection of samples to maximize signal size show magnetization scaling linearly to the highest measured fields (Fig. 5.5B inset).

Ambient field heat capacity measurements reveal a small yet finite linear coefficient. Fig. 5.5C shows the specific heat capacity of a single crystal FeSb₂ down to $T = 0.75$ K

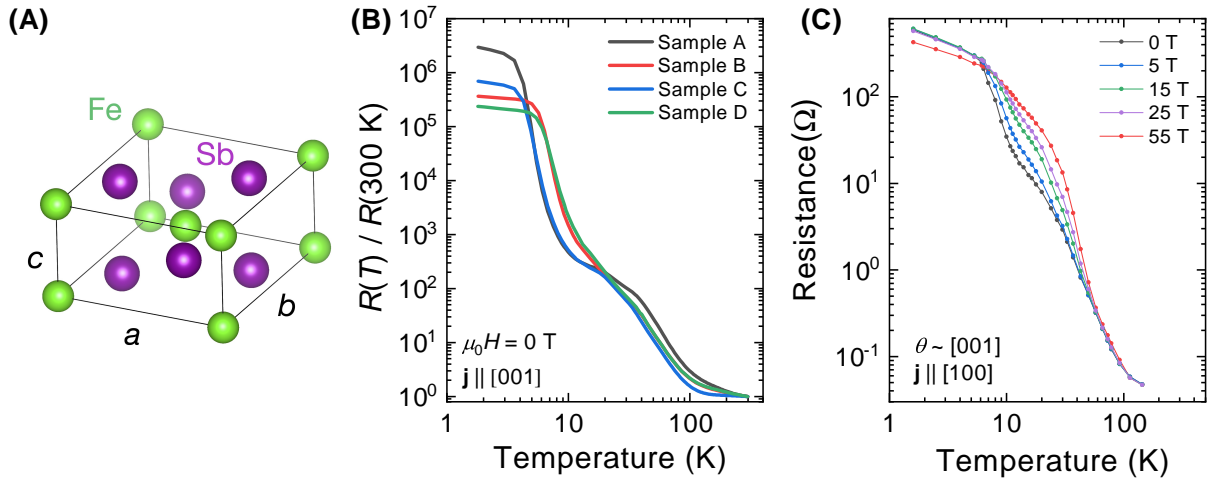


Fig. 5.4. Electrical properties of FeSb_2 . (A) A schematic diagram of the FeSb_2 unit cell. The lattice constants are $a = 5.83 \text{ \AA}$, $b = 6.53 \text{ \AA}$, and $c = 3.19 \text{ \AA}$, where a is measured along $[100]$, b is measured along $[010]$, and c is measured along $[001]$. (B) Measured inverse residual resistance ratio [$\text{iRRR} \equiv R(T = 2 \text{ K})/R(T = 300 \text{ K})$, where R is the measured resistance and T is temperature] of FeSb_2 samples that have shown quantum oscillations. Resistance measurements were performed using a Quantum Design Inc. PPMS in ambient magnetic field with the applied current \mathbf{j} aligned along the $[001]$ axis. The highest observed iRRR of the order 10^6 is an order of magnitude higher than in previous reports, signifying very high sample quality [54, 138]. The thermally activated indirect bandgap of $\approx 14 \text{ meV}$ is seen for the temperature range 20–100 K, as well as a lower temperature upturn below $\approx 10 \text{ K}$. (C) Electrical resistance as a function of applied magnetic field up to 55 T measured on a different sample than (B), with the electrical current \mathbf{j} applied along the $[100]$ axis and the applied magnetic field aligned along the $[001]$ axis. Electrically insulating behavior was observed to persist to the highest applied fields. The different current alignment compared to the measurements in (B) is the result of the geometry of the cut sample, which was produced by making a single, short cut on an as-grown crystal. The small cut sample was made to minimize self-heating in the pulsed field measurements.

measured at ambient magnetic fields by our collaborator S. Yamashita at Osaka University. A linear fit to the lowest temperature region of the data reveals a small residual linear coefficient $\gamma = 0.20(1) \text{ mJ mol}^{-1} \text{ K}^{-2}$. While this contrasts the behavior in SmB_6 and YbB_{12} , both of which exhibit sizable finite linear coefficients at low temperatures [12, 103],

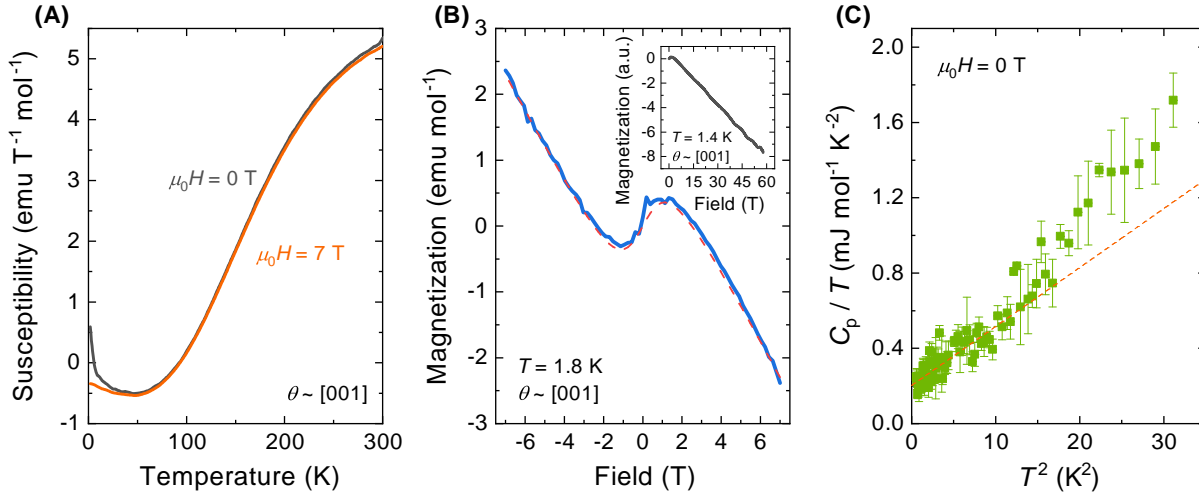


Fig. 5.5. Magnetic properties and specific heat capacity of FeSb₂. (A) Magnetic susceptibility of a single crystal of FeSb₂ as a function of temperature at constant magnetic fields of 0.05 T and 7 T measured upon warming after zero-field cooling, with the applied magnetic field aligned along the [001] axis. The small value of magnetic susceptibility and the overlap between measurements at applied fields of 0.05 T and 7 T suggest a non-magnetic ground state. (B) Measured magnetization of a single crystal of FeSb₂ as a function of applied magnetic field at a constant temperature of 1.8 K. The applied magnetic field was aligned close to the [001] axis. A Langevin fit, shown by the red dashed line, yields a magnetic impurity content of 60(20) parts per million, with an effective magnetic moment of 5.4(3) μ_B (see Appendix C for fit procedure). (Inset) Measured magnetization of a collection of single crystal FeSb₂ samples aligned close to the [001] axis up to an applied magnetic field of 60 T at a temperature of 1.4 K, showing no magnetic transition in the linear magnetization down to the detection limit. In light of the discovery of a metamagnetic transition in anisotropic magnetization, a detailed, high precision study should be conducted to search for a corresponding transition in linear magnetization. (C) Specific heat capacity measured in ambient magnetic field down to a temperature of 0.75 K. A linear fit to the lowest temperature region, shown by the red dashed line, yields a small residual linear coefficient $\gamma = 0.20(1)$ mJ mol⁻¹ K⁻².

this distinction could reflect the fact that large amplitude quantum oscillations only appear at high applied magnetic fields in FeSb₂. Specific heat capacity measurements down to low temperatures in high magnetic fields is therefore urgently needed going forward.

When selecting samples for high magnetic field quantum oscillation measurements, we choose samples with clean Laue patterns, high iRRR, and appropriately sized for our cantilevers, roughly $1 \times 1 \times 1$ mm³. Since CVT grown FeSb₂ single crystals tend to be small, the latter criterion usually amounts to selecting the largest available samples. While iRRR is not a perfect predictor of quantum oscillations, our group's work on SmB₆ and YbB₁₂ suggests that samples with high iRRR are more likely to show large amplitude quantum oscillations.

5.3 Magnetic torque quantum oscillations in FeSb₂

Following the *f*-electron Kondo insulators SmB₆ [11] and YbB₁₂ [103], we discovered bulk quantum oscillations in the magnetic torque of FeSb₂, the first *d*-electron correlated insulator to exhibit unconventional insulating quantum oscillations. Fig. 5.6A shows magnetic torque quantum oscillations measured on a single crystal of FeSb₂ at a temperature of 0.4 K up to the highest available DC fields of 45 T, with the magnetic field aligned 16° from the [001] crystallographic direction towards the vector normal to the (110) plane. Background subtraction was performed using the LOESS method, described in Chapter 3, with this particular background shown in Fig. 3.19B. The background subtracted quantum oscillations exhibit a complicated waveform, which would be expected when multiple high frequency oscillations are superimposed. When the measured oscillations are plotted in inverse field, as shown in Fig. 5.6B for the highest measured field range, visual peak counting confirms the periodicity of an ≈ 7 kT frequency. A Fast Fourier Transform of the background subtracted quantum oscillations shown in Fig. 5.6C indeed reveals multiple high frequencies on the order of kT, significantly higher than the quantum oscillations in the insulating phase of YbB₁₂ discussed in the previous chapter.

As with previous examples of insulating phase quantum oscillations, it is important to ascertain that the quantum oscillations observed at high fields in FeSb₂ are intrinsic to the insulating phase. As previously shown in Fig. 5.4C, we have found that the energy gap in FeSb₂ determined from contacted electrical transport remains relatively unchanged, if not slightly increases, up to applied magnetic fields of 55 T. In addition to pulsed field mea-

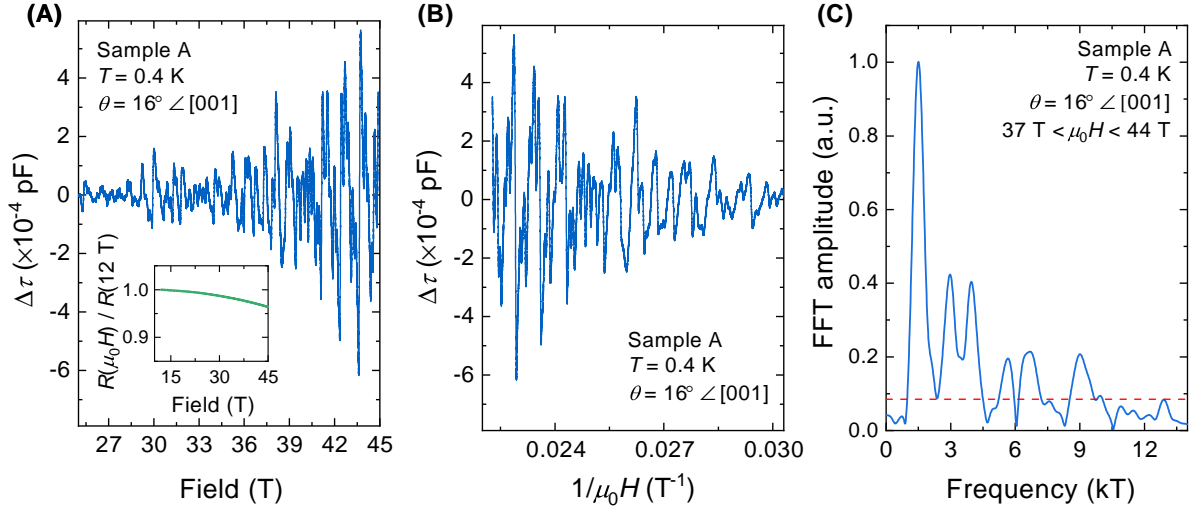


Fig. 5.6. dHvA oscillations in insulating FeSb₂. (A) Quantum oscillations in the magnetic torque expressed as changes in torque $\Delta\tau$ measured on a single crystal of FeSb₂ after LOESS background subtraction. The measurement was performed at a temperature of 0.4 K, with a magnetic field tilt angle $\theta = 16^\circ$ from the [001] crystallographic direction in the rotation plane spanning the [001] axis and the vector normal to the (110) plane. (Inset) Measured electrical resistance at the same angle as the main panel, with the applied electric current aligned along the [100] axis. Minimal negative magnetoresistance was observed in the field range where prominent quantum oscillations are visible (B) Background subtracted quantum oscillations in the highest measured field range of 33–45 T plotted as a function of inverse field, where the periodicity of the ≈ 7 kT frequency can be seen from peak counting. (C) Fast Fourier Transforms of the background subtracted quantum oscillations shown in (B) for the field range between 37–44 T, revealing multiple quantum oscillation frequencies up to ≈ 9 kT.

surements, we have also measured the magnetoresistance of FeSb₂ at 0.4 K simultaneously to the torque measurements in Fig. 5.6. As shown in the inset to Fig. 5.6A, at the same magnetic field tilt angle of 16° , the resistance of FeSb₂ was found to decrease by less than 5% between 12 T and 45 T. Taken together, the magnetoresistance measurements in DC and pulsed fields provide useful evidence that FeSb₂ remains robustly insulating in the field range where large amplitude torque quantum oscillations were observed.

To determine whether quantum oscillations are intrinsic to the bulk of FeSb₂, we calculate the absolute amplitude of the quantum oscillations in units of μ_B per unit cell. The experimentally measured quantum oscillation amplitude for the dominant ≈ 1450 T frequency at an applied field of 42 T is on the order of $10^{-4} \mu_B$ per unit cell. This compares favorably with an expected amplitude in the range of 10^{-5} to $10^{-3} \mu_B$ per unit cell from the LK formula with contributions from the entire bulk of the sample. Details of these calculations can be found in Appendix A. If we consider only a surface layer contribution, the magnetization per unit cell would be 10^4 times larger, which would be difficult to explain in the nonmagnetic ground state of FeSb₂. Since our FeSb₂ samples exhibit impurity concentrations of less than 100 parts per million (Table 5.1), the above absolute amplitude comparison also shows that the observed quantum oscillations are highly unlikely to originate from impurity inclusions.

The observed high frequencies serve as another evidence that quantum oscillations arise intrinsically from the bulk of FeSb₂. As shown in Fig. 5.6C, quantum oscillation frequencies up to the order of 9 kT are revealed at the highest applied magnetic fields above 40 T. Such a high frequency corresponds to quasiparticle orbits encompassing an area of approximately 20% of the first Brillouin Zone. Such a large orbit would not be expected from spatially separated impurity inclusions or interstitial metallic patches. It is also unlikely to arise from surface layers, since large surface orbits would only be expected within a narrow field tilt range where the field is near perpendicular to flat sample surfaces.

An additional evidence for the intrinsic nature of the quantum oscillations comes from comparing multiple samples that show quantum oscillations. When this thesis was initially drafted, our group had observed magnetic torque quantum oscillations in a total of four FeSb₂ samples (additional quantum oscillations presented in Fig. 5.9A and Fig. 5.10C). As shown in Table 5.2, we have found a correspondence between the highest oscillation frequencies with sample quality as inferred from iRRR. Later measurements performed by colleagues Alexander G. Eaton and Alexander J. Hickey further reinforce this trend, where two additional samples with iRRR of $\approx 900k$ exhibited quantum oscillation frequencies on the order of 3 kT up to applied fields of 35 T. If quantum oscillations were to arise from impurity inclusions or metallic patches, we would expect lower quality samples to show larger amplitude, higher frequency oscillations. Since our measurements show the opposite of this

5. Unconventional insulating quantum oscillations in FeSb₂

Sample	Inverse residual resistivity ratio (iRRR) $R(T = 2 \text{ K}) / R(T = 300 \text{ K})$	Highest observed quantum oscillation frequency below $\mu_0 H = 35 \text{ T}$ (kT)	Maximum applied magnetic field (T)
A	2,954,000	9.0	45
B	366,000	1.9	35
C	692,000	2.0	35
D	238,000	2.1	35

Table 5.2. List of iRRR and maximum observed quantum oscillation frequency for all measured samples. Four samples were measured to high fields, each of which exhibited quantum oscillations in the magnetic torque. A clear correspondence between the richness of a sample’s frequency spectrum and the value of its inverse residual resistivity ratio is apparent, with the high quantum oscillation frequencies observed in sample A corresponding to by far the largest recorded iRRR value. The electrical resistance measurements were performed with the applied current aligned along the [001] direction.

trend, and multiple experiments at different high field facilities using different samples from different growth batches consistently reveal high frequency quantum oscillations, we can be confident that the observed quantum oscillations are intrinsic to the insulating phase of FeSb₂.

5.4 Novel metamagnetic transition accompanied by enhanced quantum oscillations

Quantum oscillations in FeSb_2 exhibit an unusual coupling to a sharp change in the slope of the magnetic torque background (Fig. 5.7A). This change in torque background slope is accompanied by a prominent hysteresis loop between rising and falling magnetic field sweeps. As shown in Fig. 5.7B, for a magnetic field tilt angle of approximately 14° from the [001] crystallographic direction towards the vector normal to the (110) plane, a sharp slope change occurs at approximately 27 T during the rising field sweep, but only occurs at approximately 20 T during the falling field sweep, and does not fully rejoin the rising field sweep until below 5 T.

The sharp change in the slope of the torque background is similar to metamagnetism, a term initially used to describe systems that undergo a first-order transition from a low magnetization and low susceptibility state to a high magnetization and low susceptibility state upon the application of external magnetic fields at low temperatures [153]. A classic example of a metamagnetic transition can be found in FeCl_2 , which transitions from an antiferromagnetic phase to a paramagnetic phase [154]. At an applied field of 1.06 T, the magnetization of FeCl_2 exhibits a step-like increase, and opens up a hysteresis loop when the applied field is removed (Fig. 5.8). The first order transition in the magnetization results from strong magnetic anisotropy, which restricts spins to reversals along the easy axis rather than free rotations in space [155]. While the magnetic phases on either side of the transition can vary, the step-like increase in magnetization and opening of a hysteresis loop are signatures of metamagnetic transitions.

More recently, the term metamagnetism has been used more loosely to refer to features in a material's magnetization. An example relevant to this thesis is YbB_{12} , where both the insulator-to-metal transition at ≈ 47 T, which results in a slope-change in magnetization, and a separate magnetization slope-change at ≈ 102 T have been referred to as metamagnetic transitions [99]. While the magnetization of YbB_{12} changes slope at both transitions, it does not show a sharp, step-like increase similar to that in FeCl_2 . Existing reports of the

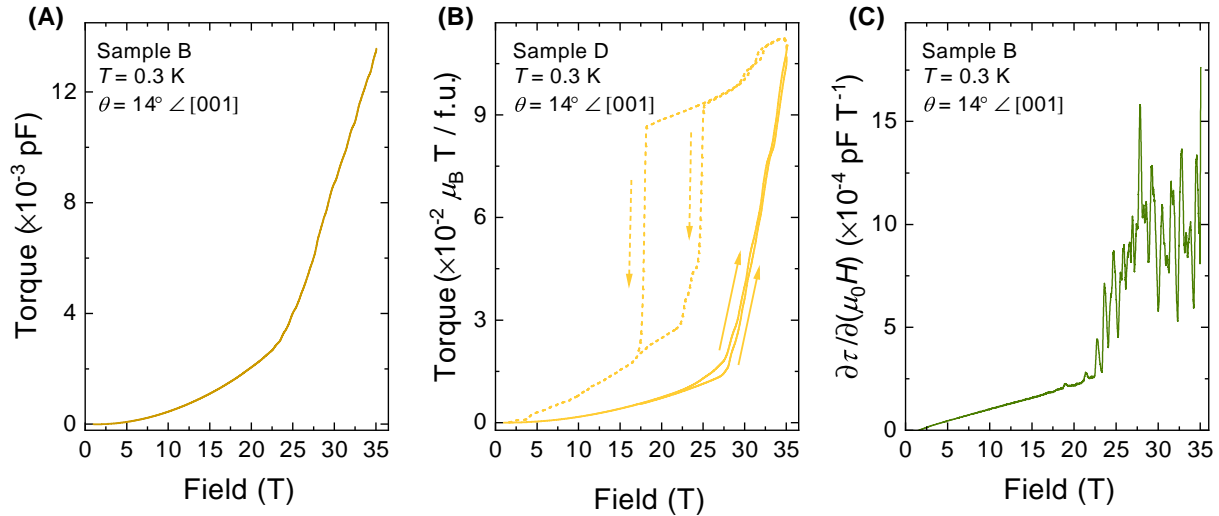


Fig. 5.7. Novel metamagnetic transition manifesting as a sharp slope change in the magnetic torque background. (A) Magnetic torque background measured on a single crystal of FeSb₂ exhibiting a sharp change in slope above ≈ 25 T. The sample was aligned to rotate between the [001] axis and the vector normal to the (110) plane. (B) Magnetic torque measured as a function of applied magnetic field at a fixed tilt angle for successive magnetic field sweeps. Arrows indicate the direction in which the magnetic field was swept; the solid (dashed) line corresponds to increasing (decreasing) magnetic field sweep. (C) Derivative of the magnetic torque in (A) with respect to applied magnetic field. Quantum oscillations above the slope change in the torque background is visible even prior to background subtraction.

two transitions in YbB₁₂ also do not show hysteresis loops, except for a small loop around the insulator-to-metal transition field that most likely results from sample self-heating in pulsed fields [69]. Considering that cubic YbB₁₂ does not show strong anisotropy between its crystal axes, features in its magnetization are unlikely to result from spin reversals. The term metamagnetic transition in the context of YbB₁₂ is therefore used to refer generally to sharp features in magnetization. It is in this broader sense of the term that we will refer to the sharp change in the slope of torque magnetization in FeSb₂ as a metamagnetic transition.

The slope change in the magnetic torque of FeSb₂ satisfies most of the original criteria

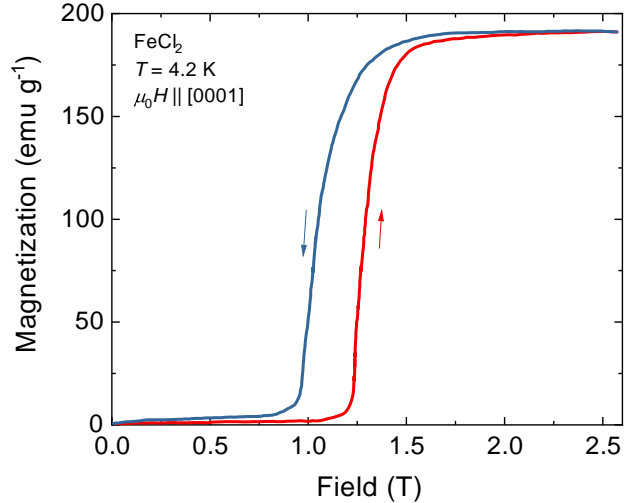


Fig. 5.8. Metamagnetic transition in FeCl_2 . Metamagnetic transition in FeCl_2 reported by Ref. [154]. The transition is characterized by a step-like increase in magnetization and hysteresis loop between rising and falling field sweeps.

for a metamagnetic transition. As seen in Fig. 5.7B, a large hysteresis loop accompanies the torque background slope change. Since torque is the cross product of magnetization and magnetic field, we can get a sense of the anisotropic magnetization by taking the derivative of torque as a function of field. While the large quantum oscillations somewhat obscure the background, we can see the derivative of magnetic torque undergoing a step-like increase in Fig. 5.7C. The step-like increase in anisotropic magnetization and hysteresis loop could be the result of spin-flips along an easy axis, since strong anisotropy has been reported in FeSb_2 (Fig. 5.4 and Fig. 5.5). Additionally, calculations performed by our collaborator Michelle Johannes suggests that FeSb_2 borders collective magnetic phases [152]. The calculations show that the gapped nonmagnetic ground state is metastable towards metallic ferromagnetism in an applied magnetic field, in agreement with previous theoretical studies [156, 157]. Further preliminary calculations suggest that other collective magnetic phases such as antiferromagnetism, ferrimagnetism, or other forms of textured magnetism may be even lower in energy. The step-like increase in torque derivative, sizable hysteresis loop, strong anisotropy in electronic and magnetic properties, and the expected proximity to magnetically ordered phases

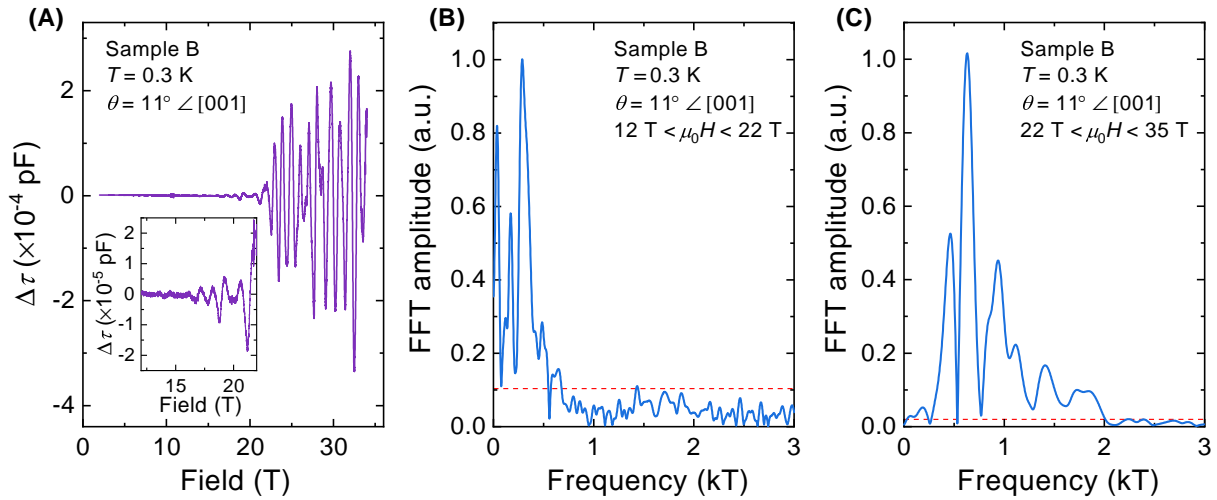


Fig. 5.9. Evolution of magnetic quantum oscillation across a novel metamagnetic transition. (A) Large amplitude quantum oscillations above the sharp slope change shown in Fig. 5.7A revealed after LOESS background subtraction. (Inset) Background subtracted magnetic torque at low fields showing quantum oscillations start below the novel metamagnetic transition (B and C) FFTs of the background subtracted quantum oscillations below and above the magnetic torque background slope change, as shown in (A) and the inset to (A). A marked increase of the quantum oscillation frequency spectrum is observed across the metamagnetic transition.

together show good evidence that FeSb₂ is likely to undergo a metamagnetic transition.

Despite the similarities, further investigations are required to clarify the exact nature of the slope change in the magnetic torque of FeSb₂. Metamagnetic transitions typically refer to features in direct magnetization, rather than anisotropic magnetization as measured by torque magnetometry. High accuracy measurements of direct magnetization, for instance through force magnetometry or extraction magnetometry, and local magnetism measurements are still required at high fields on FeSb₂. We therefore tentatively refer to the sharp slope change in the magnetic torque of FeSb₂ as a metamagnetic transition on account of their similarities, but leave open the possibility for this designation to be amended by future research.

The most striking aspect of the novel metamagnetic transition in FeSb₂ is the significant enhancement in quantum oscillation amplitude and frequencies upon crossing the transition. Fig. 5.7C shows the derivative of the torque background in Fig. 5.7A, where large amplitude quantum oscillations are visible even prior to background subtraction. Fig. 5.9A shows quantum oscillations revealed after LOESS background subtraction on the field sweep shown in Fig. 5.7A. Corroborating the torque derivative in Fig. 5.7C, the background subtraction shows large amplitude oscillations appearing above the novel metamagnetic transition. The inset to Fig. 5.7A shows background subtracted torque signal below the novel metamagnetic transition, where smaller amplitude oscillations can be seen. As FFTs of the background subtracted quantum oscillations show, the dominant oscillation frequency increases from $\lesssim 400$ T to $\gtrsim 400$ T across the metamagnetic transition, and high frequencies > 1 kT become visible (Fig. 5.9B and C).

The metamagnetic transition in FeSb₂ appears sensitive to magnetic field orientation. Fig. 5.10A shows magnetic torque background as a function of magnetic field tilt angle, measured from the [001] crystallographic direction towards the vector normal to the (110) plane. For this sample, the lowest applied magnetic field at which the metamagnetic transition occurs is approximately 27 T at a tilt angle of 14°. The transition rapidly rises to higher applied magnetic fields beyond 35 T within a few degrees of rotation in either direction. The derivative of the magnetic torque background in Fig. 5.10B, as well as their corresponding background subtracted quantum oscillations in Fig. 5.10C, show that the onset of prominent quantum oscillations exhibit a similarly rapid evolution with tilt angles.

5.5 Non-Lifshitz-Kosevich quantum oscillation amplitude growth at low temperatures

In addition to being sensitive to magnetic field tilt angles, the metamagnetic transition responds to changes in temperature. As shown in Fig. 5.11A, the metamagnetic transition moves lower in applied magnetic field with increasing temperature. This can be seen on

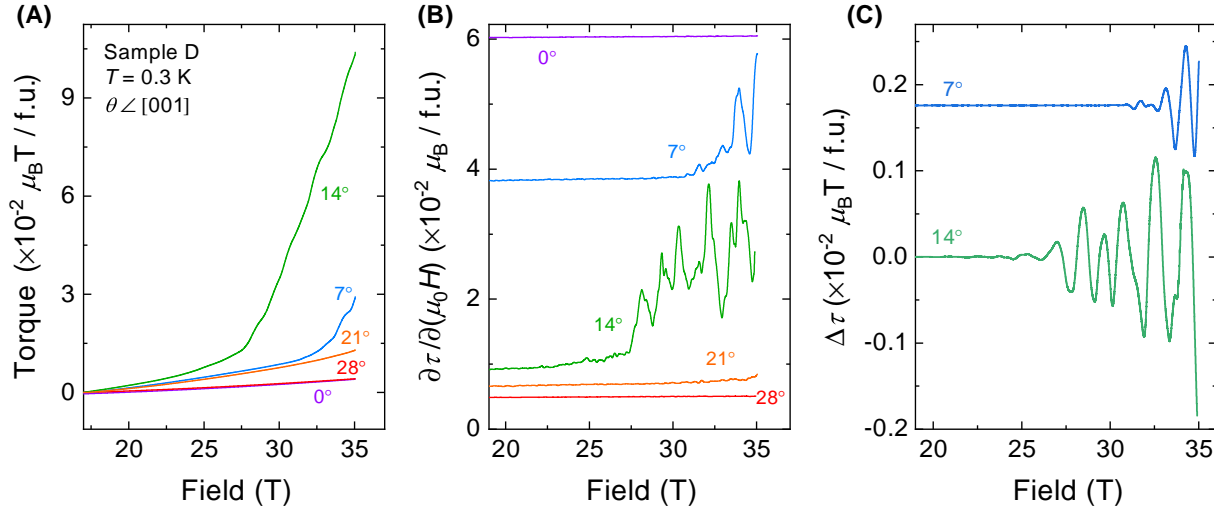


Fig. 5.10. Evolution of insulator-to-insulator metamagnetic transition as a function of angle. (A) Evolution of measured magnetic torque background, showing an acute sensitivity to magnetic field tilt angles θ . θ is measured from the [001] crystallographic direction (0°) towards the vector normal to the (110) plane (90°). (B) Derivatives of the magnetic torque backgrounds shown in (A). The metamagnetic transition and accompanying onset of prominent quantum oscillations is observable within the accessible magnetic field range up to 35 T at magnetic field tilt angles of 7° and 14° , but rapidly moves beyond the accessible magnetic field range at other angles. Data for each angle have been vertically offset for clarity. (C) Background subtraction reveals large amplitude quantum oscillations appear above the kink in the magnetic torque background shown in (A), where the onset field changes significantly between magnetic field tilt angles of 7° and 14° . Data for each angle have been vertically offset for clarity.

increasing field sweeps from the sharp change in the slope of the torque background, which moves from ≈ 28.6 T at the lowest measured temperature of 0.62 K to ≈ 27.3 T at the highest measured temperature of 1.29 K. Similarly, the rejoining of the low field phase on decreasing field sweeps moves from ≈ 22.4 T at 0.62 K to ≈ 19.7 T at 1.29 K. The inset to Fig. 5.11A shows this trend through a plot of the measured metamagnetic transition field as a function of temperature. As the onset of prominent quantum oscillations is coupled to the metamagnetic transition, this sensitivity to temperature complicates the conventional LK temperature analysis of quantum oscillation amplitudes.

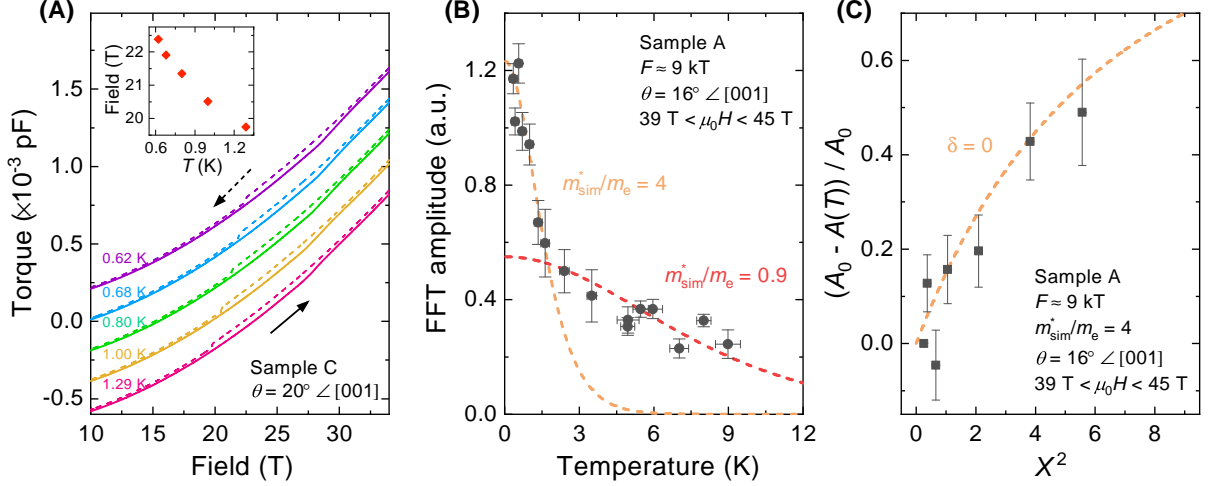


Fig. 5.11. Rapid quantum oscillation amplitude growth at low temperatures deviating from Lifshitz-Kosevich behavior. (A) Measured magnetic torque background at various temperatures, where the metamagnetic transition can be seen. The metamagnetic transition is observed to move lower in applied magnetic field with increasing temperature. Solid lines indicate sweeps with increasing field, while dashed lines indicate sweeps with decreasing field. The inset shows a plot of the metamagnetic transition as a function of temperature. (B) Temperature dependence of the quantum oscillation amplitude of the 9 kT frequency for the field range 39–45 T, showing a striking low temperature departure from the conventional Lifshitz-Kosevich (LK) temperature dependence. The orange dashed line shows a LK simulation for quasiparticle effective mass $m^* = 4 m_e$, while the red dashed line shows a LK simulation for $m^* = 0.9 m_e$. Neither simulations are able to capture the temperature dependence of the quantum oscillation amplitude over the full temperature range. (C) Low temperature expansion highlighting the growth of the 9 kT frequency dHvA oscillations at the lowest measured temperatures, using the same prescription as Chapter 4. $A(T)$ is the FFT amplitude at temperature T , A_0 is the amplitude at the lowest measured temperature, $X = 2\pi^2 k_B T / \hbar \omega_c$ is the temperature damping coefficient in the LK formula [13], $\delta = 2\pi \Delta / \hbar \omega_c$ where Δ is the isotropic gap size, and ω_c is the cyclotron frequency. Experimental data (solid squares) plotted using $m^* = 4 m_e$, taken from the simulation for the low temperature region in (A), exhibits good agreement with gapless ($\delta = 0$) model simulation (dashed line). Model calculations are shown in Appendix B.

Despite the complication, an analysis of the temperature dependence of quantum oscillation amplitudes shows potential insights into the low temperature LK deviation first reported in SmB₆ [11, 12]. Fig. 5.11B shows measured quantum oscillation amplitude as a function of temperature for the 9 kT frequency in the high field range between 39 – 45 T. The oscillation amplitudes increase sharply at temperatures below ≈ 2 K, far above the expectations from an LK simulation incorporating only the higher temperature data points. As the metamagnetic transition occurs at lower fields with increasing temperature, an earlier onset of prominent quantum oscillations could lead to higher than expected oscillation amplitudes, thereby producing a deviation from conventional LK behavior.

Intriguingly, a separate LK simulation using a heavier effective mass can be made to the quantum oscillation amplitudes below the upturn at ≈ 2 K (Fig. 5.11B). Using the same low temperature expansion procedure described in Chapter 4 and derived in Appendix B, Fig. 5.11C shows quantum oscillation amplitudes following a $X/\sinh(X)$ dependence, according to conventional LK theory, down to the lowest measured temperatures. As the charge gap in FeSb₂ is noticeably larger than that in YbB₁₂ and is minimally affected by applied magnetic fields, the observed exponential increase in quantum oscillation amplitudes at low temperatures starkly contrasts a plateauing or decrease in amplitude expected for gapped models of quantum oscillations [112, 113]. The temperature dependence of quantum oscillation amplitude therefore serves as strong evidence that insulating quantum oscillations in FeSb₂ arise from gapless excitations.

Chapter 6

Towards the origin of insulating quantum oscillations

6.1 Proposed models of insulating quantum oscillations

Following the discovery of intrinsic bulk quantum oscillations in SmB_6 , we were confronted with the mystifying question of how a characteristically metallic phenomenon could appear in an insulator. As discussed in Chapter 2, our current theory of quantum oscillations is posited on the quantization of available energy states when itinerant charge carriers are subjected to an applied magnetic field. As charge carriers are localized in insulators, the Landau quantization that gives rise to quantum oscillations are not expected to take place.

One obvious possibility is that the observed quantum oscillations arise from extrinsic sources. Arguments have for instance been made for impurity inclusion [158–160], disorder [161], tunneling [113], and Kondo breakdown [162]. Despite these suggestions, high quantum oscillation frequencies and an unusual temperature dependence of oscillation amplitudes [11], complementary signs of itinerant low energy excitations [12], and stringent sample characterization [122] suggest that extrinsic factors are unlikely to be responsible for insulating phase quantum oscillations in SmB_6 . As we have seen in Chapters 4 and 5,

extrinsic sources are also unlikely to be the root of insulating quantum oscillations in YbB_{12} and FeSb_2 .

Other possibilities of quantum oscillations arising without a Fermi surface have also been explored. Using dynamic mean field calculations, Ref. [115] finds that correlation effects and nonlocal hybridization could give rise to quantum oscillations without a corresponding Fermi surface in the insulating phase. This is essentially caused by a vanishing of the hybridization gap in the two-dimensional plane perpendicular to the applied magnetic field, which leads to small Fermi surface sections that are unlike what have been observed in SmB_6 and FeSb_2 . The heavy effective masses seen in YbB_{12} , a signature of strong correlations, would also be difficult to explain with selective closures of the hybridization gap. Another possibility, proposed by Ref. [116], is that insulators with inverted bandstructures experience periodic narrowing of the gap in an applied magnetic field. The gap narrowing can lead to oscillations in the bulk density of states, which become observable when the energy gap is comparable to the Landau level spacing. However, since this effect is thermally activated, the quantum oscillation amplitude would be expected to vanish at low temperatures, contrary to experimental observations. A further possibility, by Ref. [163], is that quantum oscillations could arise from filled bands in insulators with strong particle-hole asymmetry. When the band slope changes abruptly on a scale smaller than the typical Landau level spacing, the abrupt change would be reflected in the grand canonical potential, resulting in oscillations in physical properties. Since the density of states is unaffected, however, this model is not compatible with quantum oscillations in resistivity, which has now been observed in YbB_{12} .

We are therefore led to the possibility that insulating quantum oscillations are the product of charge-neutral low-energy excitations. One type of models predicting charge-neutral spinon Fermi surfaces in single-band Mott insulators pre-dates the discovery of quantum oscillations in SmB_6 [106, 107, 164, 165]. These models have been developed for frustrated spin systems, where a dynamically generated spinon gauge field produces a spinon Fermi surface with some unusual properties. For instance, calculations reported in Ref. [107] predict the material susceptibility to tend to a constant at low temperatures and specific heat capacity to follow a $T^{2/3}$ dependence. Ref. [164], on the other hand, derives a constant low temperature susceptibility but a T -linear dependence for specific heat capacity and thermal conductivity.

Further, Ref. [165] predicts large magnitude thermal Hall effect driven by the Lorentz force to be a distinguishing feature of a spin liquid in frustrated systems. Most relevant to our work, Ref. [107] has found that an externally applied magnetic field could lead to Landau quantization of the spinons. However, the same study suggests that magneto-oscillations are unlikely to be detected in these systems, since the homogenous state where oscillations are expected to be visible is preempted by an instability caused by finite temperatures. A further complication is that it remains unclear how a spinon Fermi surface would produce quantum oscillations in resistivity, making the model potentially incompatible with YbB_{12} .

A number of new charge-neutral low-energy models have been specifically devised to address insulating quantum oscillations in SmB_6 . For instance, in a model of low energy excitations arising from Majorana fermions, one neutral Majorana band that coincides in energy with the conduction band crosses the chemical potential, thereby producing a Fermi surface that corresponds to the conduction electron Fermi surface [108–110]. Although this model addresses the torque quantum oscillations observed in SmB_6 , one question that arises from our work on YbB_{12} is whether it can also account for quantum oscillations in resistivity. Especially as the Majorana fermion model was devised specifically to decouple electric responses to account for the lack of resistivity quantum oscillations in SmB_6 , it remains to be seen whether an argument similar to that given by Pippard for resistivity quantum oscillations can be made for this model [13].

Another model of charge-neutral low-energy excitations invoke composite Fermionic excitons [111, 166]. In this case, mixed-valence insulators are proposed to host a fractionalized neutral Fermi sea, which develops an emergent gauge field in the presence of a physical magnetic field. The quantization of the composite exciton Fermi sea would lead to quantum oscillations in both magnetic torque and resistivity, which correspond to a Fermi surface of the same volume as the conduction electron Fermi surface. A caveat with this model is that a quantitative relationship between the applied magnetic field and the effective internal field experienced by the composite fermions does not yet exist. The temperature dependence of the quantum oscillation amplitudes is predicted to plateau earlier and at a lower value than the Lifshitz-Kosevich formula. Since the amplitude of quantum oscillations observed in YbB_{12} follows the LK formula, and those in SmB_6 and FeSb_2 exceed the LK formula, it

remains to be seen whether the composite exciton model can capture these behaviors.

As we can see, there has yet to be a theoretical proposal that can completely capture the experimentally observed quantum oscillations in SmB_6 , YbB_{12} , and FeSb_2 . While a charge-neutral Fermi surface that arises from novel excitations of spinons, excitons, or Majorana fermions appears possible, our quantum oscillation studies on YbB_{12} and FeSb_2 have placed additional constraints on theoretical proposals to explain insulating quantum oscillations.

6.2 Metamagnetism and insulating quantum oscillations

One important discovery our work has led to is that of the novel metamagnetic transition in FeSb_2 . Such a feature in magnetic torque has not previously been seen in SmB_6 or in YbB_{12} , and neither material exhibit quantum oscillation onsets as sharp as that in FeSb_2 . Although the sudden change in quantum oscillation spectrum following a transition is reminiscent of the behavior of YbB_{12} across the insulator-to-metal transition, there is a notable difference in whether the field-induced transition couples to electric charge. For YbB_{12} , the enhancement of quantum oscillations is preceded by a few orders of magnitude decrease in the electrical resistance. On the other hand, as described in Chapter 5, the electrical resistance and indirect charge gap of FeSb_2 remain robust up to an applied field of 56 T. Electrical resistance measured at the same tilt angle where prominent quantum oscillations were observed remain smooth and robustly insulating in the region where the metamagnetic transition appears in torque. This suggests the large amplitude quantum oscillations we observed in FeSb_2 are not associated with a collapse of the charge gap and accompanying low-energy charge fluctuations. Instead, the transition likely corresponds to the gap closure of neutral excitations that do not participate in longitudinal charge transport, for instance those discussed in the previous section. Such a possibility had previously been raised by Monte Carlo simulations of a two-dimensional Kondo lattice, where a region of the low temperature phase diagram sustains neutral gapless excitations while the charge gap remains finite (Fig. 6.1) [12, 167].

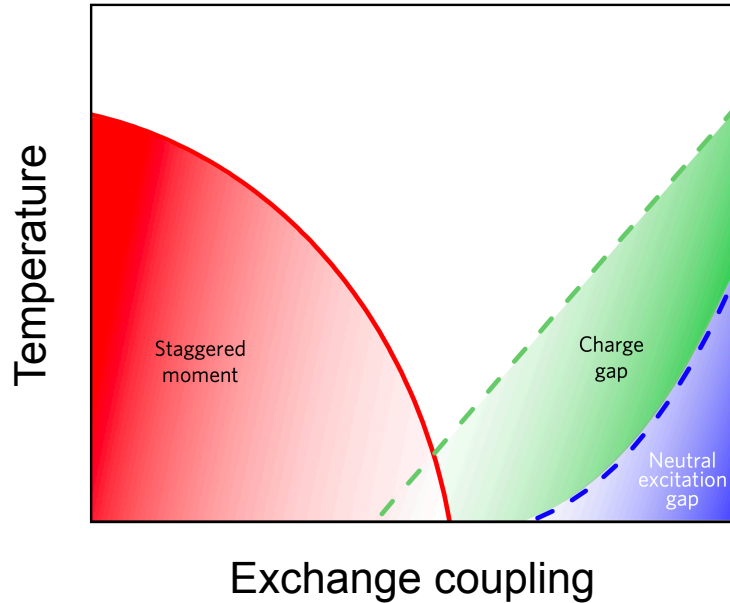


Fig. 6.1. Schematic phase diagram for closure of neutral excitation gap. Phase diagram depicting the closure of a neutral excitation gap while the charge gap remains finite for a two-dimensional Kondo lattice model. Figure adopted from Ref. [12] with computation results from Ref. [167].

It could be the case that the ground states of SmB_6 and YbB_{12} are already in this region of the phase diagram, whereas FeSb_2 enters this region in an applied magnetic field.

The enhancement of quantum oscillation amplitude and frequency in FeSb_2 bears similarities to the recent observation of quantum oscillations in the thermal conductivity of $\alpha\text{-RuCl}_3$. In $\alpha\text{-RuCl}_3$, small amplitude oscillations that are visible in the honeycomb zig-zag antiferromagnet phase undergo significant change upon entering the quantum spin liquid phase – the quantum oscillation amplitudes are strongly enhanced and a faster quantum oscillation frequency becomes visible [168]. The enhancement of quantum oscillations upon transitioning into a phase without charge transport or long range magnetic ordering is an interesting parallel between $\alpha\text{-RuCl}_3$ and FeSb_2 . However, one notable difference is that there has thus far been no direct evidence of a magnetic phase transition in the field range

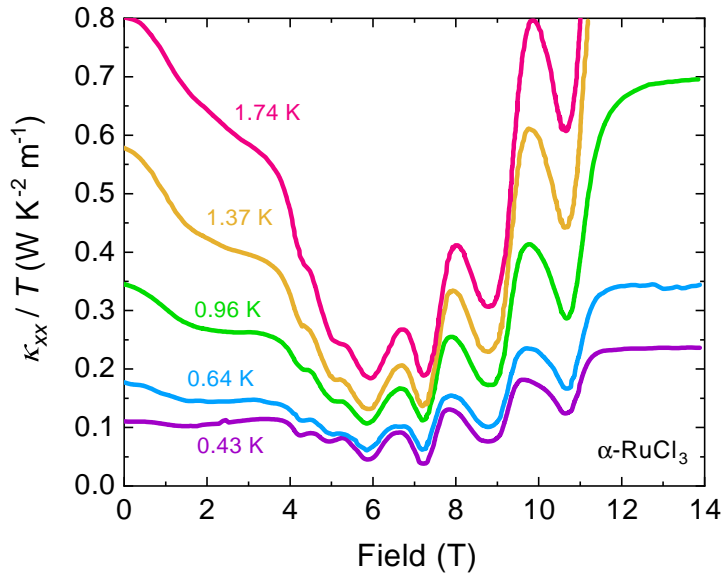


Fig. 6.2. Quantum oscillations in thermal conductivity of α -RuCl₃. Quantum oscillations in the thermal conductivity of α -RuCl₃ onsets abruptly as the material transitions from the honeycomb antiferromagnetic phase to the quantum spin liquid phase at ≈ 7.3 T. The quantum oscillations then abruptly end as the material enters the paramagnetic phase at ≈ 11 T. The abrupt onset of quantum oscillations is reminiscent of FeSb₂ as it crosses the metamagnetic transition. Figure adopted from Ref. [168].

where the metamagnetic transition was observed in FeSb₂, whereas α -RuCl₃ transitions out of an ordered magnetic phase when quantum oscillations are enhanced. As discussed in Chapter 5, calculations by our collaborator Michelle Johannes suggests that FeSb₂ could be on the brink of antiferromagnetism, ferrimagnetism, or other types of ordered magnetism. Going forward, it would therefore be informative to investigate whether the metamagnetic transition in FeSb₂, and potentially an order parameter associated with insulating quantum oscillations, could be observed with local magnetic probes at high fields [169].

6.3 Band hybridization and quantum oscillations

Another important finding from our study of YbB_{12} and FeSb_2 is that a variety of Fermi surfaces could be sustained in correlated insulators. Existing literature show that the large and light Fermi surface discovered in SmB_6 closely resembles the conduction electron Fermi surface in its non-magnetic metallic isostructural counterpart, LaB_6 [11, 12, 122]. On the other hand, as we have seen in Chapter 4, the small and heavy Fermi surface observed in the insulating phase of YbB_{12} corresponds well to Fermi surface sections that would result from shifting the calculated bandstructure of YbB_{12} such that the Fermi energy lies in either the valence band or the conduction band. The high frequency quantum oscillations that corresponds to 20% of the first Brillouin Zone in FeSb_2 with relatively light effective masses suggests that FeSb_2 is similar to SmB_6 . Comparing the three materials naturally raises the question of why insulating quantum oscillations in YbB_{12} are so different from those in SmB_6 and FeSb_2 in terms of frequencies and quasiparticle effective mass.

One potential explanation lies in the hybridization mechanisms of the three materials. In YbB_{12} , calculations by our collaborator Michelle Johannes show two partially filled unhybridized boron s - and p -electron conduction bands cross the Fermi energy and are gapped by hybridization with the Yb f -electron band (Fig. 6.3B) [103]. This contrasts the hybridization mechanism in SmB_6 , which occurs between a single conduction d -electron band that crosses the Fermi energy and a non-dispersive f -electron band. (Fig. 6.3A) [170]. FeSb_2 is similar to SmB_6 , where calculations suggest the gapped valence and conduction bands in the material are formed through the hybridization of a Fe- $3d$ band with a Sb- $4p$ band [157, 172].

Another difference between these two groups of materials lie in how they respond to external stimuli in the form of applied magnetic field and pressure. While YbB_{12} can be metallized with applied magnetic fields of as low as 47 T, SmB_6 is minimally affected by applied magnetic fields up to at least 100 T [173], and FeSb_2 does not show signs of metallization up to at least 55 T (Fig. 5.4C). In contrast, SmB_6 and FeSb_2 can be metallized with applied hydrostatic pressures on the order of 100 kbar [174, 175], whereas YbB_{12} requires applied pressures on the order of Mbar to be metallized [176].

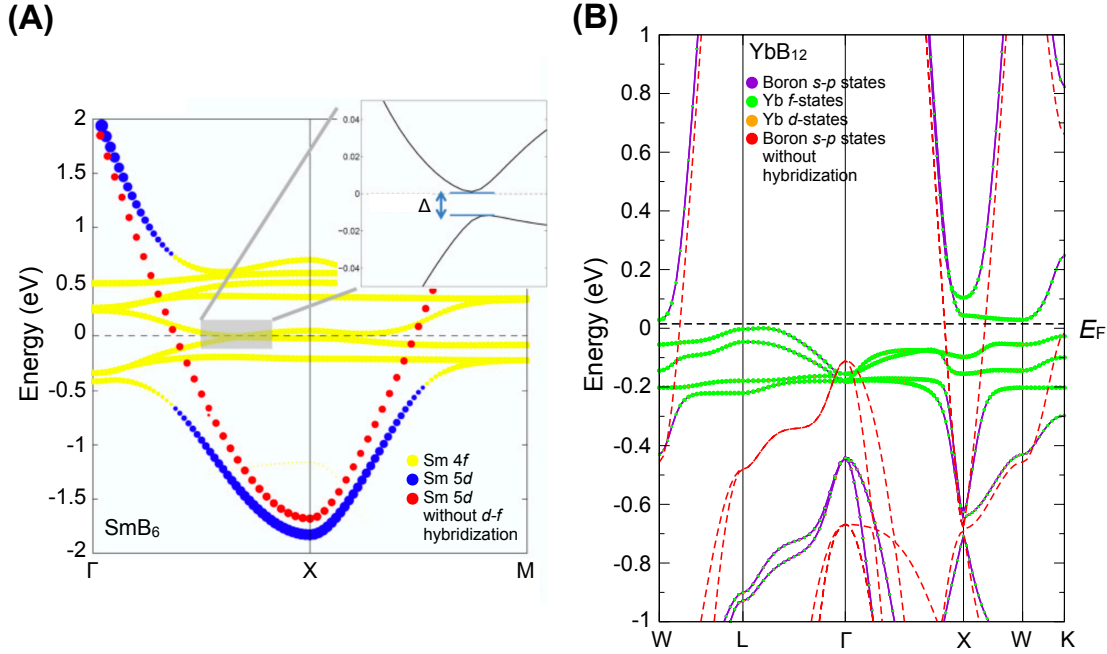


Fig. 6.3. Contrasting band structure of SmB_6 and YbB_{12} . (A) Band structure of SmB_6 from GGA calculations in [170], zoomed in near the Fermi energy E_F (full energy range shown in [170]). Sizes of yellow and blue dots denote weights of Sm-4*f* and Sm-5*d* in various bands. Red dots denote metallic Sm-5*d* orbitals without hybridization with Sm-4*f* orbitals. (B) Calculated band structure of YbB_{12} shown with an expanded view around the Fermi energy E_F (full energy range shown in Fig. 4.17). Size of the circles are proportional to the weight at each k -point, green circles are Yb *f*-states, orange circles are Yb *d*-states, and violet circles are boron *s-p*-states. Red dashes denote two partially filled unhybridized boron *s-p* conduction electron orbitals without hybridization with Yb-*f* orbitals. In both cases, the Fermi surface yielded by the unhybridized band is not simply connected, leading to a large number of expected frequencies [11, 103]. Calculations for YbB_{12} were performed by our collaborator Michelle Johannes [171].

The differing response to external stimuli in the form of applied magnetic field and hydrostatic pressure likely relates to each material's hybridization mechanism. Applied pressure changes a material's unit cell volume and the spatial overlap of electronic states, which can lead to a breakdown of hybridization by changing the relative positions of the bands [175]. Once the energy gap is closed by a breakdown of hybridization, large and light Fermi sur-

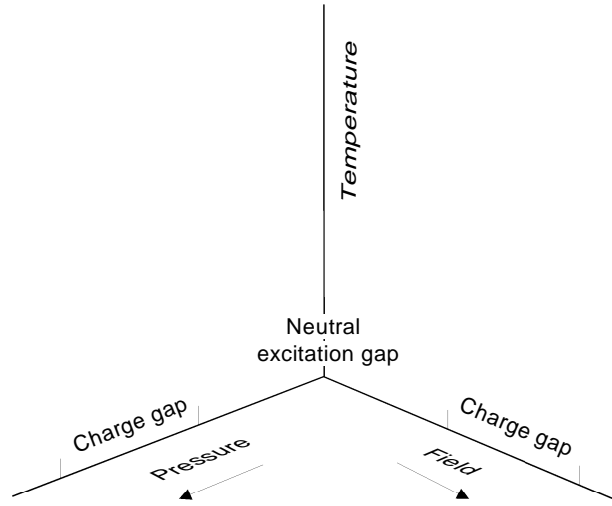


Fig. 6.4. Schematic phase diagram for magnetic field and pressure tuning of quantum oscillatory insulators. Schematic depicting a three-dimensional phase diagram where applied magnetic field and pressure can independently close the neutral excitation gap and charge gap of a material. Figure inspired by Ref. [12], which incorporates computation results from Ref. [167].

face sections corresponding to the underlying dispersive conduction electron band would be expected. Quantum oscillation data thus far suggest the insulating Fermi surfaces in SmB_6 and FeSb_2 reflect the large and light conduction electron Fermi surfaces that would result when hybridization breaks down. Since hybridization in YbB_{12} involves three bands, the relative shift in the positions of these bands could have a smaller effect. Applied magnetic field, on the other hand, splits the bands through the Zeeman effect. In this case, the larger Landé g -factor of ≈ 3.5 in YbB_{12} leads to a stronger response compared to SmB_6 and FeSb_2 , both with g -factors on the order of less than 1 [177, 178]. When Zeeman splitting causes the largely non-dispersive hybridized bands to cross the Fermi energy, small Fermi surface sections corresponding to a heavy fermion metal would be expected. This agrees with our quantum oscillation study and an independent specific heat study on metallic YbB_{12} [97].

From the above comparison, we could expand the phase diagram in Fig. 6.1 by adding an additional dimension. Instead of a single tuning parameter that controls the neutral

excitation gap and the charge gap, we allow applied pressure and field to act independently, for instance as depicted by the schematic in Fig. 6.4. Similar to the two-dimensional version of the phase diagram, the appearance of neutral gapless excitations foretells the charge gap closure. With the additional tuning parameter, however, we are able to incorporate different types of neutral gapless excitations in the insulating phase.

On the phase diagram in Fig. 6.4, the point of charge gap closure for SmB_6 and FeSb_2 along the pressure axis would be closer to the origin than its counterpart along the field axis. In such materials that are proximate to their pressure-tuned metallic phase, neutral gapless excitations in the ambient pressure insulating phase could mirror an unhybridized, dispersive conduction band Fermi surface. In YbB_{12} , on the other hand, the point of charge gap closure along the field axis would be closer to the origin than its counterpart along the pressure axis. In such materials that are proximate to their field-tuned metallic phase, neutral gapless excitations in the ambient pressure insulating phase could mirror a correlated heavy fermion Fermi surface. Under this interpretation, the metamagnetic transition observed in FeSb_2 would correspond to a closure of the neutral excitation gap, leading to the appearance of large amplitude, high frequency quantum oscillations. On the other hand, in SmB_6 and YbB_{12} , neutral excitations may already be gapless in ambient field and pressure, as suggested by specific heat capacity and thermal conductivity measurements [12, 96]. The type of Fermi surface sustained in the insulating phase, in terms of size and quasiparticle effective mass, would thus depend on how a particular material has been tuned by external stimuli.

Since this three-dimensional neutral excitation phase diagram is only speculation, it would be valuable to pursue further experiments to determine whether the insulating Fermi surfaces in SmB_6 and FeSb_2 indeed reflect their pressure-induced metallic counterparts. It would also be useful to explore if other, yet to be discovered quantum oscillatory insulators follow the trend in field and pressure tuning. Even more importantly, the physical origin of the neutral excitations that underlie insulating phase Fermi surfaces needs to be determined. To this end, studying the metamagnetic transition in FeSb_2 with probes of low energy excitations at high fields, such as specific heat capacity and thermal conductivity, as well as probes of bulk and local magnetism at high fields, such as force magnetometry and neutron scattering, should yield invaluable insight.

Chapter 7

Conclusions

“More is different”
– P. W. Anderson

Our group’s work has built on the surprising discovery of a bulk Fermi surface in the Kondo insulator SmB_6 and set in motion a vibrant field of study around unconventional bulk insulating Fermi surfaces in multiple strongly correlated insulators. In the insulating regime of YbB_{12} , a detailed study of the quantum oscillation amplitude as a function of temperature showed evidence that these unconventional oscillations arise from gapless low-energy excitations within the bulk charge gap. By measuring quantum oscillations in the field-induced metallized phase of YbB_{12} [69], it became apparent that the small and heavy Fermi surface sections in the unconventional insulating phase reflect the Fermi surface in the metallized phase where Kondo hybridization remains robust [97]. The contrast to the high frequency quantum oscillations with light effective masses observed in SmB_6 and FeSb_2 , considered in light of the two materials’ differing hybridization mechanism to that of YbB_{12} , suggests that differing hybridization mechanisms of the host bulk unconventional insulators give rise to insulating Fermi surfaces with varying geometries and masses.

Quantum oscillation studies in FeSb_2 revealed further insight into the origin of unconventional insulating quantum oscillations. Here, a novel metamagnetic transition manifests as

a sharp slope change in the magnetic torque background. Prominent hysteresis loops were observed in the magnetic torque, indicative of a high field insulating magnetic phase. The metamagnetic transition is accompanied by a strong enhancement of quantum oscillation amplitude and frequency spectrum, without corresponding features in electrical resistivity. A transition that couples strongly to quantum oscillations lends credence to the proposal of a new insulating magnetic subphase, where the neutral low energy excitation gap closes while the charge gap remains finite, that underlie unconventional insulating quantum oscillations [12, 167]. Temperature-evolution of the novel metamagnetic transition also hints at the cause of a strong growth in quantum oscillation amplitude at low temperatures exceeding the expectations of the Lifshitz-Kosevich formulation observed in both SmB_6 and FeSb_2 [11, 12].

It is an exciting time to be involved in unconventional insulators. What began as a surprising discovery of bulk, neutral quantum oscillations in the Kondo insulator SmB_6 has blossomed into a vibrant field involving three families of strongly correlated insulators: SmB_6 , YbB_{12} , and FeSb_2 . Very recently, new and more exotic entrants have entered the arena, including the two-dimensional monolayer large-gap topological insulator WTe_2 [179] and the layered insulator $\alpha\text{-RuCl}_3$ [168], the latter of which possessing a charge gap of 1.9 eV!

Of course, much remains to be done with the original trio of SmB_6 , YbB_{12} , and FeSb_2 . While the lack of resistivity quantum oscillations in SmB_6 has always been a point of contention, the observation of SdH oscillations in YbB_{12} has raised the urgency to either confirm or comprehensively rule out SdH oscillations in SmB_6 . This is particularly relevant as a recent study using Corbino disks show that bulk resistivity in SmB_6 continues to increase even in the low temperature plateau region that appears in traditional four-point contacted resistivity measurements [180]. It is therefore possible that SmB_6 exhibits bulk SdH oscillations, but the oscillations are screened from four-point measurements by a surface conduction layer. In the case of YbB_{12} , the low temperature resistivity plateau that is indicative of surface conduction layers appears to be moderated in high applied magnetic fields [88], potentially explaining the appearance of resistivity quantum oscillations at high fields. As early models of unconventional quantum oscillations deliberately decouple from electric fields to accommodate for the lack of SdH oscillations in SmB_6 , it is important to verify whether bulk resistivity quantum oscillations are indeed absent in the material. By the same token, SdH

oscillations should also be investigated in FeSb₂.

Another line of inquiry involves probing the pressure-induced metallized phases of SmB₆ and FeSb₂. As we have found in YbB₁₂, robust hybridization between Yb *f*-states and dispersive Boron *s*- and *p*-states yields small Fermi surface sections with heavy quasiparticle effective masses in both the insulating and field-induced metallic regimes. It would be informative to investigate whether the large Fermi surface sections observed in the insulating phase of SmB₆ and FeSb₂ persist in their respective metallized regimes. As both materials undergo insulator-to-metal transitions at pressures on the order of 100 kbar, this would be a task for contacted or contactless resistivity measurements using anvil pressure cells [174, 175].

It would also be important to examine the novel metamagnetic transition in FeSb₂ in further detail. Most importantly, complementary high field magnetic probes could be used to investigate whether collective magnetic phases, such as antiferromagnetism, ferrimagnetism, or textured magnetic phases are associated with the high field phase above the novel metamagnetic transition [169]. Investigating the precise behavior of the metamagnetic transition could provide hints on how to look for a similar transition in other unconventional insulators, which aid the search for additional quantum oscillatory insulators and further our understanding of this strange phenomenon.

Finally, there remains a question about the relationship between topology and unconventional insulating Fermi surfaces. Whereas SmB₆, YbB₁₂ [148], FeSb₂ [19], and WTe₂ [179] are all implicated with some type of topological phase, α -RuCl₃ does not appear to share this association. While this entire field of study was born from a desire to investigate the topological surface states in SmB₆, the relationship between nontrivial topology and unconventional insulating bulk quantum oscillations is not clear. Indeed, the observation of quantum oscillations in α -RuCl₃ would seem to suggest that unconventional insulating phases are not exclusive to materials with potential topological phases. It would therefore be worthwhile to explore whether there are any links between topology and unconventional insulating Fermi surfaces, and whether any features separate unconventional quantum oscillations in materials implicated with topological phases from those that are not.

7. Conclusions

Appendix A

Absolute amplitude of magnetic torque quantum oscillations

As described in Chapter 3, torque magnetometry measures changes in a material's anisotropic magnetization. By converting the measured cantilever displacement to absolute units of magnetic moment per unit cell, we can discern whether the measured quantum oscillations are more likely to arise from the entire bulk of the sample or from thin surface layers [12].

By considering the dimensions and Young's modulus of our cantilevers, the cantilever spring constant is estimated to be $28(8) \text{ N}\cdot\text{m}^{-1}$, similar to values obtained from the gravitational displacement technique. The proportional change in capacitance, $\Delta C/C$, associated with a small deflection δ of the cantilever from its equilibrium position, is given by:

$$\tau = \mu B_0 \sin(\theta) = Lk\delta = Lkd \cdot \frac{\Delta C}{C}, \quad (\text{A.1})$$

where μ is the total magnetic moment experienced by a sample, $B_0 = \mu_0 H$ is the applied magnetic field, θ is the angle between \mathbf{B}_0 and $\boldsymbol{\mu}$, and L is the distance along the length of the cantilever between the anchored hinge and the sample. The final equality uses the fact that the measured capacitance is inversely proportional to the spacing d between the cantilever and base plate.

A. Absolute amplitude of magnetic torque quantum oscillations

Let us define the magnetic moment in units of Bohr magnetons per unit cell, $p_e = \mu/\mu_B \cdot V_{\text{u.c.}}/V_s$, where $V_{\text{u.c.}}$ is the unit cell volume and V_s is the sample volume. Substituting for μ , we find:

$$\Delta p_e = \Delta C \cdot \frac{V_{\text{u.c.}} L k d}{\mu_B V_s B_0 C \sin(\theta)} \equiv \alpha \frac{\Delta C}{B_0 \sin(\theta)}, \quad (\text{A.2})$$

where α is a constant. By applying the relevant numerical values for α , we can calculate the absolute amplitude of the experimentally measured magnetic torque quantum oscillations.

To compare the experimentally measured oscillation amplitude to theoretical expectations, we first write the Lifshitz-Kosevich formula as:

$$\widetilde{M} = M_0 \cdot R_T R_D \cdot \sin(2\pi F/B_0 + \phi) \cdot \sin(\theta), \quad (\text{A.3})$$

where R_T and R_D are damping factors due to temperature and impurity scattering, respectively [13]. The amplitude prefactor M_0 is given by:

$$M_0 = -\frac{\mu_B}{2\pi^4} \frac{m_e}{m^*} \sqrt{\frac{A_F^3 B_0}{F \left| \frac{\partial^2 \mathcal{A}}{\partial k_{\parallel}^2} \right|}}, \quad (\text{A.4})$$

where the variables are the same as those given in Chapter 2. This can be normalized to give the expected oscillation amplitude per unit cell, p_t :

$$\begin{aligned} p_t &= \frac{|\Omega_0| V_{\text{u.c.}}}{\mu_B} \\ &= f(r) \frac{2m_e}{m^*} \left(\frac{k_F}{\bar{k}_{\text{BZ}}} \right)^3 \sqrt{\frac{2B_0}{F}}, \end{aligned} \quad (\text{A.5})$$

where the Fermi wavevector $k_F \equiv \sqrt{\mathcal{A}/\pi} = \sqrt{2eF/\hbar}$ by the Onsager relation, $\bar{k}_{\text{BZ}} \equiv 2\pi/V_{\text{u.c.}}^{1/3}$, and the anisotropy term $f(r) \equiv \sqrt{2\pi/|\partial^2 \mathcal{A}/\partial k_{\parallel}^2|}$.

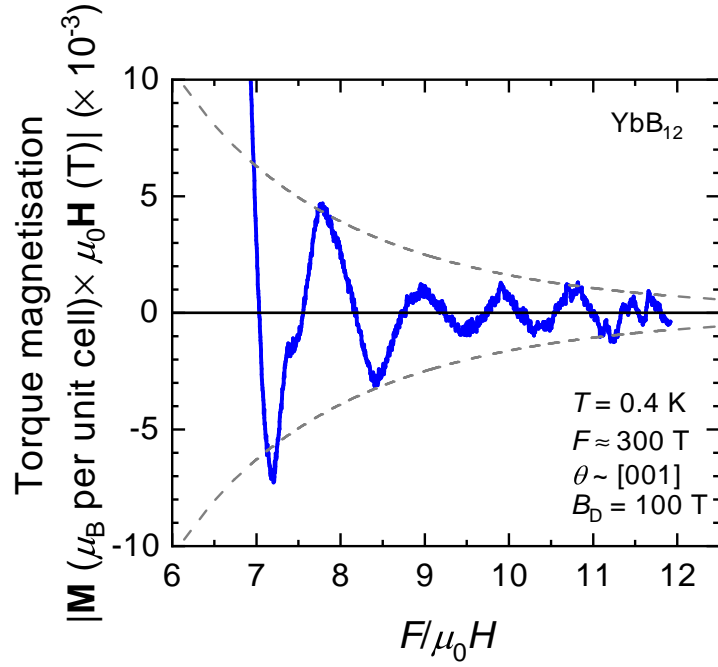


Fig. A.1. Absolute amplitude of magnetic torque quantum oscillations in YbB₁₂. Magnetic torque measured on a single crystal of YbB₁₂ converted into absolute units of μ_B per unit cell using Eq. A.2. The α term is calculated using the following values: $V_{\text{u.c.}} = 7.47^3 = 417\text{\AA}^3$, $L = 3.1$ mm, $k = 190$ N m⁻¹, $d = 0.1$ mm, and $V_s = 0.9 \times 0.5 \times 0.3$ mm³, which yields a value $\alpha = 20$ T pF⁻¹ μ_B per unit cell [103]

A.1 YbB₁₂

For quantum oscillations in YbB₁₂, the constant α in Eq. A.2 can be found by applying the following numerical values: $V_{\text{u.c.}} = 7.47^3 = 417\text{\AA}^3$, $L = 3.1$ mm, $k = 190$ N m⁻¹, $d = 0.1$ mm, and $V_s = 0.9 \times 0.5 \times 0.3$ mm³ [103]. With these, we find $\alpha = 20$ T pF⁻¹ μ_B per unit cell, with which we can convert the measured torque signal into absolute units, as shown in Fig. A.1.

For the dominant 300(70) T frequency, we can fit an envelope to the observed oscillations to extract a Dingle damping factor of $R_D = \exp(-B_D/B_0)$ with $B_D \approx 100$ T. While we are unable to directly calculate the anisotropy term $f(r)$, we estimate the term to be of the order 0.5–1 from the observation that quantum oscillation frequencies do not appear to vary

A. Absolute amplitude of magnetic torque quantum oscillations

significantly with angles. Likewise, we estimate $\sin(\theta)$ to be of the order 0.5–1. Using these assumptions, we arrive at a theoretically expected amplitude for the 300(70) frequency in the range $1\text{--}4 \times 10^{-4} \mu_B$ per unit cell at an applied field of 45 T assuming contributions from the entire bulk of the sample, which is approximately the same order of magnitude as the observed oscillations.

A.2 FeSb₂

For quantum oscillations in FeSb₂ presented in Fig. 5.6 in Chapter 5, the constant α can be found by applying the following numerical values: $V_{\text{u.c.}} = 5.83 \times 6.53 \times 3.19 = 121 \text{ \AA}^3$, $L = 3.8 \text{ mm}$, $k = 28 \text{ N m}^{-1}$, $d = 0.1 \text{ mm}$, and $V_s = 0.95 \times 1.12 \times 0.57 \text{ mm}^3$. With these, we find $\alpha = 0.23 \text{ T pF}^{-1} \mu_B$ per unit cell.

One complication arises from the lack of a definitive effective mass due to low temperature quantum oscillation amplitude growth that exceeds the expectations from LK theory. We examine the dominant $\approx 1450 \text{ T}$ frequency, for which we can roughly estimate the effective mass (m^*) to be between 0.1–1 m_e , from the fact that the measured oscillations persist up to at least 10 K. By fitting an envelope to the observed oscillations, we find that the $\approx 1450 \text{ T}$ frequency experiences a Dingle damping $R_D = \exp(-B_D/B_0)$ with $B_D \approx 150 \text{ T}$. If we approximate $\sin(\theta)$ and $f(r)$ to be within roughly the range 0.1–1, we can estimate the theoretical amplitude for the measured oscillations in the limit of low temperature, infinite field, and zero spin splitting. For the dominant $\approx 1450 \text{ T}$ frequency, we expect bulk oscillations to have an amplitude roughly in the range of 10^{-5} to $10^{-3} \mu_B$ per unit cell at an applied field of 42 T (possible Fermi surface pocket degeneracy adds further uncertainty to this estimate). Now, the experimentally observed oscillation amplitude of the $\approx 1450 \text{ T}$ frequency at an applied field of 42 T is $\approx 4.7 \times 10^{-4} \text{ pF}$, which equates to an absolute amplitude of $\approx 10^{-4}/\sin(\theta) \mu_B$ per unit cell. We therefore see that the observed quantum oscillations are in within the same order of magnitude range as the theoretical expectations for a bulk, three dimensional Fermi surface.

Appendix B

Non-LK quantum oscillation amplitude temperature-dependence for gapped models compared with LK temperature-dependence for gapless models

B.1 Model simulations

To distinguish between gapless and gapped models of quantum oscillations in the unconventional insulating phase, we simulate the quantum oscillation amplitude for various gap sizes. Using the formulation of Ref. [112], which was developed for superconductors, the ratio of the first harmonic between the gapped state and the normal state is:

$$\frac{M_g}{M_n} = \frac{\sinh(X)}{X} \int_0^\infty \cos\left(\frac{X\mu}{\pi}\right) \partial_\mu \left(\frac{\mu}{\sqrt{\mu^2 + (\Delta/T)^2}} \tanh\left(\frac{\sqrt{\mu^2 + (\Delta/T)^2}}{2}\right) \right) d\mu, \quad (\text{B.1})$$

where μ is the chemical potential, Δ is the isotropic gap size, and X is the temperature damping coefficient given by $X = 2\pi^2 k_B T m^* / e\hbar B_0$. Here, k_B is Boltzmann's constant, T is

B. Non-LK quantum oscillation amplitude temperature-dependence for gapped models compared with LK temperature-dependence for gapless models

temperature, m^* is the quasiparticle effective mass, e is the electron charge, \hbar is the reduced Planck constant, and $B_0 = \mu_0 H$ is the applied magnetic field [13].

If we set $T = X\omega_c/(2\pi^2)$ and $\Delta/T = 2\pi^2\Delta/\omega_c X = \pi\delta/X$, we find:

$$\delta = \frac{2\pi\Delta}{\hbar\omega_c}, \quad (\text{B.2})$$

where ω_c is the cyclotron frequency. We therefore find the ratio of the first harmonic between the gapped state and the normal state to be:

$$\frac{M_g}{M_n} = \frac{\sinh(X)}{X} \int_0^\infty \cos\left(\frac{X\mu}{\pi}\right) \partial_\mu \left(\frac{\mu}{\sqrt{\mu^2 + (\pi\delta/X)^2}} \tanh\left(\frac{\sqrt{\mu^2 + (\pi\delta/X)^2}}{2}\right) \right) d\mu. \quad (\text{B.3})$$

Gapped model simulations of the non-LK form of quantum oscillation amplitude at low temperatures are shown in the lower inset to Fig. B.1A for various gap sizes (i.e. various sizes of δ), compared with the LK growth in quantum oscillation amplitude at low temperatures for gapless models (i.e. $\delta = 0$).

B.1.1 Model comparisons with experimental data in YbB₁₂

Fig. B.1 reproduces the temperature dependence of quantum oscillation amplitudes in the insulating regime of YbB₁₂ presented in Chapter 4. Upper insets to Fig. B.1A and Fig. B.1B show the growth in quantum oscillation amplitude of the 700 T frequency in magnetic torque and 800 T frequency in electrical resistivity plotted against X^2 , respectively [171]. An exponential low temperature growth of the measured quantum oscillation amplitude in accordance to the LK theory is observed for both electrical transport and torque magnetization.

For insulating YbB₁₂, the isotropic gap size is $2\Delta \approx 15$ K [100] at 40 T, the field range relevant for the temperature dependence measurement of quantum oscillation amplitudes. This gap size corresponds to $\delta \approx 12$ for an effective mass (m^*) of $7 m_e$ for the quantum oscillation frequencies shown in Fig. B.1. Simulations with various values of δ are shown

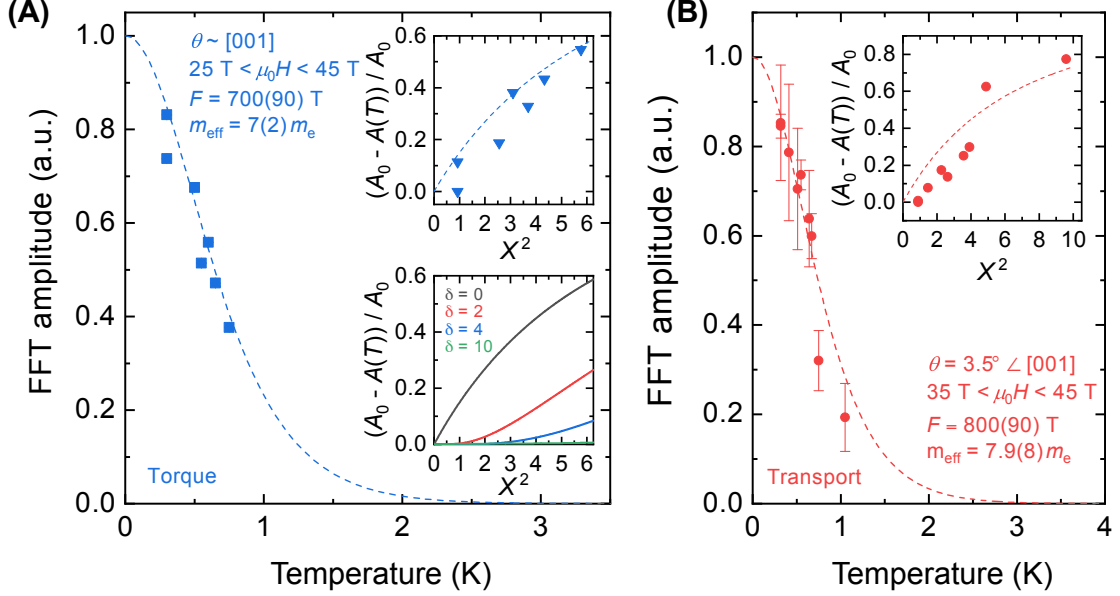


Fig. B.1. Gapless low energy excitations yield low temperature Lifshitz-Kosevich growth of quantum oscillation amplitude in the insulating phase of YbB_{12} . **(A)** Amplitude of the 700 T frequency magnetic torque quantum oscillations as a function of temperature, with the applied field aligned close to the [001] crystallographic direction. Measured quantum oscillation amplitude follows the Lifshitz-Kosevich (LK) form (dashed line) down to lowest measured temperatures. (Lower inset) Low temperature model expansion of quantum oscillation amplitude from Refs. [112, 113] shows non-LK activated behaviour for various finite gap sizes ($\delta \approx 12$ for YbB_{12} at 40 T [100]), in contrast to LK exponential growth expected for gapless low energy excitations ($\delta = 0$). $A(T)$ is the quantum oscillation amplitude at temperature T , A_0 is the amplitude at the lowest measured temperature, $X = 2\pi^2 k_B T / \hbar \omega_c$ is the temperature damping coefficient in the LK formula [13], $\delta = 2\pi \Delta / \hbar \omega_c$ where Δ is the isotropic gap size and ω_c is the cyclotron frequency. (Upper inset) Growth of magnetic torque quantum oscillation amplitude at the lowest measured temperatures; experimental data (solid triangles) exhibits good agreement with gapless model simulation (dashed lines). **(B)** Amplitude of the 800 T frequency electrical transport quantum oscillations as a function of temperature, with the applied field aligned 3.5° away from the [001] crystallographic direction in the [001]-[111]-[110] rotation plane. Measured quantum oscillation amplitude follows LK form (dashed line) down to lowest measured temperatures. (Inset) Growth of electrical transport quantum oscillation amplitude at lowest temperatures; experimental data (solid circles) exhibits good agreement with gapless model simulation (dashed line).

in the lower inset of Fig. B.1A [112, 113, 116]. For the gapless case ($\delta = 0$), quantum oscillation amplitude simulations show an exponential growth at low temperature, while for the gapped case (finite δ , shown for values up to $\delta = 10$, similar to YbB_{12} at an applied field of 40 T), quantum oscillation amplitude simulations show non-LK finite activation behavior at low temperatures. A comparison of measured quantum oscillation amplitude growth at low temperature with model simulations thus provides strong evidence for neutral gapless excitations in the unconventional insulating phase of YbB_{12} .

B.1.2 Model comparisons with experimental data in FeSb_2

As shown in Chapter 5, magnetic torque quantum oscillations observed in FeSb_2 continues to grow in amplitude down to the lowest measured temperatures (reproduced in Fig. B.2). One complication for FeSb_2 is that the amplitude growth at the lowest temperatures significantly exceeds what would be expected by fitting the LK formula to higher temperature data points. To avoid this complication, we focus on the lowest temperature region. At the lowest temperatures, the growth in the amplitude of the ≈ 9 kT quantum oscillation amplitude can be captured by a LK fit with a moderately heavy effective mass $m_{\text{sim}}^* = 4 m_e$ at the lowest temperatures. By plotting the relative change of quantum oscillation amplitude against X^2 using this effective mass, we see that the experimental data agrees well with model simulations assuming gapless excitations ($\delta = 0$) and contrasts significantly with gapped simulations ($\delta > 0$).

B.2 Low temperature model expansion

A further simplification could be made at low temperatures by using a low temperature expansion. We perform a series expansion of the temperature damping coefficient $R_T = \sinh(X)/X$ in the LK formula that describes the temperature dependence of quantum oscillations for particles obeying the Fermi-Dirac distribution [13].

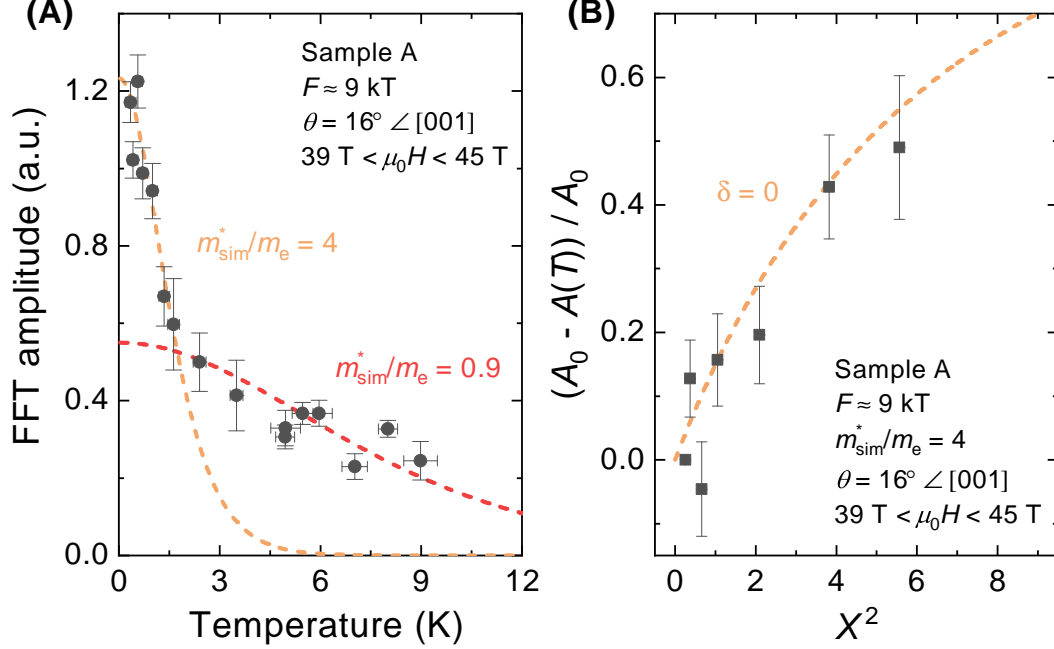


Fig. B.2. Gapless low energy excitations yield low temperature Lifshitz-Kosevich growth of quantum oscillation amplitude in the insulating phase of FeSb_2 . **(A)** Temperature dependence of the quantum oscillation amplitude of the 9 kT frequency for the field range 39–45 T, showing a striking low temperature departure from the conventional Lifshitz-Kosevich (LK) temperature dependence. The orange dashed line shows a LK simulation for quasiparticle effective mass $m^* = 4 m_e$, while the red dashed line shows a LK simulation for $m^* = 0.9 m_e$. Neither simulations are able to capture the temperature dependence of the quantum oscillation amplitude over the full temperature range. **(B)** Low temperature expansion highlighting the growth of the 9 kT frequency dHvA oscillations at the lowest measured temperatures. $A(T)$ is the FFT amplitude at temperature T , A_0 is the amplitude at the lowest measured temperature, $X = 2\pi^2 k_B T / \hbar \omega_c$ is the temperature damping coefficient in the LK formula [13], $\delta = 2\pi \Delta / \hbar \omega_c$ where Δ is the isotropic gap size, and ω_c is the cyclotron frequency. Experimental data (solid squares) plotted using $m^* = 4 m_e$, taken from the simulation for the low temperature region in (A), exhibits good agreement with gapless model simulation (dashed line).

For small T , a series expansion of the temperature dependence term yields:

$$R_T \approx 1 - \frac{X^2}{6} + O(X^4). \quad (\text{B.4})$$

B. Non-LK quantum oscillation amplitude temperature-dependence for gapped models compared with LK temperature-dependence for gapless models

The quantum oscillation amplitude therefore linearly increases with decreasing X^2 in the $T \rightarrow 0$ limit. The low temperature growth of quantum oscillation amplitude is captured by the relative amplitude change at a finite temperature $A(T)$ with respect to the amplitude at the lowest measured temperature A_0 . This can be expressed as:

$$\begin{aligned} 1 - \frac{A(T)}{A_0} &= \frac{A_0 - A(T)}{A_0} \\ &= \frac{X^2}{6}. \end{aligned} \tag{B.5}$$

A plot of $(A_0 - A(T))/A_0$ against X^2 would therefore yield a straight line with a gradient equal to $1/6$ at low temperatures for low-energy excitations within the gap. In contrast, in the absence of low-energy excitations, gapped quantum oscillation models would yield a much reduced change in amplitude as a function of X^2 at low temperatures well below the gap temperature scale (Lower inset to Fig. B.1A) [112, 113, 116]. A simplified comparison to distinguish between gapless and gapped forms of measured quantum oscillation amplitude is thus provided by this low temperature expansion.

Appendix C

Sample magnetic impurity content from Langevin fit

To determine the concentration of magnetic impurities in our FeSb₂ samples, we fit the magnetization as a function of applied magnetic field measured with the Quantum Design Inc. Magnetic Property Measurement System at constant temperature with the Langevin function [158]:

$$M(B_0, T) = \chi_{\text{bulk}} B_0 + c_{\text{impurity}} \mu_{\text{eff}} \left(\coth \left(\frac{\mu_{\text{eff}} B_0}{k_{\text{B}} T} \right) - \frac{k_{\text{B}} T}{\mu_{\text{eff}} B_0} \right), \quad (\text{C.1})$$

where χ_{bulk} is the intrinsic bulk susceptibility, B_0 is the applied magnetic field, c_{impurity} is impurity concentration, k_{B} is the Boltzmann constant, and T is temperature. The effective magnetic moment μ_{eff} , which is dependent on the material, was left as a free parameter in the fitting procedure and yielded a value of 5.4(3). As shown in Chapter 5 (reproduced below in Fig. C.1), the fit limits any magnetic impurity content in a FeSb₂ single crystal sample from the same growth batch as those used in high field quantum oscillation measurements to 60(20) parts per million.

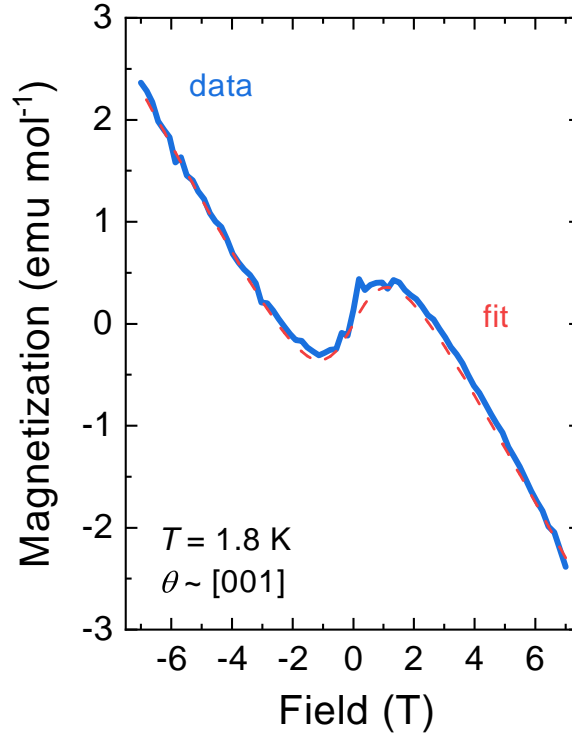


Fig. C.1. Langevin fit to magnetization measured on a single crystal sample of FeSb₂. The solid blue line shows magnetization measured on a single crystal sample of FeSb₂ at a constant temperature of 1.8 K with the applied magnetic field aligned close to the [001] crystallographic direction. The red dashed line shows a Langevin fit to the measured data, using Eq. C.1, with the effective magnetic moment μ_{eff} and magnetic impurity concentration c_{impurity} left as free parameters. The fit yielded an effective moment of 5.4(3) and a magnetic impurity concentration of 60(20) parts per million, evidencing high sample purity. This sample was from the same growth batch as those used in high field quantum oscillation measurements.

Bibliography

- [1] Pippard, A. B. the Cat and the Cream. *Phys. Today* **14**, 38–41 (1961).
- [2] Menth, A., Buehler, E. & Geballe, T. H. Magnetic and semiconducting properties of SmB₆. *Phys. Rev. Lett.* **22**, 295–297 (1969).
- [3] Kondo, J. Resistance Minimum in Dilute Magnetic Alloys. *Prog. Theor. Phys.* **32**, 37–49 (1964).
- [4] Wilson, K. G. The renormalization group: Critical phenomena and the Kondo problem. *Rev. Mod. Phys.* **47**, 773–840 (1975).
- [5] Si, Q. & Steglich, F. Heavy fermions and quantum phase transitions. *Science*. **329**, 1161–1166 (2010).
- [6] Anderson, P. W. Breaking the log-jam in many-body physics: Fermi surfaces without Fermi liquids. *Phys. Scr.* **T42**, 11–16 (1992).
- [7] Moore, J. E. The birth of topological insulators. *Nature* **464**, 194–8 (2010).
- [8] Phillips, P. *Advanced Solid State Physics* (Cambridge University Press, Cambridge, UK, 2012), 2 edn.
- [9] Landau, L. D. The Theory of a Fermi Liquid. *Sov. Phys. JETP* **3**, 920 (1957).
- [10] *Wikimedia Commons*. Band Gap Comparison (2015).

BIBLIOGRAPHY

- [11] Tan, B. S. *et al.* Unconventional Fermi surface in an insulating state. *Science*. **349**, 287–290 (2015).
- [12] Hartstein, M. *et al.* Fermi surface in the absence of a Fermi liquid in the Kondo insulator SmB₆. *Nat. Phys.* **14**, 166 (2018).
- [13] Shoenberg, D. *Magnetic Oscillations in Metals* (Cambridge University Press, Cambridge, UK, 1984).
- [14] Nickerson, J. C. *et al.* Physical properties of SmB₆. *Phys. Rev. B* **3**, 2030–2042 (1971).
- [15] Iga, F., Kasaya, M. & Kasuya, T. Specific Heat Measurements of YbB₁₂ and Yb_xLu_{1-x}B₁₂. *J. Magn. Magn. Mater.* **76&77**, 156–158 (1988).
- [16] Petrovic, C. *et al.* Kondo insulator description of spin state transition in FeSb₂. *Phys. Rev. B* **72**, 045103 (2005).
- [17] Perucchi, A., Degiorgi, L., Hu, R., Petrovic, C. & Mitrovic, V. F. Optical investigation of the metal-insulator transition in FeSb₂. *Eur. Phys. J. B* **54**, 175–183 (2006).
- [18] Dzero, M., Xia, J., Galitski, V. & Coleman, P. Topological Kondo Insulators. *Annu. Rev. Condens. Matter Phys.* **7**, 249–280 (2016).
- [19] Xu, K. J. *et al.* Metallic surface states in a correlated *d*-electron topological Kondo insulator candidate FeSb₂. *Proc. Natl. Acad. Sci. U. S. A.* **117**, 15409 (2020).
- [20] Keimer, B., Kivelson, S. A., Norman, M. R., Uchida, S. & Zaanen, J. From quantum matter to high-temperature superconductivity in copper oxides. *Nature* **518**, 179–186 (2015).
- [21] Coleman, P. *Introduction to Many-Body Physics* (Cambridge University Press, Cambridge, UK, 2015).
- [22] Stormer, H. L., Tsui, D. C. & Gossard, A. C. Fractional quantum hall effect. *Rev. Mod. Phys.* **71**, S298–S305 (1999).

- [23] Simon, S. H. *The Oxford Solid State Basics* (Oxford University Press, Oxford, UK, 2013), 1 edn.
- [24] Anderson, P. W. Localized Magnetic States in Metals. *Phys. Rev.* **124**, 41–53 (1961).
- [25] Anderson, P. W. Local moments and localized states. *Rev. Mod. Phys.* **50**, 191–201 (1978).
- [26] Abrikosov, A. A. Electron Scattering on Magnetic Impurities in Metals and Anomalous Resistivity Effects. *Phys. Phys. Fiz.* **2**, 5–20 (1965).
- [27] Suhl, H. Dispersion Theory of the Kondo Effect. *Phys. Rev.* **138**, A515–A523 (1965).
- [28] Ruderman, M. A. & Kittel, C. Indirect exchange coupling of nuclear magnetic moments by conduction electrons. *Phys. Rev.* **96**, 99–102 (1954).
- [29] Mott, N. F. Rare-earth compounds with mixed valencies. *Philos. Magazine* **30**, 403–416 (1974).
- [30] Doniach, S. The Kondo Lattice and Weak Antiferromagnetism. *Physica* **91B**, 231–234 (1977).
- [31] de Haas, W. J. & van Alphen, P. M. The dependence of the susceptibility of diamagnetic metals upon the field. *Proc. Acad. Sci. Amsterdam* **33**, 1106 (1930).
- [32] Taillefer, L. & Lonzarich, G. G. Heavy-fermion quasiparticles in UPt₃. *Phys. Rev. Lett.* **60**, 1570–1573 (1988).
- [33] Sebastian, S. E., Harrison, N. & Lonzarich, G. G. Quantum oscillations in the high-T_c cuprates. *Philos. Trans. A. Math. Phys. Eng. Sci.* **369**, 1687–1711 (2011).
- [34] Griffiths, D. J. *Introduction to Electrodynamics* (Pearson, London, 2013).
- [35] Onsager, L. Interpretation of the de Haas-van Alphen effect. *London, Edinburgh, Dublin Philos. Mag. J. Sci.* **43**, 1006–1008 (1952).
- [36] Griffiths, D. J. *Introduction to Quantum Mechanics* (Pearson, London, 2005).

BIBLIOGRAPHY

- [37] Snoke, D. W. *Solid State Physics* (Cambridge University Press, Cambridge, UK, 2020), 2 edn.
- [38] Dresselhaus, M., Dresselhaus, G., Cronin, S. B. & Gomes Souza Filho, A. *Solid State Properties* (Springer-Verlag GmbH, 2018), berlin edn.
- [39] Blundell, S. J. & Blundell, K. M. *Concepts in Thermal Physics* (Oxford University Press, Oxford, UK, 2010).
- [40] de Haas, W. J. & van Alphen, P. M. The dependence of the susceptibility of diamagnetic metals upon the field. *Comm. Phys. Lab. Leiden* **208d**, **212a** (1930).
- [41] Schubnikow, L. & de Haas, W. J. New phenomena in the change in resistance of bismuth crystals in a magnetic field at the temperature of liquid hydrogen. *Comm. Phys. Lab. Leiden* **207a**, **207d** (1930).
- [42] Pippard, A. B. *The Dynamics of Conduction Electrons* (Gordon and Breach, London, 1965).
- [43] Lifshitz, I. M. & Kosevich, A. M. Theory of Magnetic Susceptibility in Metals at Low Temperatures. *Sov. Phys. JETP* **2**, 636–645 (1956).
- [44] Carrington, A. Quantum oscillation studies of the Fermi surface of iron-pnictide superconductors. *Reports Prog. Phys.* **74**, 124507 (2011).
- [45] Kasaya, M., Iga, F., Negishi, K., Nakai, S. & Kasuya, T. A new and typical valence fluctuating system, YbB₁₂. *J. Magn. Magn. Mater.* **31-34**, 437–438 (1983).
- [46] Werheit, H. *et al.* Raman scattering and isotopic phonon effects in dodecaborides. *J. Phys. Condens. Matter* **23**, 065403 (2011).
- [47] Kasaya, M., Iga, F., Takigawa, M. & Kasuya, T. Mixed valence properties of YbB₁₂. *J. Magn. Magn. Mater.* **47-48**, 429–435 (1985).

- [48] Schlesinger, M. E. The Lesser-Known B-Ln (Boron-Lanthanide) Systems: B-Dy (Boron-Dysprosium), B-Ho (Boron-Holmium), B-Lu (Boron-Lutetium), B-Pr (Boron-Praseodymium), B-Tm (Boron-Thulium), and B-Yb (Boron-Ytterbium). *J. Phase Equilibria* **19**, 49–55 (1998).
- [49] Iga, F., Shimizu, N. & Takabatake, T. Single crystal growth and physical properties of Kondo insulator YbB₁₂. *J. Magn. Magn. Mater.* **177-181**, 337–338 (1998).
- [50] Sun, P., Oeschler, N., Johnsen, S., Iversen, B. B. & Steglich, F. Huge thermoelectric power factor: FeSb₂ versus FeAs₂ and RuSb₂. *Appl. Phys. Express* **2**, 091102 (2009).
- [51] Holseth, H. & Kjekshus, A. Compounds with the marcasite type crystal structure III. On the magnetic properties of the binary pnictides. *J. Less-Common Met.* **16**, 472–474 (1968).
- [52] Yang, G. *et al.* Electropolishing of surfaces: theory and applications. *Surf. Eng.* **33**, 149–166 (2017).
- [53] Morillo, J. & de Novion, C.-H. Destruction of the gap in the intermediate valence compound SmB₆ by neutron irradiation. *Solid State Commun.* **48**, 315–319 (1983).
- [54] Pristas, G., Gabani, S., Flachbart, K., Filipov, V. & Shitsevalova, N. Investigation of the Energy Gap in Sm_{1-x}B₆ and Sm_{1-x}La_xB₆ Kondo Insulators. *Proc. Int. Conf. Strongly Correl. Electron Syst.* **3**, 012021 (2014).
- [55] Yntema, G. B. Superconducting Winding for Electromagnet. *Phys. Rev.* **98**, 1197 (1955).
- [56] Herlach, F. & Miura, N. *High magnetic fields: science and technology* (World Scientific Publishing Co. Inc., London, 2006).
- [57] Coyne, K. New world-record magnet fulfills superconducting promise (2017).
- [58] Coyne, K. MagLab reclaims record for strongest resistive magnet (2017).

BIBLIOGRAPHY

- [59] Hahn, S. *et al.* 45.5-Tesla Direct-Current Magnetic Field Generated With a High-Temperature Superconducting Magnet. *Nature* **570**, 496–499 (2019).
- [60] Schneider-Muntau, H. J., Toth, J. & Weijers, H. W. Generation of the highest continuous magnetic fields. *IEEE Trans. Appl. Supercond.* **14**, 1245–1252 (2004).
- [61] 45 Tesla, 32 mm Bore Hybrid Magnet (Cell 15) (2018).
- [62] Meet the 100 Tesla Pulsed Magnet (2015).
- [63] Swenson, C. A. *et al.* Pulse magnet development program at NHMFL. *IEEE Trans. Appl. Supercond.* **14**, 1233–1236 (2004).
- [64] Zherlitsyn, S., Wustmann, B., Herrmannsdorfer, T. & Wosnitza, J. Status of the Pulsed-Magnet-Development Program at the Dresden High Magnetic Field Laboratory. *IEEE Trans. Appl. Supercond.* **22**, 4300603 (2012).
- [65] Nakamura, D., Ikeda, A., Sawabe, H., Matsuda, Y. H. & Takeyama, S. Record indoor magnetic field of 1200~T generated by electromagnetic flux-compression. *Rev. Sci. Instrum.* **89**, 095106 (2018).
- [66] Griessen, R. A capacitance torquemeter for de Haas-van Alphen measurements. *Cryogenics.* **13**, 375–377 (1973).
- [67] Willemin, M. *et al.* Piezoresistive cantilever designed for torque magnetometry. *J. Appl. Phys.* **83**, 1163–1170 (1998).
- [68] Schnack, H. G., Griessen, R., Noordeloos, P. & Heeck, K. Continuously rotatable high field capacitance torque magnetometer. *Physica C Supercond. its Appl.* **266**, 285–295 (1996).
- [69] Iga, F. *et al.* Anisotropic magnetoresistance and collapse of the energy gap in $\text{Yb}_{1-x}\text{Lu}_x\text{B}_{12}$. *J. Phys. Conf. Ser.* **200**, 012064 (2010).
- [70] Smits, F. M. Measurement of Sheet Resistivities with the Four-Point Probe. *Bell Syst. Tech. J.* **37**, 711 (1958).

- [71] Hodgson, R. T., Baglin, J. E., Pal, R., Neri, J. M. & Hammer, D. A. Ion beam annealing of semiconductors. *Appl. Phys. Lett.* **37**, 187–189 (1980).
- [72] Ellguth, M., Tusche, C., Iga, F. & Suga, S. Momentum microscopy of single crystals with detailed surface characterisation. *Philos. Mag.* **96**, 3284–3306 (2016).
- [73] Monch, W. *Electronic Properties of Semiconductor Interfaces* (Springer-Verlag Berlin Heidelberg, Berlin, 2004).
- [74] Altarawneh, M. M., Mielke, C. H. & Brooks, J. S. Proximity detector circuits: An alternative to tunnel diode oscillators for contactless measurements in pulsed magnetic field environments. *Rev. Sci. Instrum.* **80**, 066104 (2009).
- [75] Clover, R. B. & Wolf, W. P. Magnetic susceptibility measurements with a tunnel diode oscillator. *Rev. Sci. Instrum.* **41**, 617–621 (1970).
- [76] Van Degriift, C. T. Tunnel diode oscillator for 0.001~ppm measurements at low temperatures. *Rev. Sci. Instrum.* **46**, 599–607 (1975).
- [77] Van Degriift, C. T. & Love, D. P. Modeling of tunnel diode oscillators. *Rev. Sci. Instrum.* **52**, 712–723 (1981).
- [78] Coffey, T. *et al.* Measuring radio frequency properties of materials in pulsed magnetic fields with a tunnel diode oscillator. *Rev. Sci. Instrum.* **71**, 4600–4606 (2000).
- [79] Caulfield, J. *et al.* The effects of open sections of the Fermi surface on the physical properties of 2D organic molecular metals. *Synth. Met.* **61**, 63–67 (1993).
- [80] Gvozdikov, V. M., Pershin, Y. V., Steep, E., Jansen, A. G. & Wyder, P. De Haas-van Alphen oscillations in the quasi-two-dimensional organic conductor κ -(ET)₂Cu(NCS)₂: The magnetic breakdown approach. *Phys. Rev. B* **65**, 165102 (2002).
- [81] Sebastian, S. E. *et al.* A multi-component Fermi surface in the vortex state of an underdoped high- T_c superconductor. *Nature* **454**, 200–203 (2008).

BIBLIOGRAPHY

- [82] Cleveland, W. S. Robust Locally Weighted Regression and Smoothing Scatterplots. *J. Am. Stat. Assoc.* **74**, 829–836 (1979).
- [83] Kennedy, J. & Eberhart, R. Particle Swarm Optimization. In *Proc. ICNN'95 - Int. Conf. Neural Networks*, 1942–1948 (1995).
- [84] Shi, Y. & Eberhart, R. A modified particle swarm optimizer. In *1998 IEEE Int. Conf. Evol. Comput. Proceedings. IEEE World Congr. Comput. Intell.*, 69–73 (1998).
- [85] Sebastian, S. E. *et al.* Normal-state nodal electronic structure in underdoped high- T_c copper oxides. *Nature* **511**, 61–64 (2014).
- [86] Ekino, T. *et al.* Tunneling spectroscopy of the Kondo-semiconducting gap in YbB_{12} . *Physica B* **259-261**, 315–316 (1999).
- [87] Okamura, H. *et al.* Indirect and Direct Energy Gaps in Kondo Semiconductor YbB_{12} . *J. Phys. Soc. Japan* **74**, 1954–1957 (2005).
- [88] Xiang, Z. *et al.* Quantum oscillations of electrical resistivity in an insulator. *Science*. **362**, 65–69 (2018).
- [89] Hagiwara, K. *et al.* Surface Kondo effect and non-trivial metallic state of the Kondo insulator YbB_{12} . *Nat. Commun.* **7**, 12690 (2016).
- [90] Kim, D. J., Xia, J. & Fisk, Z. Topological surface state in the Kondo insulator samarium hexaboride. *Nat. Mater.* **13**, 466–470 (2014).
- [91] Kim, D. J. *et al.* Surface Hall Effect and Nonlocal Transport in SmB_6 : Evidence for Surface Conduction. *Sci. Rep.* **3**, 3150 (2013).
- [92] Nefeodova, E. *et al.* Inelastic neutron scattering study of the Kondo semiconductor YbB_{12} . *Phys. Rev. B* **60**, 13507 (1999).
- [93] Nemkovski, K. S. *et al.* Polarized-neutron study of spin dynamics in the kondo insulator YbB_{12} . *Phys. Rev. Lett.* **99**, 137204 (2007).

- [94] Iga, F. *et al.* Magnetic excitations in a single crystal of the Kondo semiconductor YbB₁₂. *J. Phys. Chem. Solids* **60**, 1193–1196 (1999).
- [95] Mignot, J. M. *et al.* Evidence for short-range antiferromagnetic fluctuations in kondo-insulating YbB₁₂. *Phys. Rev. Lett.* **94**, 247204 (2005).
- [96] Sato, Y. *et al.* Unconventional thermal metallic state of charge-neutral fermions in an insulator. *Nat. Phys.* **15**, 954–959 (2019).
- [97] Terashima, T. T. *et al.* Magnetic-Field-Induced Kondo Metal Realized in YbB₁₂. *Phys. Rev. Lett.* **120**, 257206 (2018).
- [98] Bat'ková, M., Bat'ko, I., Konovalova, E., Shitsevalova, N. & Paderno, Y. Gap properties of SmB₆ and YbB₁₂: Electrical resistivity and tunnelling spectroscopy studies. *Physica B Condens. Matter* **378-380**, 618–619 (2006).
- [99] Terashima, T. T. *et al.* Magnetization process of the Kondo insulator YbB₁₂ in ultra-high magnetic fields. *J. Phys. Soc. Japan* **86**, 054710 (2017).
- [100] Sugiyama, K., Iga, F., Kasaya, M., Kasuya, T. & Date, M. Field-Induced Metallic State in YbB₁₂ under High Magnetic Field. *J. Phys. Soc. Japan* **57**, 3946–3953 (1988).
- [101] Matsuda, Y. H., Kakita, Y. & Iga, F. The temperature dependence of the magnetization process of the kondo insulator YbB₁₂. *Crystals* **10**, 26 (2020).
- [102] Gabáni, S. *et al.* Properties of the in-gap states in SmB₆. *Solid State Commun.* **117**, 641–644 (2001).
- [103] Liu, H. *et al.* Fermi surfaces in Kondo insulators. *J. Phys. Condens. Matter* **30**, 16LT01 (2018).
- [104] Li, G. *et al.* Two-dimensional Fermi surfaces in Kondo Insulator SmB₆. *Science*. **346**, 1208 – 1212 (2014).

BIBLIOGRAPHY

- [105] Hartstein, M. *Fermi Surfaces and Where to Find Them: Quantum Oscillations in Kondo Insulators and High-Temperature Superconductors*. Phd thesis, University of Cambridge (2021).
- [106] Bulaevskii, L. N., Batista, C. D., Mostovoy, M. V. & Khomskii, D. I. Electronic orbital currents and polarization in Mott insulators. *Phys. Rev. B* **78**, 024402 (2008).
- [107] Motrunich, O. I. Orbital magnetic field effects in spin liquid with spinon Fermi sea: Possible application to κ -(ET)₂Cu₂(CN)₃. *Phys. Rev. B* **73**, 155115 (2006).
- [108] Baskaran, G. Majorana Fermi Sea in Insulating SmB₆: A proposal and a Theory of Quantum Oscillations in Kondo Insulators. *arXiv* 1507.03477 (2015).
- [109] Erten, O., Chang, P. Y., Coleman, P. & Tsvetlik, A. M. Skyrme Insulators: Insulators at the Brink of Superconductivity. *Phys. Rev. Lett.* **119**, 057603 (2017).
- [110] Varma, C. M. Majoranas in mixed-valence insulators. *Phys. Rev. B* **102**, 155145 (2020).
- [111] Chowdhury, D., Sodemann, I. & Senthil, T. Mixed-valence insulators with neutral Fermi surfaces. *Nat. Commun.* **9**, 1766 (2018).
- [112] Miyake, K. de Haas-van Alphen oscillations in superconducting states as a probe of gap anisotropy. *Physica B Condens. Matter* **186-188**, 115–117 (1993).
- [113] Knolle, J. & Cooper, N. R. Quantum Oscillations without a Fermi Surface and the Anomalous de Haas-van Alphen Effect. *Phys. Rev. Lett.* **115**, 146401 (2015).
- [114] Riseborough, P. S. & Fisk, Z. Critical examination of quantum oscillations in SmB₆. *Phys. Rev. B* **96**, 195122 (2017).
- [115] Peters, R., Yoshida, T. & Kawakami, N. Quantum oscillations in strongly correlated topological Kondo insulators. *Phys. Rev. B* **100**, 085124 (2019).
- [116] Zhang, L., Song, X. Y. & Wang, F. Quantum Oscillation in Narrow-Gap Topological Insulators. *Phys. Rev. Lett.* **116**, 046404 (2016).

- [117] Lee, P. A. Quantum oscillations in the activated conductivity in excitonic insulators: Possible application to monolayer WTe₂. *Phys. Rev. B* **103**, L041101 (2021).
- [118] Settai, R. *et al.* Quasi-two-dimensional Fermi surfaces and the de Haas-van Alphen oscillation in both the normal and superconducting mixed states of CeCoIn₅. *J. Phys. Condens. Matter* **13**, L627–L634 (2001).
- [119] Hedo, M. *et al.* Magnetoresistance and de Haas-van Alphen oscillation in normal and superconducting CeRu₂. *Philos. Mag. B* **77**, 975–1000 (1998).
- [120] Inada, Y. *et al.* Fermi Surface and de Haas-van Alphen Oscillation in both the Normal and Superconducting Mixed States of UPd₂Al₃. *J. Phys. Soc. Japan* **68**, 3643–3654 (1999).
- [121] Ohkuni, H. *et al.* Fermi surface properties and de Haas-van Alphen oscillation in both the normal and superconducting mixed states of URu₂Si₂. *Philos. Mag. B* **79**, 1045–1077 (1999).
- [122] Hartstein, M. *et al.* Intrinsic Bulk Quantum Oscillations in a Bulk Unconventional Insulator SmB₆. *iScience* **23**, 101632 (2020).
- [123] Ishizawa, Y., Tanaka, T., Bannai, E. & Kawai, S. de Haas-van Alphen Effect and Fermi Surface of LaB₆. *J. Phys. Soc. Japan* **42**, 112–118 (1977).
- [124] Onuki, Y., Komatsubara, T., Reinders, P. H. P. & Springford, M. Fermi Surface and Cyclotron Mass of CeB₆. *J. Phys. Soc. Japan* **58**, 3698–3704 (1989).
- [125] Heinecke, M. *et al.* Quantum oscillations and the Fermi surface of LuB₁₂. *Zeitschrift für Phys. B Condens. Matter* **98**, 231–237 (1995).
- [126] Okuda, N. *et al.* Elastic quantum oscillation of LuB₁₂. *Physica B Condens. Matter* **281-282**, 756–757 (2000).
- [127] Harima, H., Yanase, A. & Kasuya, T. Energy bandstructure of YB₁₂ and LuB₁₂. *J. Magn. Magn. Mater.* **47-48**, 567–569 (1985).

BIBLIOGRAPHY

- [128] Tran, F. & Blaha, P. Accurate band gaps of semiconductors and insulators with a semilocal exchange-correlation potential. *Phys. Rev. Lett.* **102**, 226401 (2009).
- [129] Xiang, Z. *et al.* Unusual high-field metal in a Kondo insulator. *Nat. Phys.* **17**, 788 (2021).
- [130] Hulliger, F. Über den Zusammenhang zwischen Magnetismus und elektrischer Leitfähigkeit von Verbindungen mit Übergangselementen. *Helv. Phys. Acta* **32**, 615 (1959).
- [131] Tomczak, J. M. Thermoelectricity in correlated narrow-gap semiconductors. *J. Phys. Condens. Matter* **30**, 183001 (2018).
- [132] Takahashi, H., Okazaki, R., Terasaki, I. & Yasui, Y. Origin of the energy gap in the narrow-gap semiconductor FeSb₂ revealed by high-pressure magnetotransport measurements. *Phys. Rev. B* **88**, 165205 (2013).
- [133] Sun, P. *et al.* Highly dispersive electron relaxation and colossal thermoelectricity in the correlated semiconductor FeSb₂. *Phys. Rev. B* **88**, 245203 (2013).
- [134] Herzog, A. *et al.* Strong electron correlations in FeSb₂: An optical investigation and comparison with RuSb₂. *Phys. Rev. B* **82**, 245205 (2010).
- [135] Homes, C. C. *et al.* Unusual electronic and vibrational properties in the colossal thermopower material FeSb₂. *Sci. Rep.* **8**, 11692 (2018).
- [136] Petrovic, C. *et al.* Anisotropy and large magnetoresistance in the narrow-gap semiconductor FeSb₂. *Phys. Rev. B* **67**, 155205 (2003).
- [137] Hu, R., Mitrović, V. F. & Petrovic, C. Anisotropy in the magnetic and transport properties of Fe_{1-x}Co_xSb₂. *Phys. Rev. B* **74**, 195130 (2006).
- [138] Takahashi, H., Yasui, Y., Terasaki, I. & Sato, M. Effects of ppm-level imperfection on the transport properties of FeSb₂ single crystals. *J. Phys. Soc. Japan* **80**, 054708 (2011).

- [139] Jie, Q. *et al.* Electronic thermoelectric power factor and metal-insulator transition in FeSb₂. *Phys. Rev. B* **86**, 115121 (2012).
- [140] Bentien, A., Johnsen, S., Madsen, G. K., Iversen, B. B. & Steglich, F. Colossal Seebeck coefficient in strongly correlated semiconductor FeSb₂. *EPL* **80**, 17008 (2007).
- [141] Steger, J. & Kostiner, E. Mössbauer effect study of FeSb₂. *J. Solid State Chem.* **5**, 131–135 (1972).
- [142] Zaliznyak, I. A., Savici, A. T., Garlea, V. O., Hu, R. & Petrovic, C. Absence of localized-spin magnetism in the narrow-gap semiconductor FeSb₂. *Phys. Rev. B* **83**, 184414 (2011).
- [143] Koyama, T., Nakamura, H., Kohara, T. & Takahashi, Y. Magnetization process of narrow-gap semiconductor FeSb₂. *J. Phys. Soc. Japan* **79**, 093704 (2010).
- [144] Diakhate, M. S. *et al.* Thermodynamic, thermoelectric, and magnetic properties of FeSb₂: A combined first-principles and experimental study. *Phys. Rev. B* **84**, 125210 (2011).
- [145] Sun, P., Oeschler, N., Johnsen, S., Iversen, B. B. & Steglich, F. FeSb₂: Prototype of huge electron-diffusion thermoelectricity. *Phys. Rev. B* **79**, 153308 (2009).
- [146] Sun, P., Oeschler, N., Johnsen, S., Iversen, B. B. & Steglich, F. Narrow band gap and enhanced thermoelectricity in FeSb₂. *Dalt. Trans.* **39**, 1012–1019 (2010).
- [147] Takahashi, H. *et al.* Colossal Seebeck effect enhanced by quasi-ballistic phonons dragging massive electrons in FeSb₂. *Nat. Commun.* **7**, 12732 (2016).
- [148] Dzero, M., Xia, J., Galitski, V. & Coleman, P. Topological Kondo Insulators. *Phys. Rev. Lett.* **104**, 106408 (2010).
- [149] Amon, A. *et al.* Tracking aluminium impurities in single crystals of the heavy-fermion superconductor UBe₁₃. *Sci. Rep.* **8**, 10654 (2018).

BIBLIOGRAPHY

- [150] Terashima, T. *et al.* Ferromagnetism vs paramagnetism and false quantum oscillations in lanthanum-doped CaB_6 . *J. Phys. Soc. Japan* **69**, 2423–2426 (2000).
- [151] Rudolph, P. *Handbook of Crystal Growth: Bulk Crystal Growth* (Elsevier, Amsterdam, 2015), ii edn.
- [152] Liu, H. *et al.* Quantum oscillations coupled to metamagnetism in the correlated insulator FeSb_2 . *Unpublished* .
- [153] Becquerel, J. *Le Magnetisme* (Institut International de Cooperation Intellectuelle, CNRS, Paris, 1940).
- [154] Jacobs, I. S. & Lawrence, P. E. Metamagnetic Phase Transitions and Hysteresis in FeCl_2 . *Phys. Rev.* **164**, 866–878 (1976).
- [155] Stryjewski, E. & Giordano, N. Metamagnetism. *Adv. Phys.* **26**, 487–650 (1977).
- [156] Gonçalves da Silva, C. E. T. Magnetic Susceptibility of FeSb_2 : A Quasi-Magnetic Semiconductor. *Solid State Commun.* **33**, 63–68 (1980).
- [157] Lukoyanov, A. V., Mazurenko, V. V., Anisimov, V. I., Sigrist, M. & Rice, T. M. The semiconductor-to-ferromagnetic-metal transition in FeSb_2 . *Eur. Phys. J. B* **53**, 205–207 (2006).
- [158] Fuhrman, W. T. *et al.* Screened moments and extrinsic in-gap states in samarium hexaboride. *Nat. Commun.* **9**, 1539 (2018).
- [159] Fuhrman, W. T. & Nikolić, P. Magnetic impurities in Kondo insulators: An application to samarium hexaboride. *Phys. Rev. B* **101**, 245118 (2020).
- [160] Thomas, S. M. *et al.* Quantum Oscillations in Flux-Grown SmB_6 with Embedded Aluminum. *Phys. Rev. Lett.* **122**, 166401 (2019).
- [161] Shen, H. & Fu, L. Quantum Oscillation from In-Gap States and a Non-Hermitian Landau Level Problem. *Phys. Rev. Lett.* **121**, 026403 (2018).

- [162] Erten, O., Ghaemi, P. & Coleman, P. Kondo Breakdown and Quantum Oscillations in SmB_6 . *Phys. Rev. Lett.* **116**, 046403 (2016).
- [163] Pal, H. K. Quantum oscillations from inside the Fermi sea. *Phys. Rev. B* **95**, 085111 (2017).
- [164] Grover, T., Trivedi, N., Senthil, T. & Lee, P. A. Weak Mott insulators on the triangular lattice: Possibility of a gapless nematic quantum spin liquid. *Phys. Rev. B* **81**, 245121 (2010).
- [165] Katsura, H., Nagaosa, N. & Lee, P. A. Theory of the Thermal Hall Effect in Quantum Magnets. *Phys. Rev. Lett.* **104**, 066403 (2010).
- [166] Sodemann, I., Chowdhury, D. & Senthil, T. Quantum oscillations in insulators with neutral Fermi surfaces. *Phys. Rev. B* **97**, 045152 (2018).
- [167] Capponi, S. & Assaad, F. F. Spin and charge dynamics of the ferromagnetic and antiferromagnetic two-dimensional half-filled Kondo lattice model. *Phys. Rev. B* **63**, 155114 (2001).
- [168] Czajka, P. *et al.* Oscillations of the thermal conductivity in the spin-liquid state of $\alpha\text{-RuCl}_3$. *Nat. Phys.* **17**, 915–919 (2021).
- [169] Smeibidl, P. *et al.* First Hybrid Magnet for Neutron Scattering at Helmholtz-Zentrum Berlin. *IEEE Trans. Appl. Supercond.* **26**, 4301606 (2016).
- [170] Chang, T. R. *et al.* Two distinct topological phases in the mixed-valence compound YbB_6 and its differences from SmB_6 . *Phys. Rev. B* **91**, 155151 (2015).
- [171] Liu, H. *et al.* *f*-electron hybridised metallic Fermi surface in magnetic field-induced metallic YbB_{12} . *arXiv* 2102.09545 (2021).
- [172] Chikina, A. *et al.* Correlated electronic structure of colossal thermopower FeSb_2 : An ARPES and *ab initio* study. *Phys. Rev. Res.* **2**, 023190 (2020).

BIBLIOGRAPHY

- [173] Wolgast, S. *et al.* Reduction of the low-temperature bulk gap in samarium hexaboride under high magnetic fields. *Phys. Rev. B* **95**, 245112 (2017).
- [174] Derr, J., Knebel, G., Braithwaite, D., Salce, B. & Flouquet, J. From unconventional insulating behavior towards conventional magnetism in the intermediate-valence compound SmB_6 . *Phys. Rev. B* **77**, 193107 (2008).
- [175] Mani, A., Janaki, J., Satya, A. T., Geetha Kumary, T. & Bharathi, A. The pressure induced insulator to metal transition in FeSb_2 . *J. Phys. Condens. Matter* **24**, 075601 (2012).
- [176] Kayama, S. *et al.* Pressure induced insulator-to-metal transition at 170~GPa of Kondo semiconductor YbB_{12} . *Proc. Int. Conf. Strongly Correl. Electron Syst.* **3**, 012024 (2014).
- [177] Cooley, J. C. *et al.* High magnetic fields and the correlation gap in SmB_6 . *Phys. Rev. B* **52**, 7322–7327 (1995).
- [178] Figueira, M. S., Silva-Valencia, J. & Franco, R. Thermoelectric properties of the Kondo insulator FeSb_2 . *Eur. Phys. J. B* **85**, 203 (2012).
- [179] Wang, P. *et al.* Landau quantization and highly mobile fermions in an insulator. *Nature* **589**, 225 (2021).
- [180] Eo, Y. S. *et al.* Transport gap in SmB_6 protected against disorder. *Proc. Natl. Acad. Sci. U. S. A.* **116**, 12638–12641 (2019).